Jordan Journal of
PHYSICS
An International Peer-Reviewed Research Journal

Volume 7, No. 1, 2014, 1435 H

Jordan Journal of Physics (*JJP*): An International Peer-Reviewed Research Journal issued by the support of the Scientific Research Support Fund, Ministry of Higher Education & Scientific Research, Jordan, and published quarterly by the Deanship of Research & Graduate Studies, Yarmouk University, Irbid, Jordan.

Manuscripts should be submitted to:

Prof. Nihad A. Yusuf
Editor-in-Chief, Jordan Journal of Physics
Deanship of Research and Graduate Studies
Yarmouk University-Irbid-Jordan
Tel. 00 962 2 7211111 Ext. 2075
E-mail: *jjp@yu.edu.jo*
Website: *http://Journals.yu.edu.jo/jjp*

Jordan Journal of

PHYSICS

An International Peer-Reviewed Research Journal

Volume 7, No. 1, 2014, 1435 H

INTERNATIONAL ADVISORY BOARD

Prof. Dr. Ahmad Saleh
Department of Physics, Yarmouk University, Irbid, Jordan.
salema@yu.edu.jo

Prof. Dr. Aurore Savoy-Navarro
LPNHE Universite de Paris 6/IN2P3-CNRS, Tour 33, RdC 4, Place Jussieu, F 75252, Paris Cedex 05, France.
auore@lpnhep.in2p3.fr

Prof. Dr. Bernard Barbara
Laboratoire Louis Neel, Salle/Room: D 108, 25, Avenue des Martyrs BP 166, 38042-Grenoble Cedex 9, France.
Barbara@grenoble.cnrs.fr

Prof. Dr. Bruno Guiderdoni
Observatoire Astronomique de Lyon, g, avenue Ch. Antre-F-69561, Saint Genis Laval Cedex, France.
Bruno.guiderdoni@olos.univ-lyon1.fr

Prof. Dr. Buford Price
Physics Department, University of California, Berkeley, CA 94720, U. S. A.
bprice@berkeley.edu

Prof. Dr. Colin Cough
School of Physics and Astronomy, University of Birmingham, B15 2TT, U. K.
c.gough@bham.ac.uk

Prof. Dr. Desmond Cook
Department of Physics, Condensed Matter and Materials Physics Research Group, Old Dominion University, Norfolk, Virginia 23529, U. S. A.
Dcook@physics.odu.edu

Prof. Dr. Evgeny Sheshin
MIPT, Institutskij per. 9, Dogoprudnyi 141700, Russia.
sheshin@lafeet.mipt.ru

Prof. Dr. Hans Ott
Laboratorium Fuer Festkorperphysik, ETH Honggerberg, CH-8093 Zurich, Switzerland.
ott@solid.phys.ethz.ch

Prof. Dr. Herwig Schopper
President SESAME Council, Chairman Scientific Board UNESCO IBSP Programme, CERN, 1211 Geneva, Switzerland.
Herwig.Schopper@cern.ch

Prof. Dr. Humam Ghassib
Department of Physics, Jordan University, Amman, Jordan.
humam@atf.org.jo

Prof. Dr. Ingo Hofmann
GSI Darmstadt, Planckstr. 1, 64291, Darmstadt, Germany.
i.hofmann@gsi.de

Prof. Dr. Jozef Lipka
Department of Nuclear Physics and Technology, Slovak University of Technology, Bratislava, Ilkovicova 3, 812 19 Bratislava, Slovakia.
Lipka@elf.stuba.sk

Prof. Dr. Khalid Touqan
Chairman of Jordan Atomic Energy Commission, Amman, Jordan.

Prof. Dr. Mark J. Hagmann
Desert Electronics Research Corporation, 762 Lacey Way, North Salt Lake 84064, Utah, U. S. A.
MHagmann@NewPathResearch.Com.

Prof. Dr. Nasr Zubeidey
President*: Al-Zaytoonah University of Jordan, Amman, Jordan.*
President@alzaytoonah.edu.jo

Prof. Dr. Patrick Roudeau
Laboratoire de I'Accelerateur, Lineaire (LAL), Universite Paris-Sud 11, Batiment 200, 91898 Orsay Cedex, France.
roudeau@mail.cern.ch

Prof. Dr. Paul Chu
Department of Physics, University of Houston, Houston, Texas 77204-5005, U. S. A.
Ching-Wu.Chu@mail.uh.edu

Prof. Dr. Peter Dowben
Nebraska Center for Materials and Nanoscience, Department of Physics and Astronomy, 255 Behlen Laboratory (10th and R Streets), 116 Brace Lab., P. O. Box 880111, Lincoln, NE 68588-0111, U. S. A.
pdowben@unl.edu

Prof. Dr. Peter Mulser
Instiute fuer Physik, T.U. Darmstadt, Hochschulstr. 4a, 64289 Darmstadt, Germany.
Peter.mulser@physik.tu-darmstadt.de

Prof. Dr. Rasheed Azzam
Department of Electrical Engineering, University of New Orleans New Orleans, Louisiana 70148, U. S. A.
razzam@uno.edu

Dr. Richard G. Forbes
University of Surrey, FEPS (X1), Guildford, Surrey GU2 7XH, U. K.
R.Forbes@surrey.ac.uk

Prof. Dr. Roy Chantrell
Physics Department, York University, York, YO10 5DD, U. K.
Rc502@york.ac.uk

Prof. Dr. Shawqi Al-Dallal
Department of Physics, Faculty of Science, University of Bahrain, Manamah, Kingdom of Bahrain.

Prof. Dr. Susamu Taketomi
Matsumoto Yushi-Seiyaku Co. Ltd., Shibukawa-Cho, Yao City, Osaka 581-0075, Japan.
staketomi@hotmail.com

Prof. Dr. Wolfgang Nolting
Institute of Physics / Chair: Solid State Theory, Humboldt-University at Berlin, Newtonstr. 15 D-12489 Berlin, Germany
Wolfgang.nolting@physik.hu-berlin.de

The Hashemite Kingdom of Jordan

Yarmouk University

Jordan Journal of
PHYSICS

An International Peer-Reviewed Research Journal issued by the Support of the Scientific Research Support Fund

Volume 7, No. 1, 2014, 1435 H

Instructions to Authors

Instructions to authors concerning manuscript organization and format apply to hardcopy submission by mail, and also to electronic online submission via the Journal homepage website (http://jjp.yu.edu.jo).

Manuscript Submission

1- **Hardcopy**: The original and three copies of the manuscript, together with a covering letter from the corresponding author, should be submitted to the Editor-in-Chief:

Professor Nihad A. Yusuf
Editor-in-Chief, Jordan Journal of Physics
Deanship of Scientific Research and Graduate Studies
Yarmouk University, Irbid, Jordan.
Tel: 00962-2-7211111, Ext. 2075
Fax: 00962-2-7211121
E-mail: jjp@yu.edu.jo

2- **Online**: Follow the instructions at the journal homepage website.

Original *Research Articles*, *Communications* and *Technical Notes* are subject to critical review by minimum of two competent referees. Authors are encouraged to suggest names of competent reviewers. *Feature Articles* in active Physics research fields, in which the author's own contribution and its relationship to other work in the field constitute the main body of the article, appear as a result of an invitation from the Editorial Board, and will be so designated. The author of a *Feature Article* will be asked to provide a clear, concise and critical status report of the field as an introduction to the article. *Review Articles* on active and rapidly changing Physics research fields will also be published. Authors of *Review Articles* are encouraged to submit two-page proposals to the Editor-in-Chief for approval. Manuscripts submitted in *Arabic* should be accompanied by an Abstract and Keywords in English.

Organization of the Manuscript

Manuscripts should be typed double spaced on one side of A4 sheets (21.6 x 27.9 cm) with 3.71 cm margins, using Microsoft Word 2000 or a later version thereof. The author should adhere to the following order of presentation: Article Title, Author(s), Full Address and E-mail, Abstract, PACS and Keywords, Main Text, Acknowledgment. Only the first letters of words in the Title, Headings and Subheadings are capitalized. Headings should be in **bold** while subheadings in *italic* fonts.

Title Page: Includes the title of the article, authors' first names, middle initials and surnames and affiliations. The affiliation should comprise the department, institution (university or company), city, zip code and state and should be typed as a footnote to the author's name. The name and complete mailing address, telephone and fax numbers, and e-mail address of the author responsible for correspondence (designated with an asterisk) should also be included for official use. The title should be carefully, concisely and clearly constructed to highlight the emphasis and content of the manuscript, which is very important for information retrieval.

Abstract: A one paragraph abstract not exceeding 200 words is required, which should be arranged to highlight the purpose, methods used, results and major findings**.**

Keywords: A list of 4-6 keywords, which expresses the precise content of the manuscript for indexing purposes, should follow the abstract.

PACS: Authors should supply one or more relevant PACS-2006 classification codes, (available at http://www.aip.org/pacs/pacs06/pacs06-toc.html)

Introduction: Should present the purpose of the submitted work and its relationship to earlier work in the field, but it should not be an extensive review of the literature (e.g., should not exceed 1 ½ typed pages).

Experimental Methods: Should be sufficiently informative to allow competent reproduction of the experimental procedures presented; yet concise enough not to be repetitive of earlier published procedures.

Results: should present the results clearly and concisely.

Discussion: Should be concise and focus on the interpretation of the results.

Conclusion: Should be a brief account of the major findings of the study not exceeding one typed page.

Acknowledgments: Including those for grant and financial support if any, should be typed in one paragraph directly preceding the References.

References: References should be typed double spaced and numbered sequentially in the order in which they are cited in the text. References should be cited in the text by the appropriate Arabic numerals, enclosed in square brackets. Titles of journals are abbreviated according to list of scientific periodicals. The style and punctuation should conform to the following examples:

1. Journal Article:

a) Heisenberg, W., Z. Phys. 49 (1928) 619.
b) Bednorz, J. G. and Müller, K. A., Z. Phys. B64 (1986) 189
c) Bardeen, J., Cooper, L.N. and Schrieffer, J. R., Phys. Rev. 106 (1957) 162.
d) Asad, J. H., Hijjawi, R. S., Sakaji, A. and Khalifeh, J. M., Int. J. Theor. Phys. 44(4) (2005), 3977.

2. Books with Authors, but no Editors:

a) Kittel, C., "Introduction to Solid State Physics", 8th Ed. (John Wiley and Sons, New York, 2005), chapter 16.
b) Chikazumi, S., C. D. Graham, JR, "Physics of Ferromagnetism", 2nd Ed. (Oxford University Press, Oxford, 1997).

3. Books with Authors and Editors:

a) Allen, P. B. "Dynamical Properties of Solids", Ed. (1), G. K. Horton and A. A. Maradudin (North-Holland, Amsterdam, 1980), p137.
b) Chantrell, R. W. and O'Grady, K., "Magnetic Properities of Fine Particles" Eds. J. L. Dormann and D. Fiorani (North-Holland, Amsterdam, 1992), p103.

4. Technical Report:

Purcell, J. "The Superconducting Magnet System for the 12-Foot Bubble Chamber", report ANL/HEP6813, Argonne Natt. Lab., Argonne, III, (1968).

5. Patent:

Bigham, C. B., Schneider, H. R., US patent 3 925 676 (1975).

6. Thesis:

Mahmood, S. H., Ph.D. Thesis, Michigan State University, (1986), USA (Unpublished).

7. Conference or Symposium Proceedings:

Blandin, A. and Lederer, P. Proc. Intern. Conf. on Magnetism, Nottingham (1964), P.71.

8. Internet Source:

Should include authors' names (if any), title, internet website, URL, and date of access.

9. Prepublication online articles (already accepted for publication):

Should include authors' names (if any), title of digital database, database website, URL, and date of access.

For other types of referenced works, provide sufficient information to enable readers to access them.

Tables: Tables should be numbered with Arabic numerals and referred to by number in the Text (e.g., Table 1). Each table should be typed on a separate page with the legend above the table, while explanatory footnotes, which are indicated by superscript lowercase letters, should be typed below the table.

Illustrations: Figures, drawings, diagrams, charts and photographs are to be numbered in a consecutive series of Arabic numerals in the order in which they are cited in the text. Computer-generated illustrations and good-quality digital photographic prints are accepted. They should be black and white originals (not photocopies) provided on separate pages and identified with their corresponding numbers. Actual size graphics should be provided, which need no further manipulation, with lettering (Arial or Helvetica) not smaller than 8 points, lines no thinner than 0.5 point, and each of uniform density. All colors should be removed from graphics except for those graphics to be considered for publication in color. If graphics are to be submitted digitally, they should conform to the following minimum resolution requirements: 1200 dpi for black and white line art, 600 dpi for grayscale art, and 300 dpi for color art. All graphic files must be saved as TIFF images, and all illustrations must be submitted in the actual size at which they should appear in the journal. Note that good quality hardcopy original illustrations are required for both online and mail submissions of manuscripts.

Text Footnotes: The use of text footnotes is to be avoided. When their use is absolutely necessary, they should be typed at the bottom of the page to which they refer, and should be cited in the text by a superscript asterisk or multiples thereof. Place a line above the footnote, so that it is set off from the text.

Supplementary Material: Authors are encouraged to provide all supplementary materials that may facilitate the review process, including any detailed mathematical derivations that may not appear in whole in the manuscript.

Revised Manuscript and Computer Disks

Following the acceptance of a manuscript for publication and the incorporation of all required revisions, authors should submit an original and one more copy of the final disk containing the complete manuscript typed double spaced in Microsoft Word for Windows 2000 or a later version thereof. All graphic files must be saved as PDF, JPG, or TIFF images.

Allen, P.B., "…………….", in: Horton, G.K., and Muradudin, A. A., (eds.), "Dynamical…….", (North……..), pp….

Reprints

Twenty (20) reprints free of charge are provided to the corresponding author. For orders of more reprints, a reprint order form and prices will be sent with the article proofs, which should be returned directly to the Editor for processing.

Copyright

Submission is an admission by the authors that the manuscript has neither been previously published nor is being considered for publication elsewhere. A statement transferring copyright from the authors to Yarmouk University is required before the manuscript can be accepted for publication. The necessary form for such transfer is supplied by the Editor-in-Chief. Reproduction of any part of the contents of a published work is forbidden without a written permission by the Editor-in-Chief.

Disclaimer

Opinions expressed in this Journal are those of the authors and neither necessarily reflects the opinions of the Editorial Board or the University, nor the policy of the Higher Scientific Research Committee or the Ministry of Higher Education and Scientific Research. The publisher shoulders no responsibility or liability whatsoever for the use or misuse of the information published by JJP.

Indexing

JJP is currently applying for indexing and abstracting to all related International Services.

Jordan Journal of
PHYSICS
An International Peer-Reviewed Research Journal

Volume 7, No. 1, 2014, 1435 H

Table of Contents:

Volume 7, Number 1, 2014. pp. 1-6

Jordan Journal of Physics

ARTICLE

Under Vacuum Photoluminescence Study of Vertically Stacked InAs/GaAs Quantum Dots

Ziad Y. AbuWaar

Department of Physics, The University of Jordan, Amman, 11942, Jordan.

Received on: 23/6/2013; Accepted on: 8/12/2013

Abstract: This work presents a study of photoluminescence (PL) in vacuum from vertically stacked InAs/GaAs quantum dots on (100) N^+ oriented GaAs substrate. A PL system in ultra-high vacuum that was coupled onto a molecular beam epitaxy (MBE) chamber was used in order to avoid the oxidation of the quantum dots. After carrying out the PL of the first layer, the same sample has been returned back to the MBE chamber to grow a second, third, forth and fifth layer of QDs, where after every layer the sample has been taken out of the MBE to the PL system. A clear double peak structure revealing a bimodel size distribution of the QDs has been shown by the power and the temperature dependent PL studies. This bimodel size distribution of the QDs has been also confirmed by an atomic force microscopy (AFM) image.

A blue shift in the PL was observed after the deposition of the second layer due to the generation of a strain field which results in the formation of a second QD layer with different structure and dimensions compared to the first QD layer.

The present observations can help improve understanding the dependence of the optical properties of InAs/GaAs QDs on inter-diffusion of In and Ga atoms during the growth of a new layer due to annealing effect.

Keywords: Photoluminescence; Vacuum; Quantum Dots; InAs / GaAs.

Introduction

Recent interest has been focused on the properties of self-organized InAs/GaAs quantum dots (QDs) due to their potential for electronic and optoelectronic device applications [1- 6]. The size uniformity of the QDs is a major problem which must be solved before high-efficiency devices can be fabricated. To achieve high performance devices, it is essential to understand the rule of thermal treatment of such devices. In view of the fact that thermal treatment may change the strain, composition and size of multiple vertically stacked InAs/GaAs QDs, it is tremendously interesting to look into the thermal effect on the optical properties and on the possibility of improving the size distributions of the QDs[7- 13]. In most cases, results were obtained on vertically stacked InAs/GaAs self – organized QDs, by fabricating the whole stacked QDs without fully understanding the thermal effect on each layer of dots. For this purpose, a PL system in ultra-high vacuum that was coupled onto a molecular beam epitaxy (MBE) chamber was used in order to avoid the oxidation of the quantum dots due to air exposure. After carrying out the PL of the first layer, the same sample has been returned back to the MBE chamber to grow a second, third, forth and fifth layer of QDs, where after every layer the sample has been taken out of the MBE to the PL system. In this paper, I report for the first time in the literature a PL emission from each layer of the same stacked InAs QDs sample.

Corresponding Author: Ziad Y. AbuWaar **Email**: Ziad.abuwaar@ju.edu.jo

Experimental Details

The samples studied here were grown using a solid-source molecular beam epitaxy chamber connected to a PL system under ultra-high vacuum (UHV). A 0.3 μm GaAs buffer layer was grown on (100) N^+ GaAs substrates at 580°C after oxide desorption. This was then followed by 2 ML of InAs and the formation of QDs at 520 °C. The dots were obtained using the Stranski–Krastanov growth mode. Cycles of 0.14 ML of InAs plus a 2 s interruption under As_4 flux were repeated until the total 2 ML of InAs was deposited. The QDs were next annealed for 20 s to improve the QD size distribution. The evolution of the dots was detected using *in situ* reflection high-energy electron diffraction (RHEED). The dots were then capped with 5 nm of GaAs cap layer grown at 520 °C. InAs and GaAs growth rates were set to 0.065 and 1 (ML) s^{-1}, respectively. Then, the sample has been taken outside the MBE chamber to carry out the PL measurements. After that, another layer of InAs QDs has been grown on the same sample, and the same set of PL measurements were performed on the 2 layers of QDs. This process of adding an additional layer of QDs and carrying out PL measurements under vacuum has been repeated until we obtained 5 stacked layers of InAs QDs.

PL measurements were performed in a modified Omicron variable temperature scanning tunneling microscopy (VT-STM) chamber under UHV that was maintained to be better than 10^{-10} Torr. A set of optics inside and outside the VT-STM were used to carry out the PL measurements [14]. The VT-STM chamber was coupled to a Riber MBE system in order to avoid oxidation of the semiconductor surface. The PL measurements were performed over a temperature range of 77–300 K under excitation of a 632.8 nm line of a helium–neon laser. The luminescence was detected by a cooled InP/InGaAs photomultiplier tube (Hamamatsu R5509- 73) mounted on 0.5 m monochromator. To study the surface morphology of the nanostructures, another sample having the same growth conditions with four layers was grown without a capping layer and imaged by an *ex situ* atomic force microscopy AFM. All samples were prepared and experimental tests were performed at the University of Arkansas, Fayetteville, Arkansas.

Results and Discussion

Fig. 1 shows an AFM image of the 4 stacked layers InAs/GaAs QDs. The AFM image and the size profile show a clear bimodel size distribution of the QDs in the studied samples with a typical average dot size of ~ 7 nm in height and ~ 25 nm in diameter. The average QD density is about 2×10^{10} cm^{-2}.

Fig. 2 shows the PL spectra under UHV at 77 K of the stacked InAs/GaAs QDs.

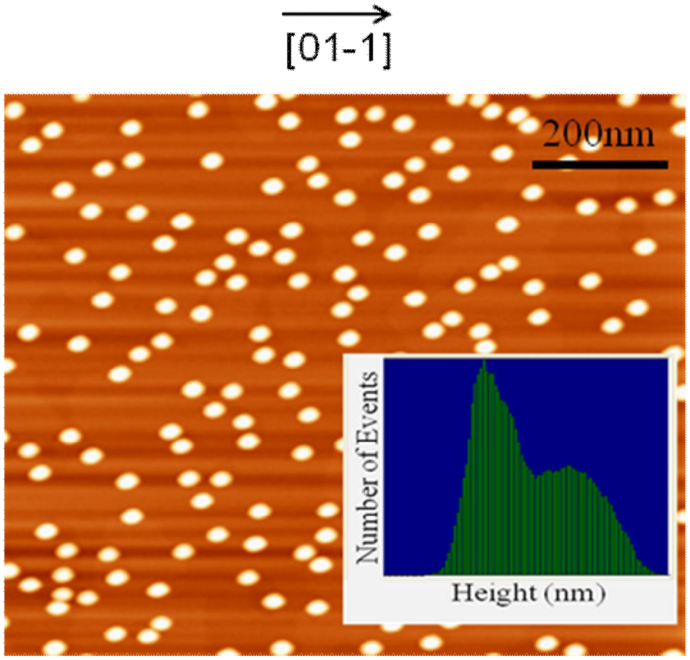

FIG. 1. (1μm×1μm) AFM image and a size profile (bottom right) of the 4 layers InAs/GaAs QDs.

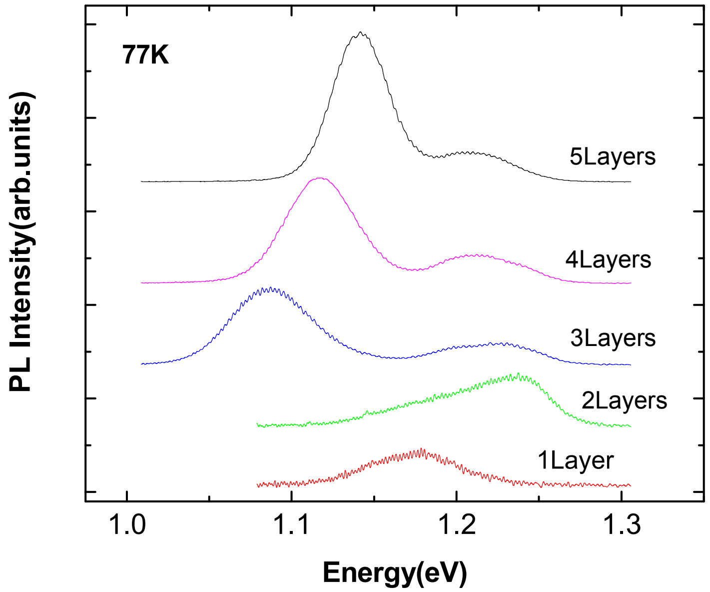

FIG. 2. The PL spectra at 77 K and under UHV of the stacked InAs/GaAs QDs.

For the first layer of QDs, one peak was observed at 1.18 eV. For closely stacked QDs, a blue shift in the PL was observed (E = 1.24 eV) after the deposition of the second layer. I propose that the first QD layer capped with 10 nm GaAs generates a strain field that not only causes vertical alignment but also leads to the formation of a second QD layer with different structure and dimensions compared to the first QD layer. After the deposition of the third layer of QDs, two well separated peaks were observed. The low (E=1.1 eV) and the high (E= 1.24 eV) energy PL peaks after the deposition of the third layer are red-shifted and blue shifted, respectively, from the emission of peak of the first layer PL. These two peaks are associated with larger and smaller dots. The PL spectra after the deposition of the fourth and the fifth layers of QDs showed the same behavior as that after the deposition of the third layer. Form Fig. 2, we can see that for the fourth layer, two PL peaks were observed at E=1.11 eV and at E=1.22 eV, and for the fifth layer, also two PL peaks were observed at E=1.14 eV and at 1.22 eV. PL spectrum of the big dots clearly shifts to higher energies when the number of layers increases while the PL of the small dots does not shift.

The blue shifts of the PL spectra can be explained by inter-diffusion of In and Ga atoms during the growth of a new layer due to the annealing effect [15- 18].

In such more Ga rich dots, the transition energy increases. The Ga diffusion into small dots stops almost after the deposition of the second layer because it approaches saturation values [15, 16].

The power-dependent PL study in Fig. 3 demonstrates that the double peaks from the 4 layers stacked QDs are associated with the ground state emission of islands in different size branches. The temperature dependence of the PL spectra from the 5 layers stacked QDs in Fig. 4 further verifies this assignment.

In Fig. 5, the PL integrated intensity of the two peaks observed in the 5 layers stacked QDs are plotted vs 1/kT. From these plots, the thermal activation energies E_a are determined to be 240 meV and 115 meV for islands in large and small branches, respectively. Different thermal activation energies corresponding to different size islands can be measured for these samples because of the bimodal island size distribution in these samples. Two distinct island size branches coexist and can be identified by simple PL spectroscopy.

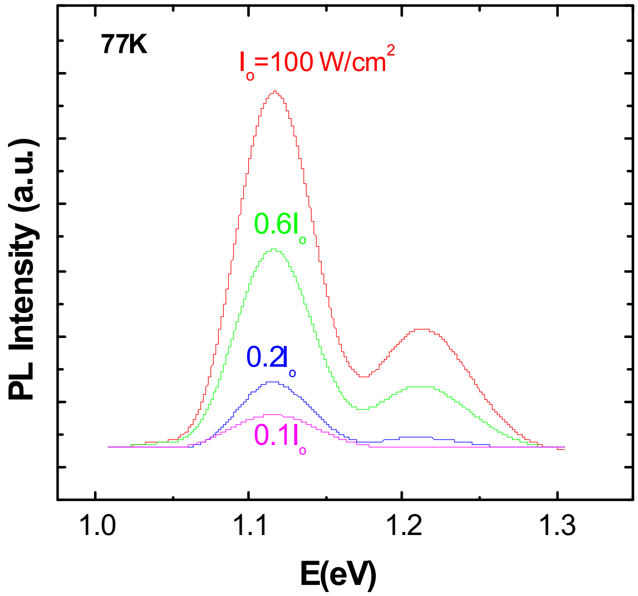

FIG. 3. The power- dependent PL spectra at 77 K and under UHV of the 4 layers stacked InAs/GaAs QDs.

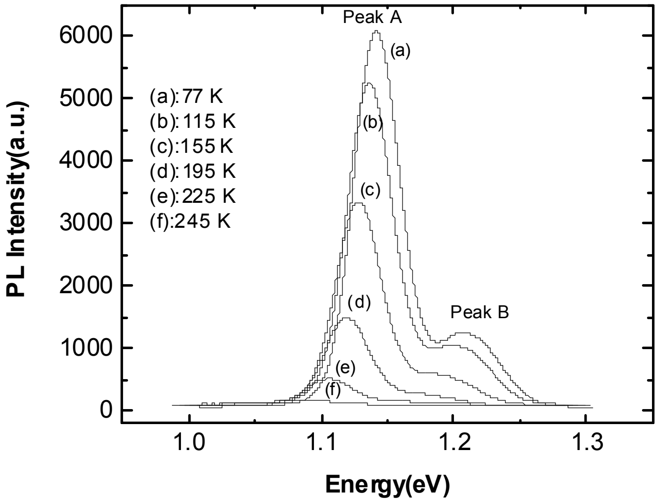

FIG. 4. The temperature dependence of the PL for the 5 layers stacked InAs/GaAs QDs.

Conclusions

The optical properties of vertically stacked InAs / GaAs QDs were investigated by using PL measurement in UHV environment. The power and the temperature dependent PL studies show a clear double peak structure, revealing a bimodel size distribution of the QDs in the studied samples. A bimodel distribution of dot sizes has also been confirmed by an AFM image. After the deposition of the second layer, a blue shift in the PL was observed due to the generation of a strain field which results in the formation of a second QD layer with different structure and dimensions compared to the first QD layer. The blue shifts of the PL spectra for the big dots can be explained by inter-diffusion of In and Ga atoms during the growth of a new layer due to the annealing effect.

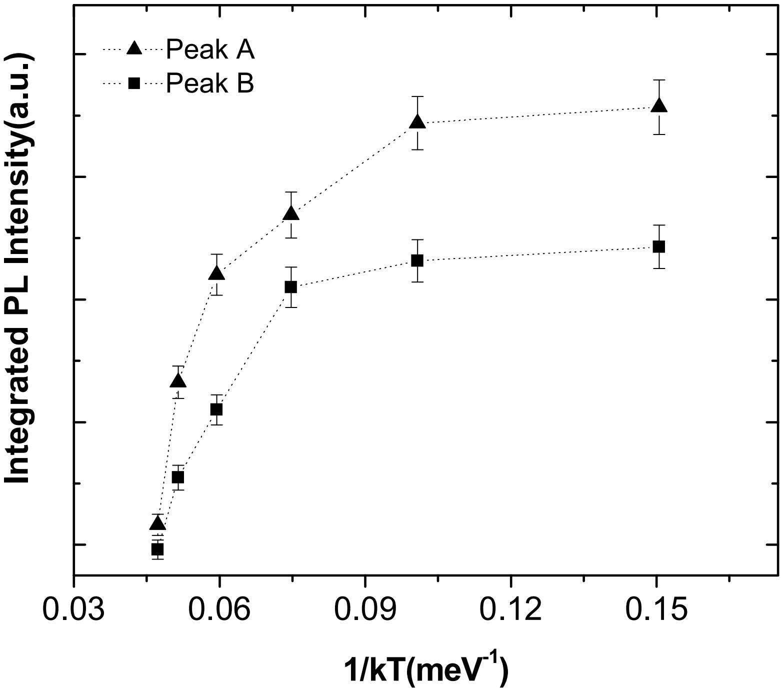

FIG. 5. Plots of PL intensities vs 1/kT from the ground transitions observed in the 5 layers stacked InAs/GaAs QDs.

Acknowledgments

The author acknowledges Gregory J. Salamo group at Arkansas Institute for Nanoscale Materials Science and Engineering, University of Arkansas, Fayetteville, Arkansas 72701, USA, for technical and financial support.

References

[1] Schafer, F., Reithaier, J.P. and Forchel, A., Appl. Phys. Lett., 74 (1999) 2915.

[2] Chu, L., Arzberger, M., Böhm, G. and Abstreiter, G., J. Appl. Phys., 85 (1998) 2355.

[3] Le Ru, E.C., Fack, J. and Murray, R., Phys. Rev. B, 67 (2003) 245318.

[4] Heidemeyer, H., Kiravittaya, S., Müller, C., Jin-Phillipp, N.Y. and Schmidt, O.G., Appl. Phys. Lett., 80 (2002) 1544.

[5] Skiba-Szymanska, J., Jamil, A., Farrer, I., Ward, M.B., Nicoll, C.A., Ellis, D.J.P., Griffiths, J.P., Anderson, D., Jones, G.A.C., Ritchie, D.A. and Shields, A.J., Nanotechnology, 22 (2011) 065302.

[6] Sugaya, T., Kamikawa, Y., Furue, S., Amano, T., Mori, M. and Niki, S., Solar Energy Materials and Solar Cells, 95(1) (2011) 163.

[7] Lee, C.Y., Song, J.D., Lee, Y.T. and Kim, T.W., Solid State Communications, 126 (2003) 421.

[8] Sze, S.M., “VLSI Technology”, (McGraw-Hill, New York, 1988).

[9] Mo, Q.W., Fan, T.W., Gong, Q., Wu, J., Wang, Z.G. and Bai, Y.Q., Appl. Phys., 73 (1998) 3518.

[10] Leonard, D., Krishnamurthy, M., Fafard, S., Merz, J.L. and Petroff, P.M., J. Vac. Sci. Technol., B12 (1994) 1063.

[11] Lee, H., Yang, W. and Sercel, P.C., Phys. Rev. B, 55 (1997) 9757.

[12] Polimeni, A., Patane, A, Capizzi, M., Martelli, F., Nasi, L. and Salviati, G., Phys. Rev. B, 53 (1996) 4213.

[13] Petrov, M.Yu., Ignatiev, I.V., Poltavtsev, S.V., Greilich, A., Bauschulte, A., Yakovlev, D.R. and Bayer, M., Physical Review B, 78 (2008) 045315.

[14] Abu Waar, Z.Y., Marega, E.Jr., Mortazavi, M. and Salamo, G.J., Private Communication.

[15] Lee, H., Lowe-Webb, R., Yang, W. and Sercel, P.C., Appl. Phys., 71 (1997) 2325.

[16] Surkova, T., Patane, A., Eaves, L., Main, P.C., Henini, M., Polimeni, A., Knights, A.P. and Jeynes, C., J. Appl. Phys., 89 (2001) 6044.

[17] Jogai, B., J. Appl. Phys., 88 (2000) 5050.

[18] Jaskolski, W. and Zielinski, M., Physical Review B, 74 (2006) 195339.

Volume 7, Number 1, 2014. pp. 7-12

Jordan Journal of Physics

ARTICLE

Portable Low-Cost CT Scanner Prototype Based on Coincidence Measurements

M. S. Hamideen

Department of Applied Sciences, Faculty of Engineering Technology, Al-Balqa' Applied University, Amman, Jordan.

Received on: 29/5/2013; Accepted on: 26/12/2013

Abstract: A prototype design of Computed Tomography scanner has been tested. The major system employs a gamma ray source, scintillation detectors, a data logger and a three-dimensional sample position controller. The image resolution is determined by the step size and the diameter of the gamma ray beam which is controlled by the pinhole collimator. This device is being designed as a prototype gamma ray scanner with modifications in the type of radiation being used, electronics setup and the rotation and translation techniques. In this scanner, however, the object is rotated instead of the entire detector-radiator system. The type of radiation being used will not be an x-ray tube, but will be an indirect byproduct of Na-22 $^{+}\beta$- decay. This source emits positrons at the surface of the object which rapidly annihilate with atomic electrons that result in the emission of 2 back-to back 511 keV annihilation photons that can be used to electronically require coincidence between gamma detections and therefore reduce background radiation being detected. It is obvious that tomographic imaging is a complex procedure, thus, the main motivation of the work is to prove the capabilities and performances of a prototype CT scanner based on coincidence measurements, as an imaging system.

Keywords: Coincidence Measurements; CT scanner, Prototype Design; Annihilation Photons.
PACS: 81.70.Tx.

Introduction

Computed Tomography (CT) is a method of constructing a two-dimensional (2D) image of the internal structure of a solid body. This method uses computers to construct an image using information obtained from photons that have passed through the body from multiple angles. The algorithms used to calculate the images are called image reconstruction from projection algorithms [1]. There are two categories for image reconstruction algorithms, the analytical algorithms and the iterative algorithms [2]. Analytical algorithms have been popularly used for modern 1st - 4th generation CT, because modern CT has to process a large amount of projection data. On the other hand, iterative methods are slow but more accurate than analytical methods. Iterative algorithms can be divided into algebraic algorithms and statistical algorithms [3]. For image reconstruction in this work, filtered back projection [4] or iterative algorithms can be used. Iterative algorithms were chosen because projection data are small. Among statistical algorithms, EM (Expectation Maximization) [5] is used for image reconstruction in this paper. Computed tomography (CT) was first introduced into medical sciences, and lately with the success of the technique, CT began to be used in other areas of knowledge [6, 7, 8]. For example, Pires *et al.* showed that scanning of soil samples was performed with a first generation CT scanner with fixed source–detector arrangement and translation/rotational movements of the samples [9].

Corresponding Author: M. S. Hamideen **Email**: mhamideen@fet.edu.jo, mhamideen@bau.edu.jo

The new design that is being built differs from standard computed tomography scanners in both the radiation source and the translation/rotation method [10]. First, most computed tomography scanners use x-rays generated by the use of a hot cathode x-ray tube. These x-rays are collimated to produce a beam. The new design, however, will not use x-rays but annihilation photons produced by a Na-22 source. This source emits positrons at the surface of the object which rapidly annihilate with atomic electrons that result in the emission of 2 back-to back 511 keV annihilation photons that can be used to electronically require coincidence between gamma detections and therefore reduce background radiation being detected [11]. The reduction of background radiation allows the radiation source to be less active, since the signal does not need to compete with background noise [12]. The second difference in the new design is the way the transmission beam being rotated and translated across the object. In most computed tomography scanners, the object being scanned must remain motionless. This is a requirement, for example, if the object is a human. However, since our preliminary design will not be used on humans, the object itself will be rotated and translated. This change simplifies the mechanical apparatus, since it requires only one object to move rather than rotating and translating both the detectors and the source. Other advantages of the scanner include lower cost and that it would be more portable, as well as that the relatively small size and lack of lead shielding required by the scanner would allow it to be transported by workers to remote areas.

The disadvantages might include the higher energy annihilation photons involved and the more complicated electronics for each in-line detector channel. The more complicated electronics would make repair more difficult to perform. The imaging time would also be very slow compared to modern-day scanners.

Experimental Work

The present measurements are performed using Na-22 radioactive source with an activity of 1μCi. The source is placed in front of data detector (detector 2) as shown in Fig. 1. The energy transition that is being made to change Na-22 nuclei into Ne-22 nuclei is a 1.274 MeV gap that must be jumped by emitting a 1.274 MeV particle. 90.05% of the time, the Na-22 nucleus emits a 1.274 MeV positron. The Na-22 nucleus will also emit a 1.274 MeV gamma ray in order to make the transition. Due to atomic electrons, the positron will then be captured to form positronium. This positron-electron annihilation results in the production of two back-to-back 511 keV annihilation photons. We can use this fact to our advantage when building a computed tomography scanner. Each annihilation photon that reaches the detector has a annihilation photon traveling in the opposite direction. By placing the coincidence detector (detector1) behind the Na-22 source and directly across from the data detector, an electronic setup can be built that will require a coincidence between a transmitted annihilation photon and the corresponding annihilation photon traveling in the opposite direction. In requiring such a coincidence, the majority of background events can be eliminated. Instead of requiring a very intense source to produce a useable signal to noise ratio by enhancing the signal, the signal-to-noise ratio is maintained by reducing the background noise. Therefore, a weaker and safer source can be used.

The mechanical part of the scanner which was built in the workshop of the Department of Physics/ University of Jordan is a complex sample holder driven by three powerful stepper motors; (M1, M2 and M3), all fixed onto a main metallic frame, and controlled by computer software. The first motor drives the sample in a forward and backward direction on a 20 cm linear track. The second stepper motor is used to rotate the sample holder to any angular position, from 1° to 360°. In a similar way, the third stepper motor is used to allow up and down translational motion of the sample holder, as shown in Fig. 2.

Measurements were taken to begin construction of this novel design, and the performance of the scanner is tested by scanning a cylindrical vessel of water (density = 1g/cm^3) of 10cm diameter and a steel nut (density = 7.85 g/cm^3) of 5cm inner diameter and 10cm outer diameter. The capability of this proposed setup to distinguish between different densities can be highlighted.

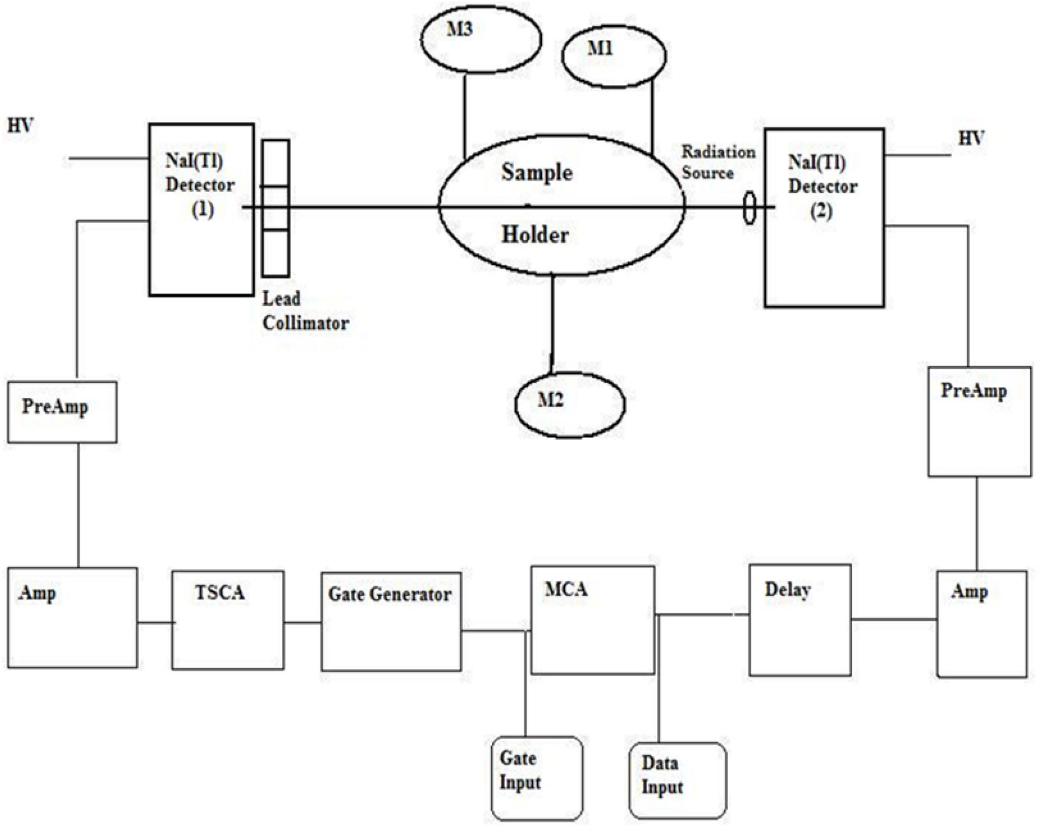

FIG. 1. A schematic diagram showing the electronic circuit involved in data collection.

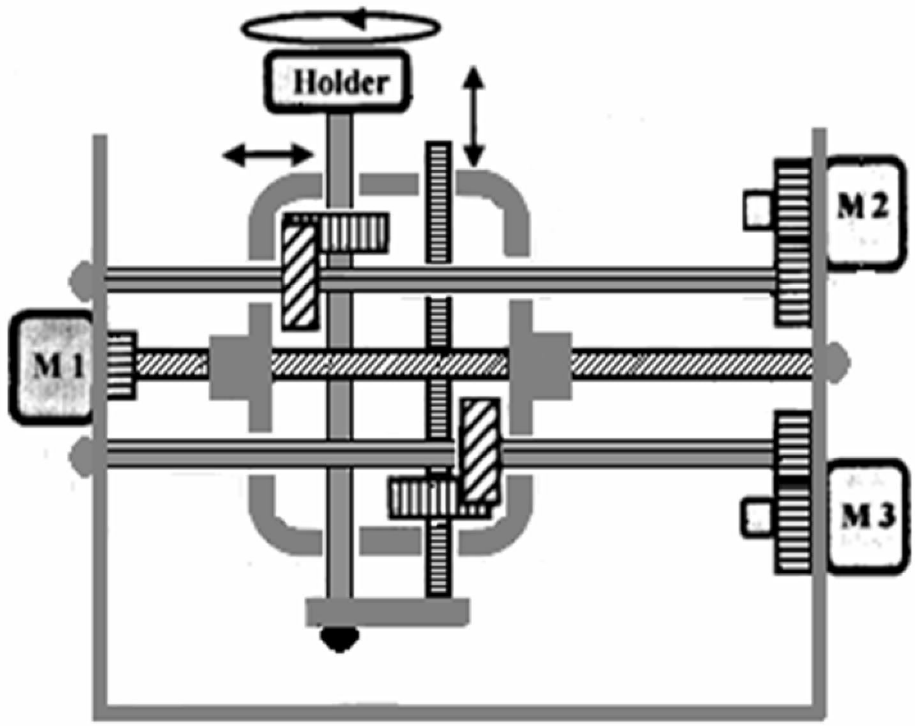

FIG. 2. Mechanical construction showing the side view of the scanner.

Results and Discussion

The energy resolution of the detectors was measured and calculated. Both detectors collected the energy spectrum of Na-22 source, and using this spectrum the energy resolution of the detectors was found 8.4% and 9.5% for the coincidence and data detectors, respectively.

Spatial resolution is described by the full width at half maximum (FWHM) complemented by the full width at tenth maximum (FWTM) of the line spread function of the detector. The limit of the spatial resolution is set by the intrinsic resolution, R_i. It describes the ability of the system to transfer the spatial distribution of the absorbed energy in the detector to a readable image, and it depends primarily on the statistical fluctuation in the number of light photons hitting the detector [11]. The spatial resolution is also heavily dependent on the collimator resolution R_c, and for high resolution the collimator holes should be as long and narrow as possible. R_c is dependent on the distance from the collimator, and the value of R_c increases in an approximately linear manner with increased distance for a parallel-hole collimator. Therefore, it is important that the collimator is as close to the sample as possible. Spatial resolution is also dependent on scatter and septal penetration, to a less degree, and the contribution of these effects is called R_{sc}. The total spatial resolution can be calculated as:

$$R_{tot.} = \sqrt{R_i + R_c + R_{sc}} \quad (1)$$

In this work, the full width at half maximum (FWHM) has been measured for the spectrum several attempts sufficient to collect a spectrum on a multi- channel analyzer (MCA), and the average value was 5mm. Although it is not a good result, it is suitable enough for a home-made scanner.

Data collection time, in this case, is mostly dependent on the amount of time it will take to collect enough data for each measurement in order to acquire a particular amount of error for that data. While measuring the number of annihilation photons, there is a statistical error equal to the square root of the number of counts. In this work, the accepted error is ten percent; therefore each measurement will require one hundred counts. The number of gamma detections can be calculated using the next formula [11].

$$N_{det.}=N[(\frac{\Delta\Omega}{4\Pi})(\varepsilon_1)(\varepsilon_2)(C_1)(C_2)\mathrm{Exp}[-\mu x]] \quad (2)$$

where N is the number of disintegrations in the nucleus resulting in at least one gamma emission which was known to be $3.7\mathrm{x}10^4$ disintegrations per second, $\frac{\Delta\Omega}{4\Pi}$ is the geometric solid angle of the detections, $\varepsilon_1$and ε_2 are the detector's efficiency that can be determined for this type of detectors to be 64% [11].

C_1 and C_2 are the photopeak fractions of both detectors which were measured to be 40%, μ is the coefficient of attenuation for the material being scanned and x is the distance through which the annihilation photons have to travel. Calculations of the geometric solid angle of the detections are made depending on using one micro-Curie Na-22 source. The calculated value is approximately $1.29\mathrm{x}10^{-4}$. Arranging the last calculations, the number of detected radiations can be calculated, and the average time required for each measurement is 841.75 seconds. In this work, 20 translations are required to completely cover the scanned body of water. The number of rotations required for this particular setup is determined. In a higher resolution scanner, there would be one rotation for every degree in a half circle. However, since the width of the beam in this case is larger, it will require more rotation per angle in order to avoid overlap. The beam angle is rotated 5.74 degrees which requires 32 rotations. The whole number of translational and rotational measurements has been calculated. The total time required to perform the scan is determined to be 538720 seconds. This is equal to 6.23 days of continuous scanning.

Fig. 3 shows the reconstructed image of the water body using the (EM) reconstruction method on a matrix of 64x64 pixels. The image shows that the examined cross-sectional views of the sample (transverse planes) have a homogeneous density which describes the water content of the vessel. In spite of the limitation of the imaging time and spatial resolution of the proposed system, the reconstructed image is reasonable.

Fig. 4 shows another example of the scanner output of a reconstructed image of a steel nut of 5cm inner diameter and 10cm outer one by the same reconstruction method. The images demonstrate the good image quality obtained by the scanner and its ability to distinguish between different densities.

The last two images can be taken in the saggital and coronal planes, which are left as a future work, since we are interested now in testing the performance of this design in transverse plane.

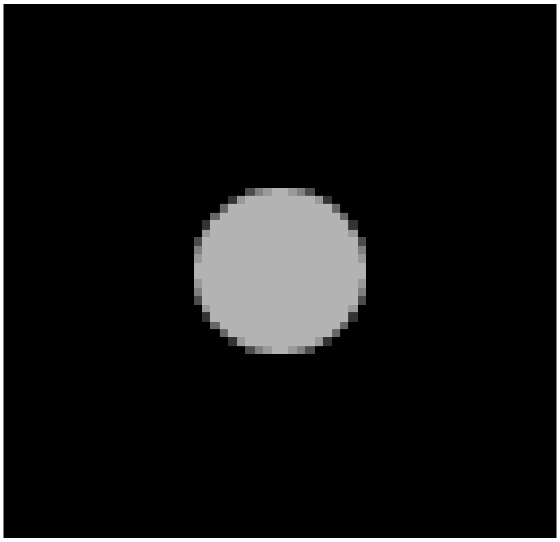

FIG. 3. A reconstructed image of a cylindrical vessel of water.

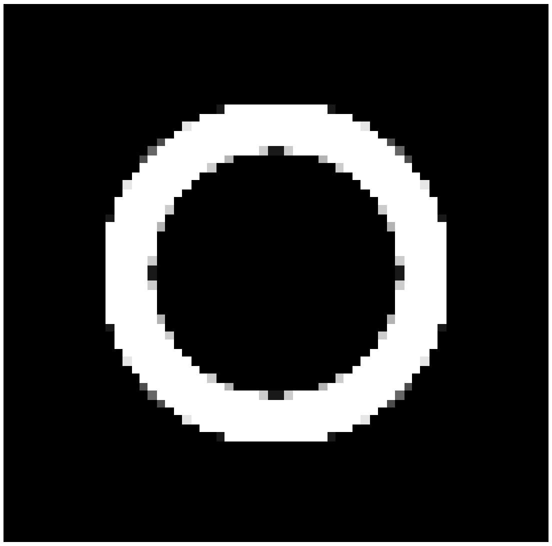

FIG. 4. A reconstructed image of a steel nut.

Conclusions

The energy resolution was found 8.4% for detector (1) and 9.5% for detector (2). Spatial resolution and detector efficiencies were determined. Through a series of calculations, it was found that a complete scan using the condition described would theoretically take about 6.23 days. Although it is not a good result, it is suitable enough for this appropriate design of scanners.

In spite of the limitation of the imaging time and spatial resolution of the proposed system, the reconstructed images are reasonable and can be considered as a novelty compared to those obtained from other standard transmission CT scanners.

The collimation and filtering out background noise could also be achieved by using the combination of the coincidence detector and data detector.

Acknowledgment

The author would like to thank some of his colleagues, especially Dr. Assad Sakhel for his helpful discussions in the reconstruction software.

References

[1] Oldendorf, W., IEEE Trans. Biomed. Electron., 8 (1961) 68.

[2] Herman, G., "Reconstruction from Projections: The Fundamentals of Computerized Tomography". (Academic Press, 1980).

[3] Kak, C. and Slaney, M., "Principles of Computerized Tomographic Imaging". (New York IEEE Press, 1988).

[4] Dreik, P. and Boyd, D., Comput. Graph. Image Process, 5 (1976) 459–469.

[5] Cattle, B.A., Ann. Nucl. Energy, 34 (2007) 591–599.

[6] Lange, K. and Carson, R., J. Comput. Assist. Tomo., 8 (1984), 306–316.

[7] Peele, A.G., Quiney, H.M., Dhal, B.B., Mancuso, A.P., Arhatari, B. and Nugent, K.A., Radiat. Phys. Chem., 75 (2006) 2067–2071.

[8] Masschaele, B., Dierick,M., Cnudde, V., van Hoorebeke, L., Delputte, S., Gildemeister, R., Gaehler, R. and Hillenbach, A., Radiat. Phys. Chem., 71 (2004) 807–808.

[9] Pires, L.F., Ca´ssaro, F.A.M., Bacchi, O.O.S. and Reichardt, K., Rad. Phys. Chem., 80 (2011) 561–566.

[10] Hamideen, M., Sharaf, J., Al-Saleh, K. and Shaderma, M., Radiat. Phys. Chem., 80 (2011) 1162–1165.

[11] Glenn F. Knoll, "Radiation Detection and Measurements". (John Wiley and Sons, 1988).

[12] Lopes, R., Costa, E. and de Jesus, O., App. Radiat. Isot., 53 (2000) 665-671.

Volume 7, Number 1, 2014. pp. 13-22

Jordan Journal of Physics

ARTICLE

Preparation and Characterization of Binary Polymer Blend Reinforced with Polypropylene, Carbon and Hybrid Fibers

Awham M. Hameed and **Nada R. Kareem**

Department of Applied Sciences, University of Technology, Baghdad, Iraq.

Received on: 3/10/2013; Accepted on: 26/12/2013

Abstract: In this study, a binary polymer blend was prepared and characterized before and after the reinforcement with polypropylene, carbon fibers and hybrid of both types. Epoxy/polyvinyl chloride (EP/PVC) blends were prepared with different weight ratios including (0, 5, 10, 15 and 20)% of (PVC). The influence of addition of (PVC) on the mechanical properties of epoxy resin was examined. The microstructure and impact fracture surfaces of the blends and their composites were investigated by scanning electron microscope (SEM). The experimental results show that the mixing ratio of 20% (PVC) has the highest impact strength compared to other ratios. The percentage (80/20) % of (EP/PVC) reinforced with carbon fibers records the highest values for both impact strength (I.S.) and Young's modulus (E); while the hybrid composite has higher Shore D hardness compared with other composites prepared from the same blend.

Keywords: Polymer Blend; Miscibility; Epoxy; PVC; Composites; Mechanical Properties.

Introduction

Polymer blending is a convenient and attractive route for obtaining new polymeric materials. The polymer blending offers the possibility of adjusting the cost-performance balance and tailoring the technology to make products for specific end user applications, enhancing resins' performance, improving specific properties, *viz*. impact strength, solvent resistance… etc. and provide means for industrial and consumer plastics waste recycling. However, this approach is complicated by the fact that polymers are generally thermodynamically immiscible. Thus, achieving compatibilization in immiscible polymer blends has been a long-standing academic and technological challenge [1].

When any two materials are mixed together, or blended, the properties of the resulting mixture depend on the level at which intimate mixing takes place and on whether any chemical reactions between the components of the mixture take place [2].

Two or more existing polymers may be blended for various reasons. One reason is to achieve a material that has a combination of the properties of the constituents, e.g. a blend of two polymers, one of which is chemically resistant and the other is tough. Another reason is to save costs by blending a high-performance polymer with a cheaper material. A very important use of blending is the combination of an elastomer with a rigid polymer in order to reduce the brittleness of the rigid polymer [2].

A miscible polymer blend is one for which the miscibility and homogeneity extend down to the molecular level, so that there is no phase separation. An immiscible blend is one for which phase separation occurs [3].

Polymer blend (PB) is a mixture of at least two polymers or copolymers. It is a physical mixture of two or more polymers with/without any chemical bonding between them [2].

Corresponding Author: Nada R. Kareem **Email**: nada.kammona@yahoo.com

Basically, there are three different types of blends depending on miscibility [4, 5]:

1. Completely miscible blends have ($\Delta G < 0$) due to specific interaction.

Homogeneity is observed at least on a nanometer scale, if not on the molecular level. This type of blend exhibits only one glass transition temperature (Tg), which is in between the glass transition temperatures of the blend components in a close relation to the blend composition.

2. In partially miscible blends, a small part of one of the blend components is dissolved in the other part. This type of blend, which exhibits a fine phase morphology and satisfactory properties, is referred to as compatible. Both blend phases are homogeneous and have their own Tg. Both Tg_s are shifted from the values for the pure blend components towards the Tg of the blend component.

3. Fully immiscible blends have a coarse morphology, sharp interface and poor adhesion between the blend phases. So, these blends are of no use without compatibilization.

A composite is a structural material that consists of two or more combined constituents that are combined at a macroscopic level and are not soluble in each other. One constituent is called the (reinforcing phase) and the one in which it is embedded is called the (matrix) [6].

The most common advanced composites are polymer matrix composites (PMCs) consisting of a polymer (e.g., epoxy, polyester, urethane) reinforced by thin diameter fibers (e.g., graphite, aramids, boron). For example, graphite/ epoxy composites are approximately five times stronger than steel on a weight for- weight basis. The reasons why they are the most common composites include their low cost, high strength and simple manufacturing principles [7].

The importance of polymer blends has been demonstrated in recent years by the intensive research carried out on the subject, the increasing amount of articles, patents and books being continuously published and the introduction of polymer blends for practical uses [8].

D. Feldman *et al.*[9] modified the epoxy polymer (EP) by incorporation of dibutyl phthalate (DBP), poly vinyl chloride (PVC), polyvinyl alcohol (PVA) and glass fiber reinforcement. Results indicated that EP and DBP are miscible in the proportions used in the work (up to 10% of DBP). PVA added to cure EP in a concentration of 10% occurs as a separate phase. The morphology of EP–PVC blends is relatively complex; EP and PVC are immiscible at low concentration of the second component (up to 10% of PVC), but become mutually and increasingly more miscible as the concentration of PVC increases. Incorporation of DBP into EP causes a marked reduction in the heat distortion temperature (HDT), whereas the addition of PVC has only a moderate effect.

Cao *et al.* [10] studied the mechanical properties of an epoxy resin toughened by polyester. The results showed that the impact strength and tensile strength of the modified epoxy resin were remarkably greater than those of the unmodified cured epoxy resin and the mechanical properties depended greatly on the congregating state of the polyester added.

Shokrieh *et al.*[11] have studied the mechanical properties of multi-walled carbon nanotube (CNTs) /polyester nanocomposites. They found that adding CNTs into polymers at very low weight fractions can improve mechanical properties of the resulting nanocomposites. The results of mechanical tests (tensile and flexural) exhibit improvements of tensile and flexural strengths by 6% and 20%, respectively, at only 0.05 wt.% MWCNT (multi-walled carbon nanotubes). Improvements in Young's modulus and flexural modulus were also observed.

Epoxy resin is a brittle material and has low impact strength in many applications. For this reason, there are two main aims of the current study, the first aim is carrying out some modification in properties of resin material (epoxy, EP) by adding thermoplastic material (Poly Vinyl Chloride, (PVC)) with different weight ratios to prepare binary polymer blend. The second aim is to study some of mechanical properties for these blends before and after the reinforcement with polymer fibers (polypropylene fibers), ceramic fibers (carbon fibers) and hybrid fibers of the previous two types.

Experimental Part

The Materials Used

The following materials were used for preparing the specimens of polymer blends and their composites:

Matrix material: Two types of polymers were used in this study; the first is epoxy resin (EP) as thermosetting material, while the other is PolyVinyl Chloride (PVC) as thermoplastic material.

Epoxy resin (EP): Epoxy resin of type (Quickmast 105) was used in this work; it is a liquid with moderate viscosity. This resin could be converted to the solid state by adding a hardener.

PolyVinyl Chloride (PVC): In this study, a white powder of (PVC) produced by (Hyundai company) was used to prepare the polymer blend after dissolving it with (cyclohexanon). The molecular weight of PVC is about 62.05g/mol.

Reinforcement materials: Three types of fibrous reinforcement were used in this work.

1- Carbon fibers

Chopped carbon fibers as ceramic fibers were used to reinforce the selected polymer blend (80/20)% of (EP/PVC).

2-Polypropylene fibers

Chopped polypropylene fibers as polymer fibers were used to reinforce the polymer blend under study.

3-Hybrid fibers

The above two fibers were mixed together to reinforce the prepared polymer blend.

Blends and Composites Preparation

1- Before the casting process, polymer sheets (transparent papers) were prepared as molds with dimensions (15*20*2) cm^3.

2-PVC powder was sieved using (Retsch) sieve produced by UK company with three particle sizes including (25, 45 and 63) micron, it was found that the particle size of PVC powder is about (63micron).

3- After dissolving (PVC) powder in its solvent (cyclohexanon), epoxy resin was mixed with PVC at different percentages to prepare the binary polymer blend casts.

4- Five sheets of (epoxy / PVC) blend with different weight ratios (0%, 5%, 10%, 15%, and 20%) of PVC were prepared, respectively.

5- These sheets were left at room temperature for (24 / hours) and then removed from the molds after completing the solidification process; the casts were put into an oven at (50^oC) for (1 hour) to complete the curing process.

6- The homogeneity case of these blends was tested by using scanning electron microscope (SEM).

7- It was found that the best ratio of mixing between the two polymers is (80/20)% which exhibits the compatibility case between them.

8- The selected ratio was reinforced with three kinds of fibrous reinforcement including (carbon, polypropylene and a hybrid of both of them).

9- The rule of mixture (equation 1) [12] was applied for calculating the volume fraction of fibers (φ) for the composites. The reinforcement process was carried out by the addition of a layer of polymer blend inside the prepared molds previously, and then the chopped fibers were arranged uniformly into these molds above this layer. Finally, the remaining amount of the polymer blends was poured above the arranged fibers.

$$\Phi = \frac{1}{1+\left(\frac{1-\Psi}{\Psi}\right)\times\left(\frac{\rho_f}{\rho_m}\right)} \qquad (1)$$

where (Φ, Ψ) are the volume and weight fractions of the fibres, respectively, (ρ_f, ρ_m) are the density of fibres and the density of matrix, respectively.

The density of the prepared blends was determined from the following equation [8]:

$$\rho_m = X_1\rho_1 + X_2\rho_2 \qquad (2)$$

where ρ_m: the density of the matrix (polymer blends), ρ_1, ρ_2: the density of the first polymer and the second polymer, respectively and X_1, X_2: the percentage of the first polymer that of and the second polymer, respectively.

10- The previous step was repeated with the three different types of reinforcement under study.

11- Step (5) was repeated for the three reinforced casts. It is important to mention that the volume fraction of fibers is (30) % for the single reinforcement, but equal to (15%) of carbon fibers (C.F.) and (15%) of polypropylene fibers (P.P.F.) for the reinforcement with hybrid fibers (H.F.) to obtain constant fiber volume fraction for each case of reinforcement.

12- According to the standard specifications (ISO and ASTM), the samples of impact, bending and hardness tests were cut and their properties were tested at room temperature. The prepared specimens are shown in Figs. 1, 2 and 3.

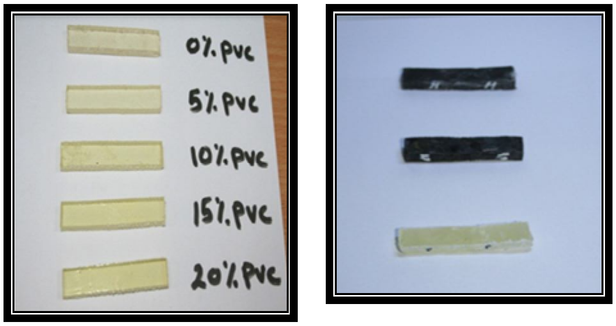

(a) (b)

FIG. 1. Impact test samples before and after the reinforcement, respectively.

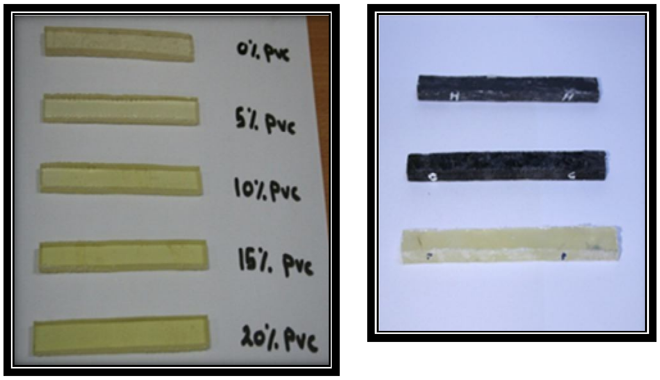

(a) (b)

FIG. 2. Bending test samples before and after the reinforcement, respectively.

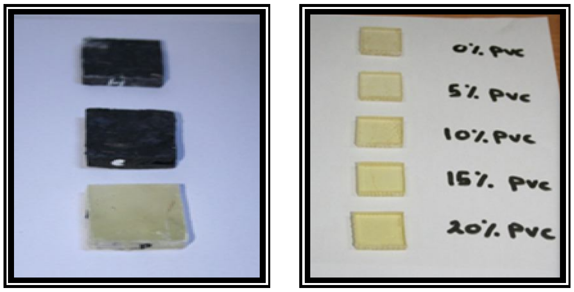

(a) (b)

FIG. 3. Hardness samples before and after the reinforcement, respectively.

Mechanical Testing

Impact Test

Charpy impact test instrument was used to determine the impact energy of the prepared samples before and after the reinforcement.

The technique of the instrument is conducted through lifting up the hammer to the highest point and fixing it well, and then the sample is placed in its position.

The potential energy by a swinging movement will change to kinetic energy and loses part of it in breaking the sample; the pointer of gauge will read the energy value required to break the sample.

Impact strength (I.S.) is calculated by the relation [13]:

$$I.S. = \frac{Uc}{A} \quad (3)\ (\mathrm{J/m^2})$$

I.S.: impact strength;

Uc: the energy of fracture (Joule);

A: the cross-sectional area of the sample (m^2).

Bending Test Instrument

Three-point bending test instrument was used to measure the Young's moduli of polymer blend samples before and after the reinforcement. The sample was fixed at the two ends on the support of the instrument, and then the weights were added gradually to the hanger which was placed at the middle of the sample. From the reading dial gauge, the deflection amount of the sample was determined.

The values of Young’s moduli are calculated from the following relations [13]:

$$I = \frac{b \times t^3}{12} \quad (4)\ \mathrm{mm^4}$$

where (I) is the moment of inertia, (b) is the width of the sample, (t) is the thickness of the sample. Young's modulus (E) is calculated using equation (5).

$$E = \frac{M \times g \times L^3}{48 \times I \times S} \quad (5)$$

where (M / S) is the slope of the curve obtained from the relationship between the mass (M) and the deflection (S) of each sample, g = 9.8 m/ s^2, L is the distance between two supports which is equal to (10 cm).

Hardness Test Instrument

Shore D hardness instrument (digital, Italy, type TH210) was used to measure the hardness values of the specimens. This test was carried out by fixing a dibbing tool on the surface of the sample. The dibbing tool length is about 2.54 mm. The pointed dibbing tool penetrates into the material surface, and then the number value of hardness is shown on a digital screen.

Morphology Studies

Scanning electron microscope (SEM, model 7426 manufactured by OXFORD company) was used to study the morphology and fracture surface nature of the impact test specimens.

Results and discussion

Impact Properties

Charpy impact test was used to evaluate the impact strength of the (EP/PVC) blends with different weight ratios of (PVC) including (0, 5, 10, 15 and 20%). Fig. 4 shows the effect of PVC percentages on the impact strength (*I.S.*) values of the prepared blends. From these results, it can be observed that the impact strength (*I.S.*) values decrease at the first addition ratios of PVC and then increase at percentages above (15%). This increase may be attributed to the compatibilization between epoxy and PVC at this ratio of mixing as well as the second phase of (PVC) affects the (*I.S.*) because the particles of (PVC) act as an energy absorber and improve the impact strength of the blend [14].

Fig. (5) illustrates the values of (*I.S.*) of (EP/PVC) reinforced with P.P.F, C.F. and H.F. It can be seen that carbon fibers (C.F.) give higher values of (*I.S.*). This means that (C.F.) need higher fracture energy before fracture which leads to increase the toughness of this composite where one definition of material toughness is the amount of energy per volume that a material can absorb before breaking. It is also defined as the resistance to fracture of a material when stressed [3].

In general, previous studies [6, 15, 16] were indicated that cured epoxy with other polymer phases exhibits two microstructure phases consisting of small particles of the added phase.

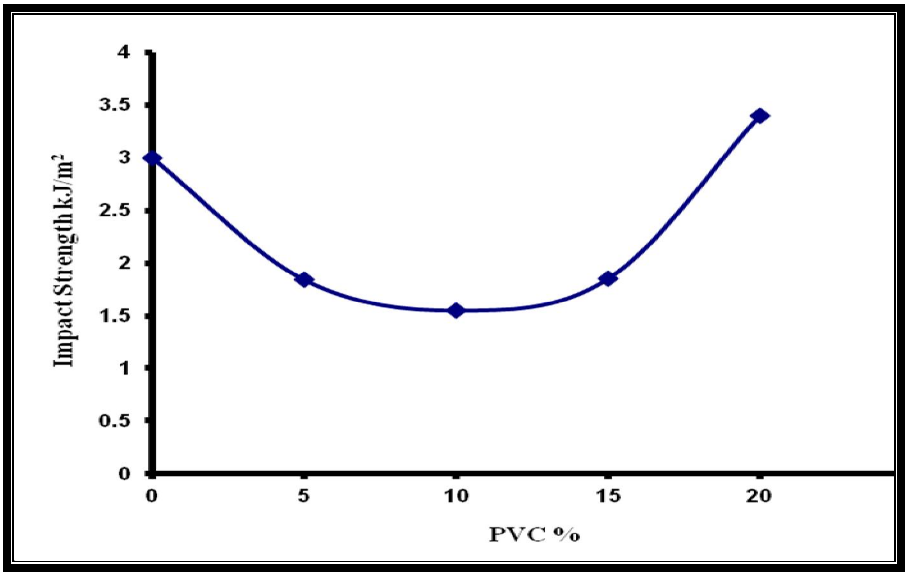

FIG. 4. Effect of (PVC%) on the impact strength of (EP/PVC) polymer blend.

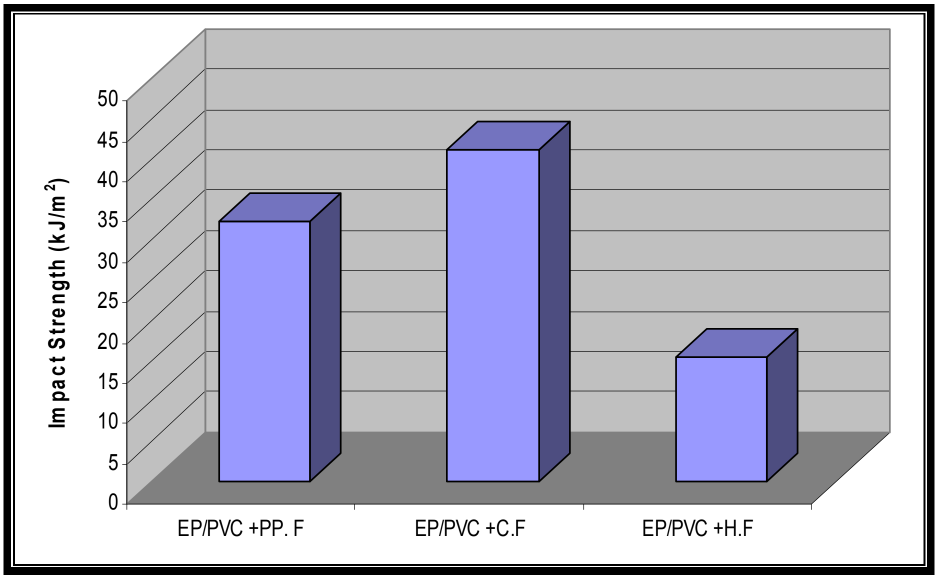

FIG. 5. Impact strength of (EP/PVC) composites.

The morphology of fracture surfaces for pure epoxy, blends and their composites can be observed from Figs. 6(a-e) and 7(a-c), respectively. Fig. 6a illustrates the nature of single phase of pure epoxy. The neat blend sample of (5%PVC) shows brittle fracture surface, indicative of miscible characteristics between the epoxy and PVC as shown in Fig.(6b). In Figs. (6c-e), it is observed that fracture surface was rather coarse and turned to ductile fracture behaviour due to higher addition of PVC. In Fig. (6e), another strong ductile fracture surface can be observed, which gives an indication of good dispersion of (PVC) phase that improves the impact strength at 20wt.% of (PVC). It can be concluded that the plasticity case of the blend will increase and become best at mixing of 20% of PVC.

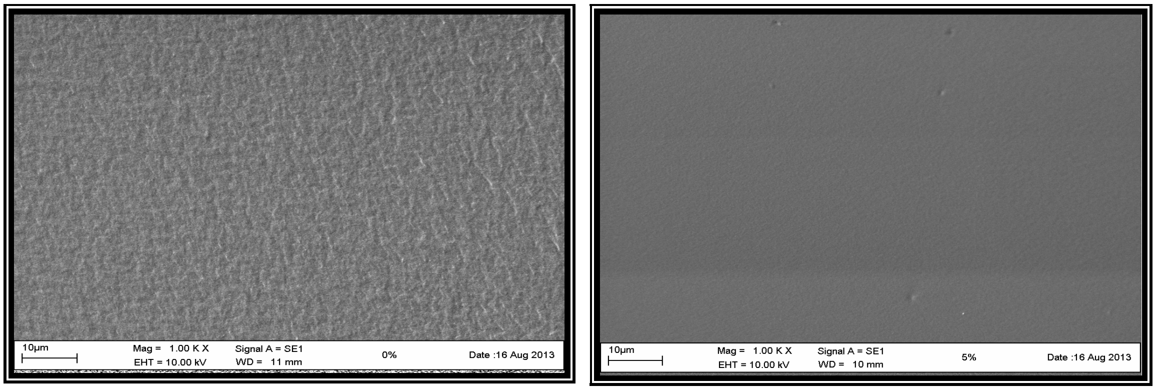

(a) 0% PVC (b) 5% PVC

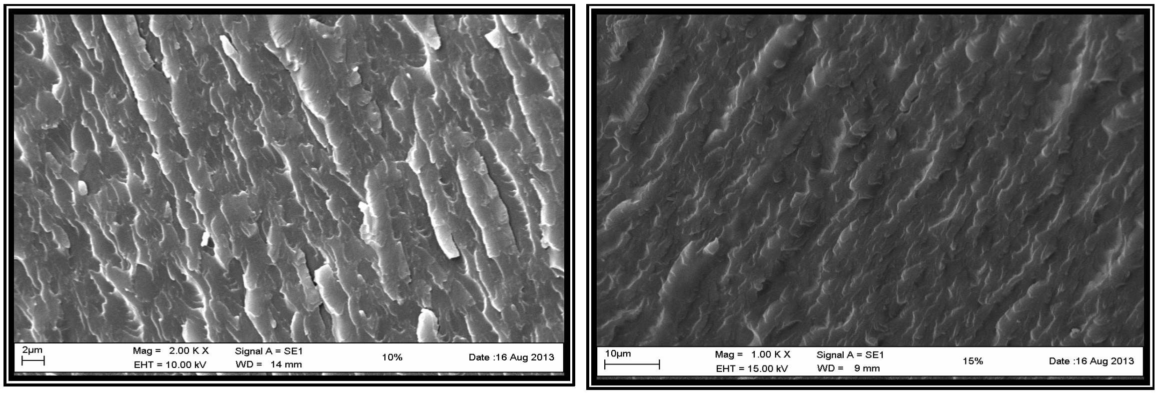

(c) 10% PVC (d) 15% PVC

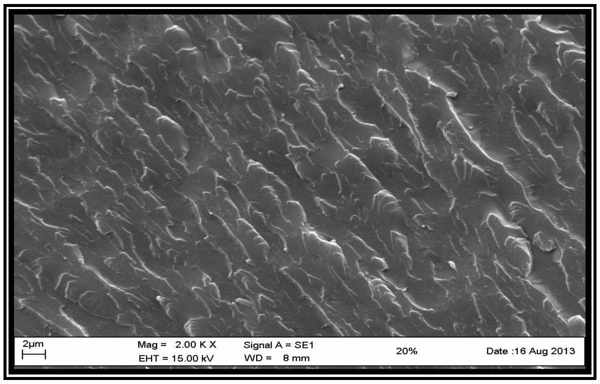

(e) 20% PVC

FIG. 6. SEM micrographs of fracture surfaces for (EP/PVC) blends.

From the micrographs of fracture surfaces for the composites shown in Figs. (7a-b), respectively, it can be recognized that carbon fibers break with brittle manner, while (P.P.F) fractures in ductile mode deform with buckling. It can also be noticed that (C.F.) have smooth fracture surfaces, implying brittle fracture mode, but there is pronounced bending that precedes the fracture and final separation occurs after a large amount of local drawing for (P.P.F.). In contrast, carbon fibers fracture without any reduction in cross-sectional area [12].

The fracture surface of (H.F.) involves both above cases with some fibrillation and kink formation of fibers as shown in Fig. (7c).

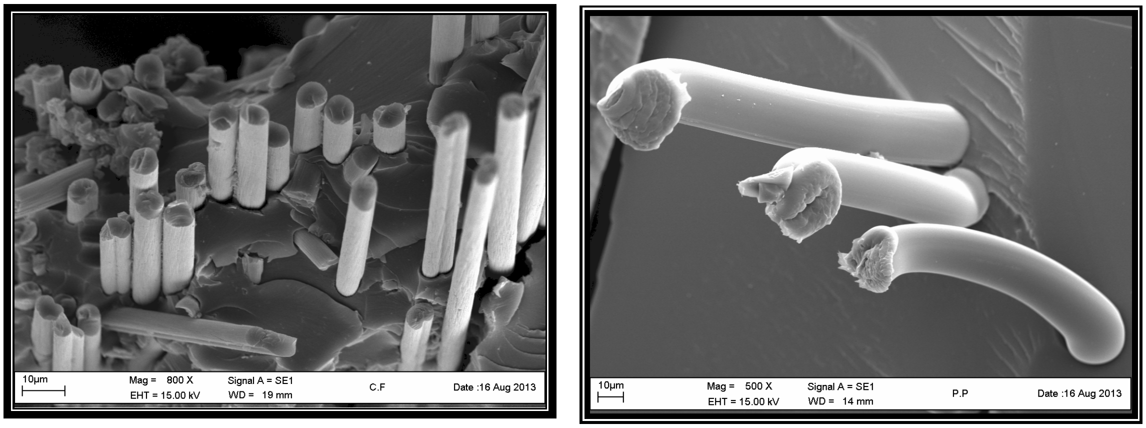

(a) (EP/PVC)+C.F (b) (EP/PVC)+PP.F

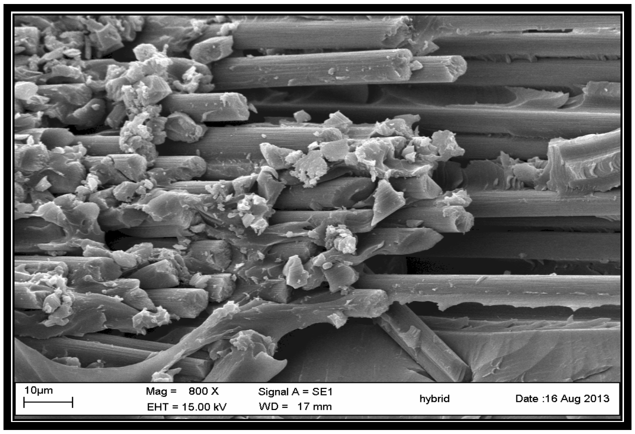

(c) (EP/PVC)+H.F

FIG. 7. SEM micrographs of fracture surfaces for (EP/PVC, (80/20)%) composites.

Hardness and Young's Modulus Properties

It is well known that the hardness is usually defined as the resistance of material to penetration. Hardness is primarily a function of the elastic limit; (i.e. yield strength) of the material [17].

In Fig.(8), the curve shows the dependence of Shore D hardness Number on the content of PVC. This curve can be divided this curve into three regions corresponding to the behaviour of the material. The first is the low additive content region where the hardness follows a gradual decrease with increasing the content of PVC. The blend exhibited a low ductility in this region, so it was named the brittle region. The second was the brittle - ductile transition when the additive content increased from (5 to 15)% of PVC, where the hardness was greatly influenced by the content of the additive. When the content exceeded 15%, the blend exhibited higher toughness and the influence of additive on the hardness became less, this was the ductile region which represents the third region of the curve.

Fig. (9) shows convergent values of hardness for (C.F.) and (H.F.) composites and both are higher than that for (P.P.F.) composite, which is attributed to the brittleness for carbon fibers.

Young's modulus (E) is indicative of the property called stiffness [17], Fig. (10) illustrates the relationship between (E) and PVC content of the blend. The first values of curves reflect stiffness and rigidity, while the small amounts of (E) indicate flexible material.

Fig. (11) shows values of the Young's modulus of (EP/PVC) composites. It can be concluded that (C.F.) composite has the highest value of (E) compared with (P.P.F) and (H.F.) composites; where (E) ranged (2.2-2.7) GPa for carbon fibers and (1- 1.4) GPa for polypropylene fibers[12].

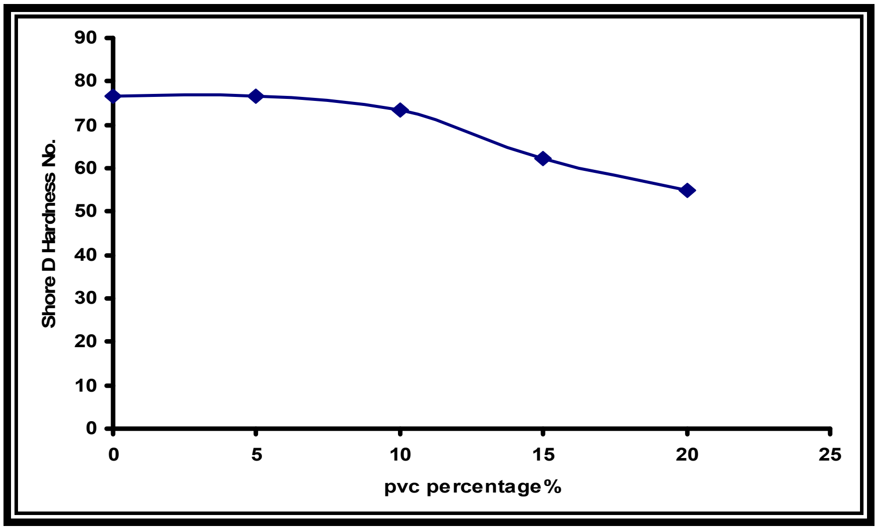

FIG. 8. Shore D hardness No. of (EP/PVC) blends.

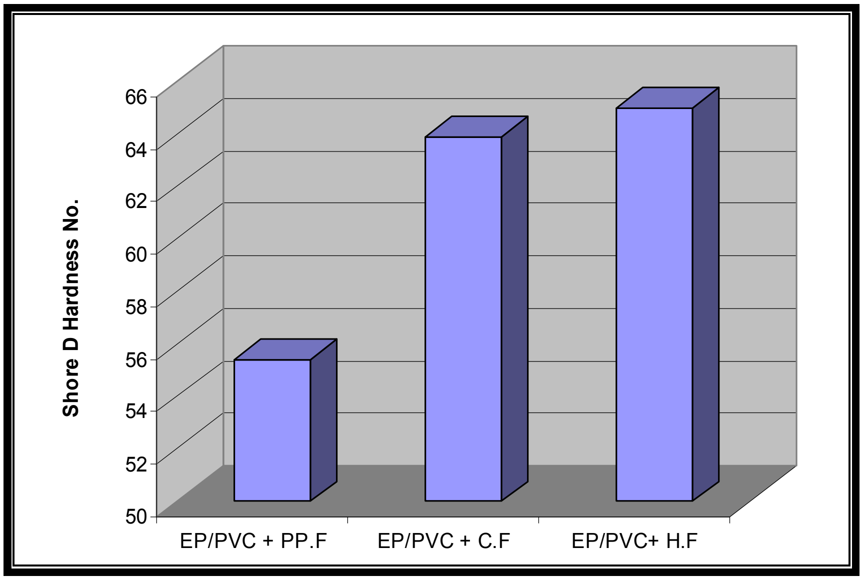

FIG. 9. Shore D hardness No. of (EP/PVC) composites.

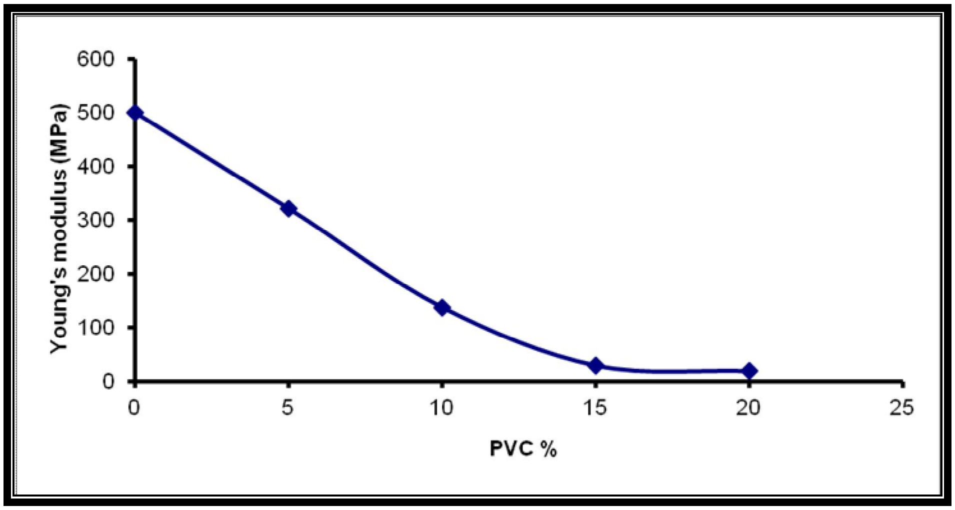

FIG. 10. Young's modulus values of (EP/PVC) blends.

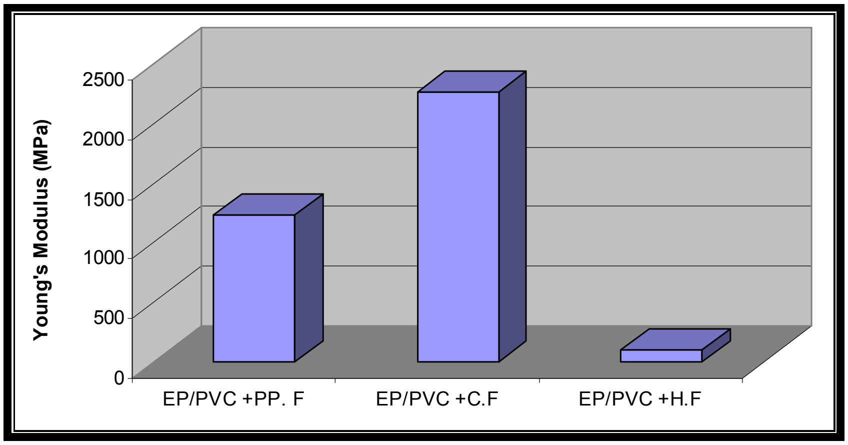

FIG. 11. Young's modulus values of (EP/PVC) composites.

Conclusions

Both epoxy resin and PVC form a single-phase system at the ratio 5% of (PVC), but two phases and heterogeneous blend with good compatibility results at 20% of (PVC). It was observed that impact strength increased at 20 wt.% PVC content in comparison with pure epoxy. The impact strength showed a 13.3% increase at this ratio. From (SEM) micrographs, it can be noticed that the blends exhibit different impact fracture modes depending on the content of the second phase (PVC). SEM provided further evidence, showing that (PVC) indeed acts as a plasticizer factor for epoxy at 20% of (PVC) content. Young's modulus and hardness of epoxy decrease after blending it with PVC, whereas the (EP/PVC) blend has higher (E) and hardness after reinforcing it with carbon fibers.

References

[1] Wang, D., Li, Y., Xie, X. and Guo, B., Polymer, 52(1) (2011) 191.

[2] Zhong, Z., Zheng, S.,Yang, K. and Que, Q., J. of Applied Polymer Science, 69(5) (1998) 995.

[3] Budinski, K.G., "Engineering materials, properties and slection", 9th edition, (Pearson, Upper Saddle River, New Jersey, 2010).

[4] Utracki, L.A., "Polymer alloys and blends, thermodynamics and reology", (Hanser publishers, New York, 1989).

[5] Seymour, C., "Polymer Chemistry", 7th Edition, Charles E. Carraher, Jr., (CRC press, New York, 2006).

[6] Jang-Kyo, K. and Yiu-Wing, M., "Engineered Interfaces in Fiber Reinforced Composites ", (Elsevier, Amsterdam, 1998).

[7] Autar, K.K., "Mechanics of Composite Materials", 2nd edition, (Taylor and Francis Group, 2006).

[8] Martinez, J.M., Eguiazabal, J.I. and Nazabal, J., J. of Applied Polymer Science, 45(7) (1992) 1135.

[9] Feldman, D., Blaga, A. and Coriatry, E., J. of Applied Polymer Science, 29(2) (1984) 515.

[10] Cao, Y., Shao, Y., Sun, J. and Lin, S., J. of Applied Polymer Science, 90(12) (2003) 3384.

[11] Shokrieh, M.M., Saeedi, A. and Chitsazzadeh, M., Journal of Nanostructure in Chemistry, 3 (2013) 20.

[12] Hull, D. and Clyne, T.W., "An Introduction to Composite Materials", 2nd edition, (Cambridge University Press, Great Britain, 1996).

[13] Crawford, R.J., "Plastic Engineering", 3ed edition, (Elsevier Butterworth-Heinemann, Oxford, 1998).

[14] Chang, W.Y. and Lo, M.S., J. of Applied Polymer Science, 36 (1988) 1685.

[15] Saleh, A.B., Mohd Ishak, Z.A., Hashim, A.S. and Kamil, W.A., Journal of Physical Science, 20(1) (2009) 1.

[16] Barone, L., Cicala, G. and Recca, A., Polymer Engineering and Science, 46(11) (2006) 1576.

[17] Rajput, R.K., "Engineering Materials", revised edition, S. Chand, (New Delhi, 2008).

Volume 7, Number 1, 2014. pp. 23-34

Jordan Journal of Physics

ARTICLE

Magnetic Properties of Co^{II}, Co^{III} and $Co^{II–III}$ Coordinated to a Carbosilazane-Based Polymer

Y. A. Hamam[a] , **H. M. El-Ghanem**[b] , **I. M. Arafa**[c] , **Kh. A. Ziq**[d] and **M. R. Said**[a+]

[a] *Physics Department, Yarmouk University, 211-63 Irbid, Jordan.*

[b] *Department of Physics, Faculty of Science and Arts, Jordan University of Science and Technology, PO Box 3030, Irbid 22110, Jordan.*

[c] *Department of Chemical Sciences, Faculty of Science and Arts, Jordan University of Science and Technology, PO Box 3030, Irbid 22110, Jordan.*

[d] *Department of Physics, King Fahd University of Petroleum and Minerals, Dhahran 31261, Saudi Arabia.*

[+] *On leave at: Physics Department, King Faisal University, P.O. Box 400, Al- Ahsa 31982, Saudi Arabia.*

Received on: 19/11/2013;   Accepted on: 25/2/2014

Abstract: Magnetization measurements have been performed on Co^{II}, Co^{III} and $Co^{II–III}$ incorporated into carbosilazane-based polymeric matrix (PEDCSZ, $–[(CH_3)_2SiNHCH_2CH_2NH]_n$--). The local field effect has been evaluated using simple approach similar to the Weiss molecular field model in the paramagnetic state. In this approach, the exchange interaction is represented by the average molecular field constant γ. The calculated γ values are 327, 100 and 223 Oe-g/emu and the corresponding average molecular fields are: 2.7, 0.70 and 2.0 kOe for Co^{II}, Co^{III} and $Co^{II–III}$, respectively. The corresponding molecular field values are about four orders of magnitude lower than that in elemental Co metal. The magnetic measurements support the notion that coordination of this polycarbosilazane matrix with different valences of Co ions has pronounced effects on the exchange interaction and on the general magnetic properties of the system. The results also indicate that the strongest exchange effects are in the Co^{II} case, and that the magnetic properties in the mixed valance Co^{II-III} case do not follow the simple "Additive Rule".

Keywords: Magnetization; Polycarbosilazane; Molecular Field; Paramagnetism; Antiferimagnetism; Exchange Interaction; Coordination and Magnetic Moments.

Introduction

The magnetic behavior of molecular, macromolecular, polymeric and extended lattice systems containing unique magnetic centers attracts the interest of researchers working in a wide variety of disciplines including biomedical diagnosis and treatment, biotechnology, catalysis, magnetic recording, microwave antennas among others [1-5]. Recent advances in plastic antennas rely on using common transition metals such as cobalt, nickel and iron as alternatives to rare-earth based magnetic materials [5]. On the other hand, the presence of isotropic and anisotropic interactions leading to different levels of magnetic coupling or magnetic ordering is of prime importance in magnetic clusters, low-dimensional, 3-dimensional and core-shell molecular magnetic systems [6-8]. Unlike physical dispersion of nano-scale magnetic particles in a polymeric matrix, chemical coordination of magnetic ions to polymer backbone results in a regular

---

Corresponding Author: Y. A. Hamam   **Email**: yaqoob@yu.edu.jo; yaqobhamam@yahoo.com

distribution of magnetic sites at the molecular levels. In such a case, the presence of isolated magnetic spin sites allows one to examine in details spin-spin interaction, spin delocalization, spin-crossover, spintronics and spin-frustrated assemblies. Such interaction is critical in evaluating the performance of soft-hard magnetic materials. Furthermore, combination of magnetic and optical properties to generate switchable photo-magnetic materials is finding increasing interest in spintronics applications. The fundamental magnetic properties of elemental Co^{0}, Co^{II} and Co^{III} and their magnetic interactions in molecular magnets, magnetic polymers and alloys have been extensively studied in recent years [6-8]. Generally, cobalt is added to Fe to increase the saturation magnetism in antennas-based cobalt ferrites [8].

This article is part of our continuing interest in low-dimensional magnetic arrays, where the magnetic sites are attached at regular intervals in fixed position [9-10]. In a previous publication, we examined the dielectric behavior of the divalent (d^{7}) Co^{II}, trivalent (d^{6}) Co^{III} and mixed-valence (d^{7}-d^{6}) Co$^{II\text{-}III}$ containing polycarbosilazane polymer (PEDCSZ, $-[(CH_3)_2SiNHCH_2CH_2NH]_n$--), Fig. 1, and found out that the divalent Co^{II} system exhibited the higher bulk resistance compared to the trivalent Co^{III} and mixed-valent Co$^{II\text{-}III}$ analogs [11], reflecting high localization of electrons. In this work, we extend our interest to examine the spin delocalization / spin interaction of this system. In particular, we present results which support the notion that coordination of these cobalt ions with PEDCSZ greatly affect the spin-spin exchange interaction and therefore their magnetic characteristics. In this respect, we found that the strongest exchange effect occurs in the Co^{II} system, and that the magnetic properties in the mixed-valance Co$^{II\text{-}III}$ system do not follow the simple "Additive Rule".

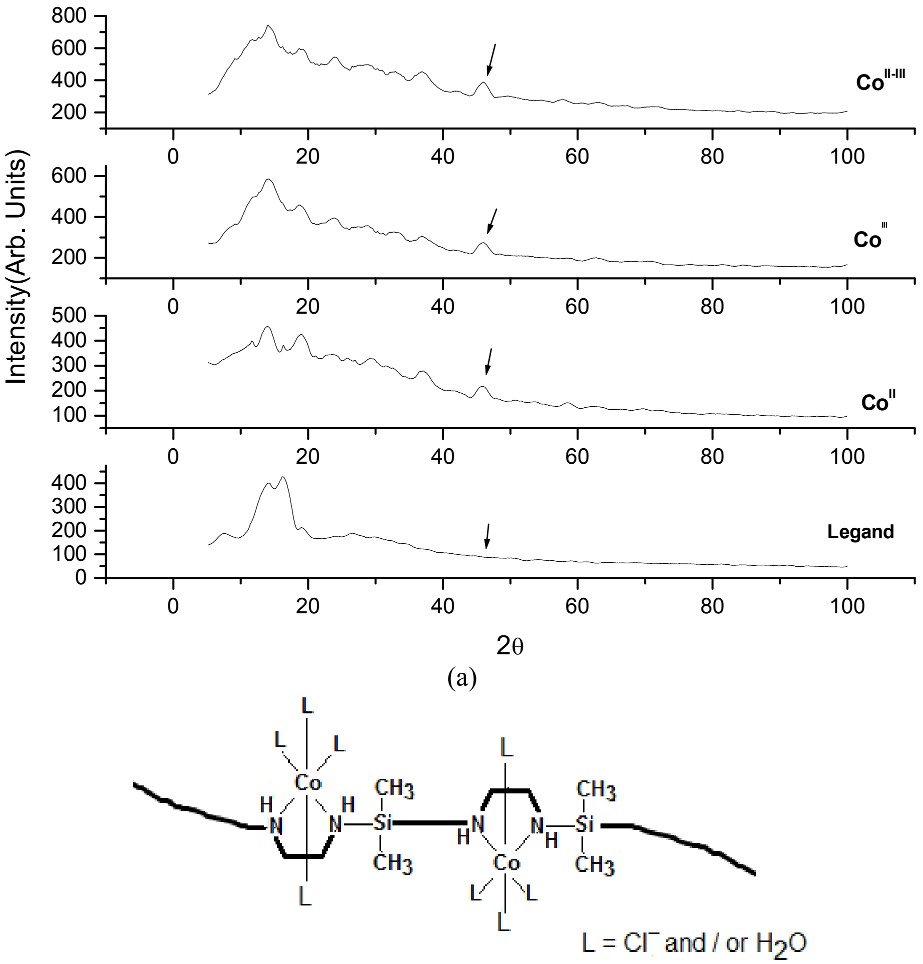

(a)

(b)

FIG. 1(a). XRD pattern for PEDCSZ legand and Cobalt ions-coordinated polymers. (b) Schematic representation of Co^{II}, Co^{III} and Co$^{II\text{-}III}$ chloride salts incorporated into the PEDCSZ matrix.

Experimental Section

The detailed procedure for the synthesis and sample preparations of the examined Co^{II}, Co^{III} and Co^{II-III} containing PEDCSZ has been published earlier [11]. For the magnetic measurements, several milligrams of the powdered materials were encapsulated in small non-magnetic plastic vile. The magnetic moment of the empty vile falls within the noise signal (10^{-5} emu) of the VSM used to monitor the magnetic moment. The magnetization measurements (*M vs. H* and *M vs. T)* were recorded using PAR-4500/150A 9-tesla vibrating sample magnetometer (VSM) in the temperature range 2 to 300 K. A calibrated carbon glass resistor located near the specimen was used to monitor the temperature. A pure Ni-standard was used to calibrate the magnetometer. The overall accuracy in the temperature measurements is better than 0.1K.

Results and Discussions

(a) XRD Results

Fig. 1(a) shows the XRD patterns for the PEDCSZ along with the Co^{II}, Co^{III} and Co^{II-III} coordinated polymers. The patterns were recorded at room temperature using Cu K_α radiation (λ=1.5418 Å), in the 2θ range 5° to 100° with a step size of 0.03° operating at 30 kV and 30 mA. The XRD pattern of PEDCSZ displays two diffuse broad diffraction peaks centered in the 10°-20° and 20°-40° regions, suggesting that PEDCSZ is amorphous in nature. However, the XRD patterns for the cobalt-containing PEDCSZ under investigation show that the degree of crystallinity of the samples increased with the insertion of Co^{II} and Co^{III} ions in the system. Moreover, the diffused peak of the PEDCSZ become more broadened due to the incorporation of Co ions in the polymer backbone. The crystallite size of these samples was estimated using Scherer's Equation ($D_m = K\lambda/[\beta \cos \theta]$, where K is a constant, λ is the wavelength of X-rays, β is the full width at half maximum and θ is the diffraction angle) [12-13]. Based on the widening of the peaks centered at $2\theta = 46^o$, the crystallite size for Co^{II}, Co^{III} and Co^{II-III} containing PEDCSZ is found to be comparable (D ≈10 nm) showing fine particle magnetic systems. Furthermore, the peak at $2\theta = 14.8^o$ is used to estimate the chain separation of the PEDCSZ which gives a d-spacing of 6.00Å (Braggs′ Law, $n\lambda = 2\ d \sin\theta$). The attachment of Co^{II}, Co^{III} and Co^{II-III} increased the chain separation of the PEDCSZ from d = 6.00 Å in metal free matrix to d = 6.32, 6.26 and 6.30 Å, respectively. This slight increase in d-spacing clearly suggests that the cobalt ions are entrapped between the PEDCSZ chains, Fig. 1(b) [9]. The comparable separation distances show that magnetic differences cannot be attributed to spin-spin distance.

(b) Magnetic Results

Fig. 2 shows the variation of magnetization *M* with temperature *T* at a constant applied magnetic field H=10^4 Oe for the three samples Co^{II}, Co^{III} and Co^{II-III} containing PEDCSZ, respectively. *M* exhibits a sharp drop with increasing temperature at low values of T<20K then decreasing very slowly with *T,* suggesting that the three systems undergo a transition from an ordered phase to disordered (paramagnetic) phase. The phase transition occurs at T~17K, as can be clearly shown in the inset of Fig. 2.

The sample doped with Co^{II} reveals the sharpest minimum, which reflects a sharper transition to the paramagnetic state, while the Co^{III} sample showed wider minimum and broader transition to the paramagnetic state. The sample with mixed-valance states Co^{II-III} occurs in between. This would suggest that the sample with Co^{II} ions exhibits a relatively larger magnetic exchange interaction.

Fig. 3 shows the selected isothermal curves of the magnetization, *M*, (in emu/g) *versus* the applied magnetic field, *H*, (in Oe) in the temperature range 4.2K–60K for the three samples of Co^{II}, Co^{III} and Co^{II-III} coordinated PEDCSZ. The curves show no hysteresis or remanence. As it is clear from Fig. 3, the magnetization increases rapidly with *H* at temperatures (T<15 K) and fields (H<10^4 Oe). This is similar to a ferromagnetic behavior that is commonly seen at very low magnetic fields. At higher fields, the magnetization increases linearly indicating the approach to saturation after subtraction of the linear high field susceptibility. At temperatures T≥20K, the magnetization increases linearly with the applied magnetic field, suggesting paramagnetic behavior. The ferromagnetic ordering was tested using the Arrott plots[14], where M^2 *versus H/M* curves are drawn for the three samples and are shown in Fig. 4. These curves, at low values of

H/M, pass through the *H/M* axis as seen in Fig. 4. The nonexistence of intercept with the M^2 axis at small values of *H/M* does not mean that there is no spontaneous magnetization. This is clear from the curvature of the Arrott plots curves at low temperatures. The rapid increase in the magnetization at low temperatures and low fields can be attributed to the formation of fine, as mentioned in the XRD results, superparamagnetic clusters of Co-complexes. This is further supported by the enhanced values of the average molecular field constant γ (the exchange interaction).

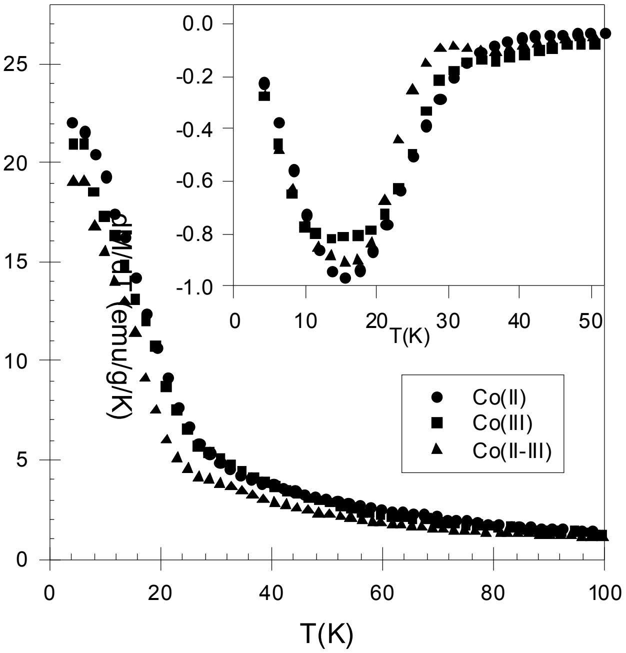

FIG. 2. Variations of the magnetization with temperature. The inset is the derivative of the magnetization with respect to temperature.

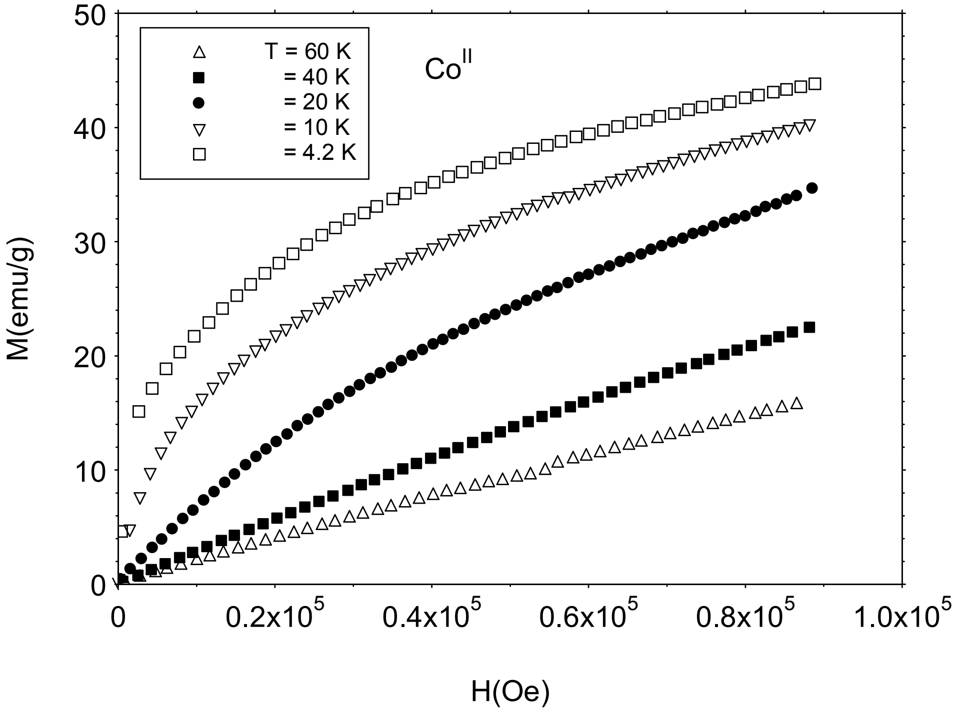

(a)

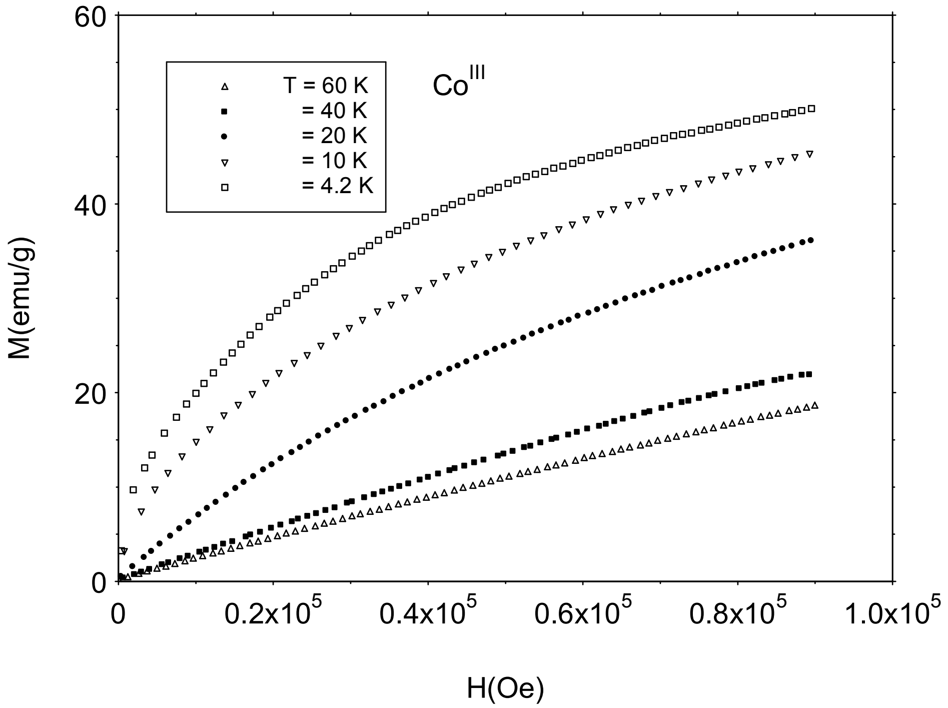

(b)

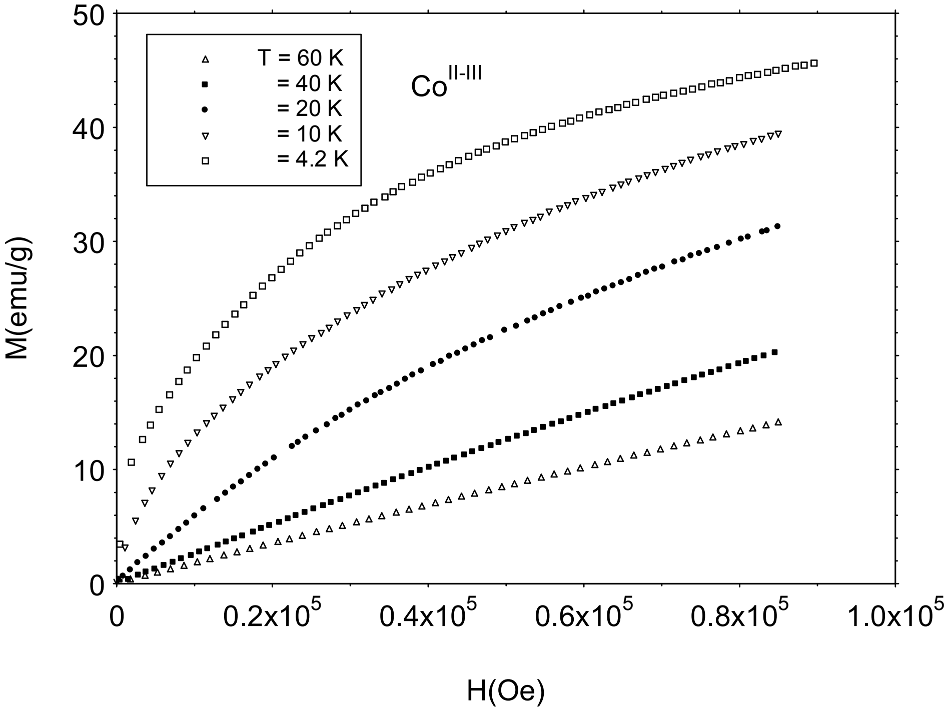

(c)

FIG. 3. Selected isothermal curves of the Co - ions coordinated polymers (a) Co^{II}, (b) Co^{III} and (c) Co^{II-III}.

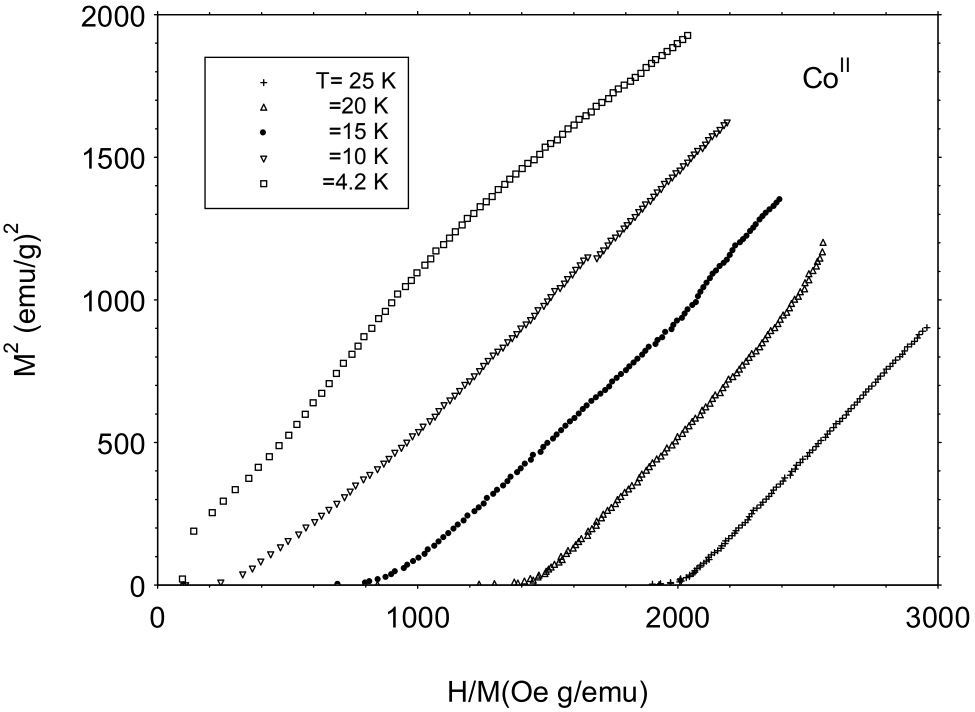
2000
1500
1000
500
0
0
1000
2000
3000
M^2 (emu/g)^2
H/M(Oe g/emu)
Co^{II}
T= 25 K
=20 K
=15 K
=10 K
=4.2 K

(a)

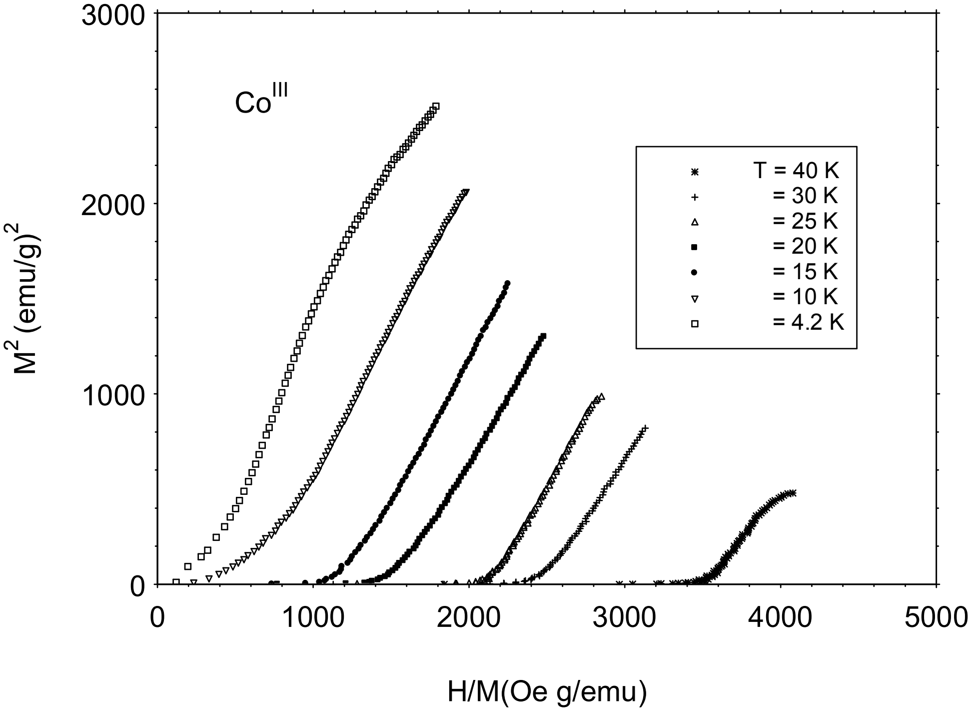
3000
2000
1000
0
0
1000
2000
3000
4000
5000
M^2 (emu/g)^2
H/M(Oe g/emu)
Co^{III}
T = 40 K
= 30 K
= 25 K
= 20 K
= 15 K
= 10 K
= 4.2 K

(b)

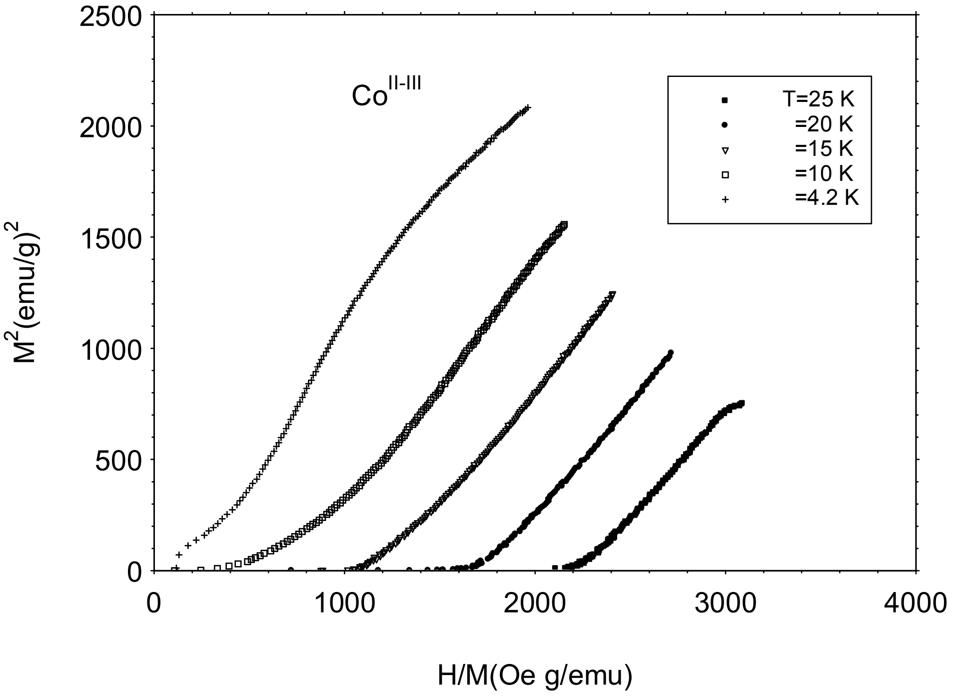

(c)

FIG. 4. Arrott plots of the three Co-ions coordinated polymers (a) Co^{II}, (b) Co^{III} and (c) Co^{II-III}.

The existence of two magnetic phases, superparamagnetic and paramagnetic, can be explained by expressing the total magnetization as [15]:

$$M(T) = M_s(T)L(a) + \chi_h(T)H$$

$$M(T) - \chi_h(T)H = M_s(T)L(a) \qquad (1)$$

where $M_s(T)$ is the saturation magnetization at temperature T, $L(a)$ is the Langevin function given as $L(a)=coth(a)-1/a$, $a=\frac{\mu H}{k_B T}$, μ is the magnetic moment, k_B is the Boltzmann constant and $\chi_h(T)$ is the high field induced susceptibility. $\chi_h(T)$ was calculated using the high field data of the isothermal curves and is presented in Fig. 5 as χ_h *versus T*. Initially, χ_h increases with increasing temperature; reaching maximum near 20K then gradually decreases. The high field induced susceptibility maximum may indicate break-down of the superparamgnetic cluster to a paramagnetic behavior above 20K.

The magnetization curve (Fig. 3; T= 4.2K) for Co^{II} starts with a slope higher than that of Co^{III} and Co^{II-III} coordinated polycarbosilazane. This supports the conclusion that Co^{II} has a higher exchange interaction. The three samples show a Curie-Wiese paramagnetic behavior. The magnetic properties in the mixed valance coordinated polymer Co^{II-III} do not follow the simple “Additive Rule”.

The magnetization curves approach saturation with finite slope at high fields (up to 9 Tesla). Moreover, the Co^{II} magnetization nearly saturates at slightly lower magnetization than that for the other two samples Co^{II-III} and Co^{III}, respectively. In the paramagnetic region, the magnetization curves for all samples increase linearly with the applied field.

Molecular Field

The Weiss molecular field model can be easily applied to paramagnetic materials, where the magnetic spins behave almost independently from each other. The interaction between the spins will affect the local spin environment, giving rise to non-vanishing molecular field (H_m). Isothermal curves fitted to equation 1 do not give satisfactory fit to the experimental data. In order to achieve a reasonable fit, the molecular field effect has to be accounted for in any M *versus* H_{ef}/T representation; where $H_{ef} = H+H_m$, $H_m = \gamma M$ and γ is the exchange interaction constant[16]. In this representation, the applied field, H, is replaced by an effective field, H_{ef}.

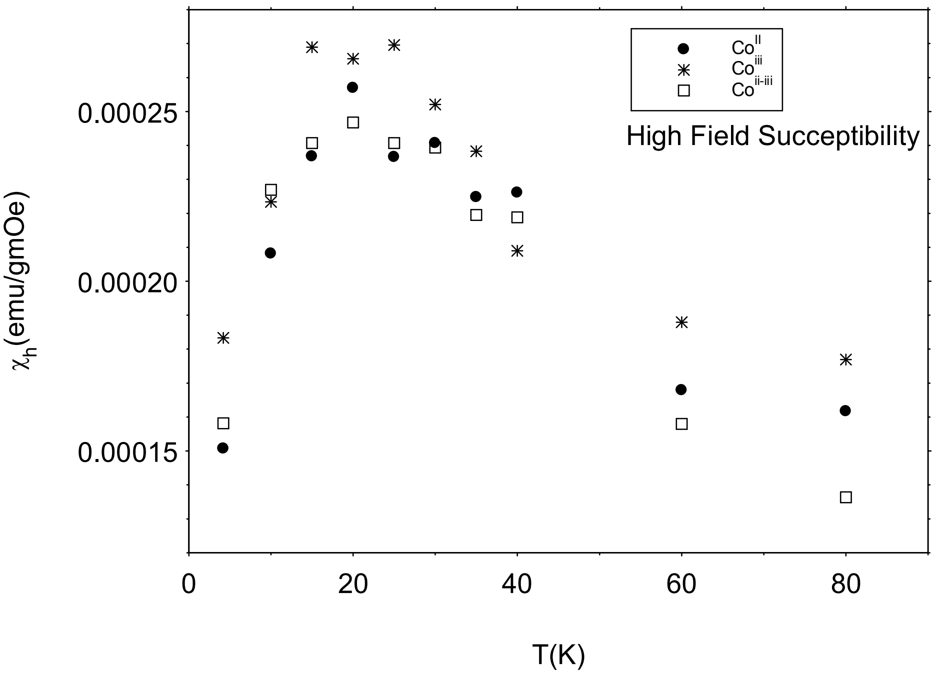

FIG. 5. Variations of the high field susceptibility with temperature.

A simple approach is used to determine γ, and this is explained below. According to the classical theory of paramagnetism, the magnetization, M, can be expressed as a function of H_{ef}/T.

$$M = f\left(\frac{H+\gamma M}{T}\right) \qquad (2)$$

where:

$$\frac{H}{T}+\frac{\gamma M}{T}=f^{-1}(M) \qquad (3)$$

Equation (3) is used to determine different values of γ at constant values of magnetization as shown in Fig. 6. Although the values of γ depend on the temperature as found in other systems [17-18], a constant average value of γ for each sample was used. This can be justified, since the behavior of all samples for T>20K is paramagnetic. The estimated values of γ are 327, 100 and 223 (Oe-g/emu) and the corresponding molecular fields are 2.7, 0.70 and 2.0 kOe for Co^{II}, Co^{III} and $Co^{II\text{-}III}$ samples respectively.

It is worth mentioning that the value of γ for $Co^{II\text{-}III}$ sample is different from the γ values for the other two samples. Incidentally, it equals the difference between the values for the other two samples Co^{II} and Co^{III}. Similarly, the calculated molecular field for $Co^{II\text{-}III}$ is different from the corresponding values for the other two samples; however it equals the difference between the values for the other two samples Co^{II} and Co^{III}. This may reflect an antiferrimagnetic coupling between Co^{II} and Co^{III} atoms in $Co^{II\text{-}III}$ sample. This antiferrimagnetic coupling behavior is due to the coordination of Co^{II} and Co^{III} in the PDECSZ as mentioned in the XRD analysis.

To search for a universal scaling behavior in the magnetization with field and temperature, the magnetization is represented versus H_{ef}/T in Fig.7 for all the isothermal curves for $T \geq 20$K (above the transition temperature). The figure yields a universal behavior for each sample and clearly supports the assumption made in equation 2.

Each of these universal curves for every sample is fitted to a Langevin function, $L(x)=\coth(x)-\frac{1}{x}$, where $x=\frac{\mu_{ef}H_{ef}}{k_B T}$, and μ_{ef} is the average effective magnetic moment. The solid curve in Fig.7 shows this fit for the three coordinated polymers of Co^{II}, Co^{III} and $Co^{II\text{-}III}$, respectively. The average effective magnetic moments for the coordinated polymers, Co^{II}, Co^{III} and $Co^{II\text{-}III}$ determined from the fit are $12.5\mu_B$, $10.3\mu_B$ and $9.66\mu_B$, respectively, where μ_B is the Bohr magneton.

The molecular field values determined are about four orders of magnitude lower than that of cobalt atom, (H_m ~2100 T). However, the elemental Co is ferromagnetic, while the Co-doped samples are paramagnetic.

The effective magnetic moments for the three samples are approximately equal. This is higher than the corresponding magnetic moments of the Co-ions. Since the average magnetic moment of the Co^{II} is a little higher than for the other two samples, this reflects stronger exchange interaction in the Co^{II} coordinated polymer.

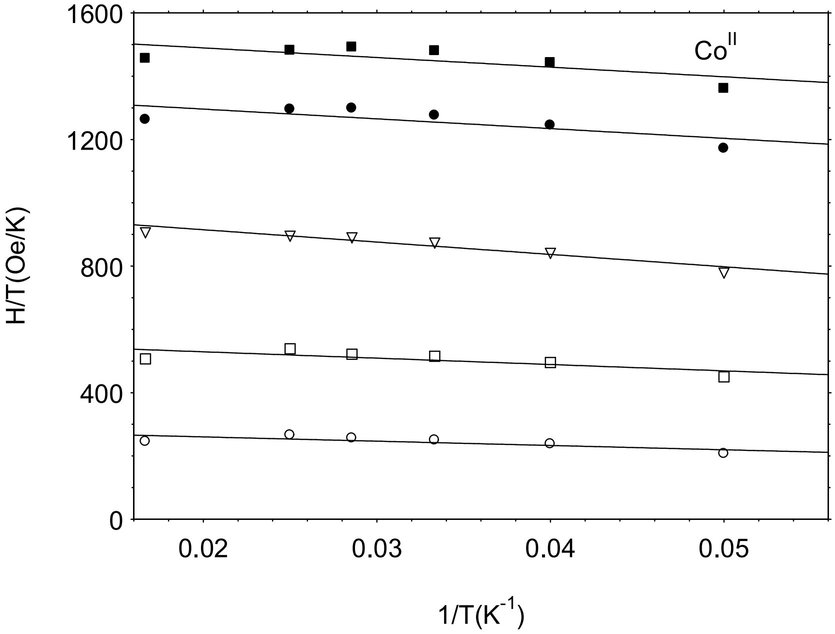

(a)

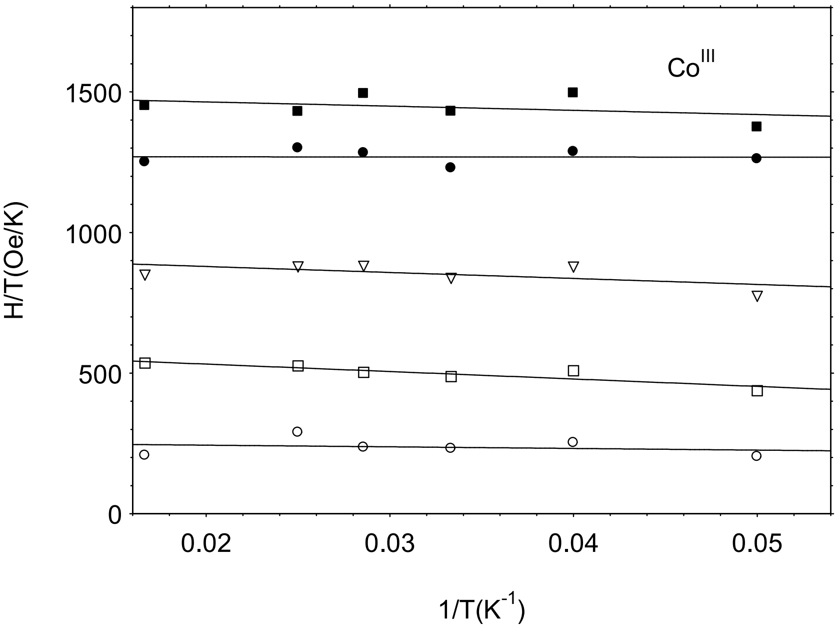

(b)

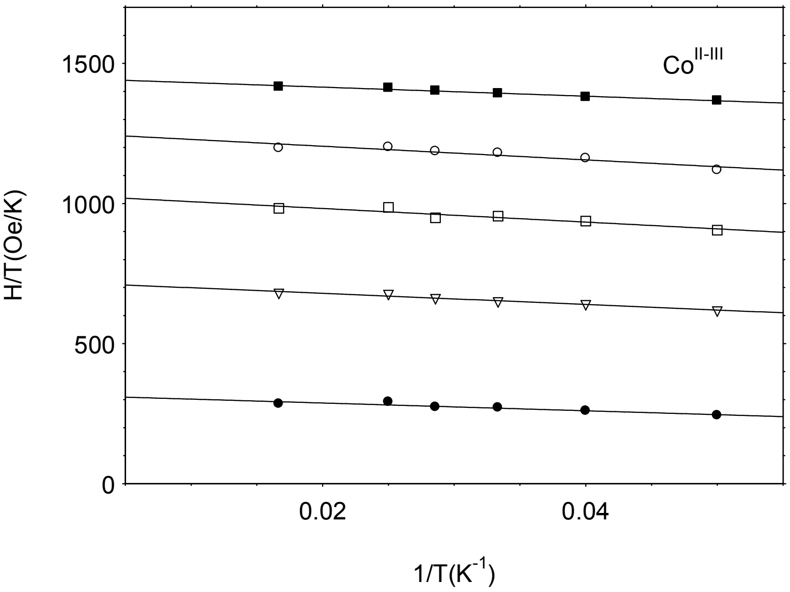

(c)

FIG. 6. Graph of H/T *versus* 1/T for the three samples of the Co-ions coordinated polymers (a) Co^{II}, (b) Co^{III} and (c) Co^{II-III} used to determine the average values of γ and H_m.

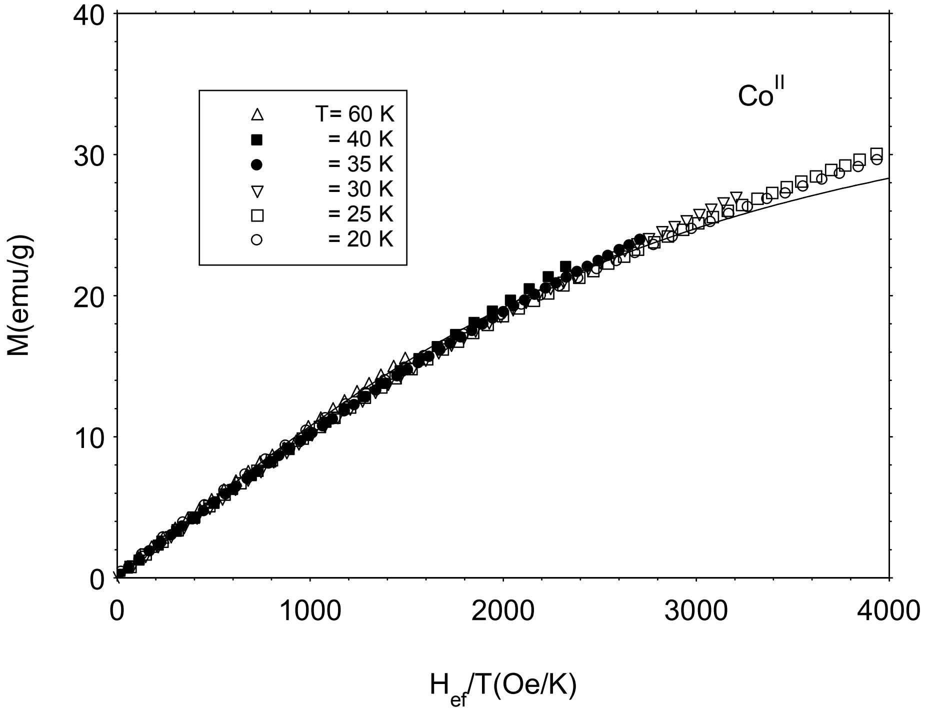

(a)

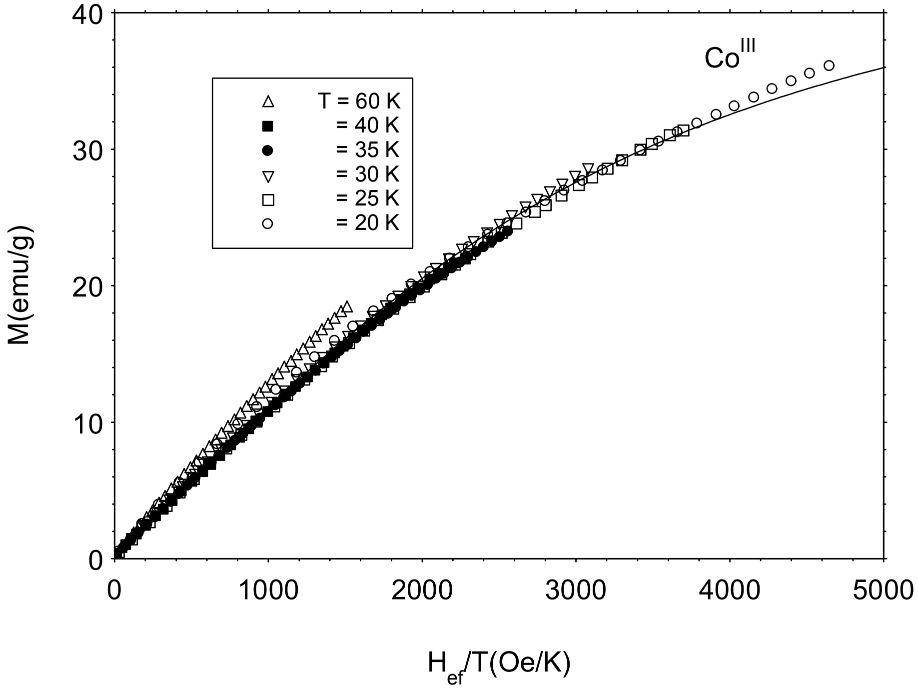

(b)

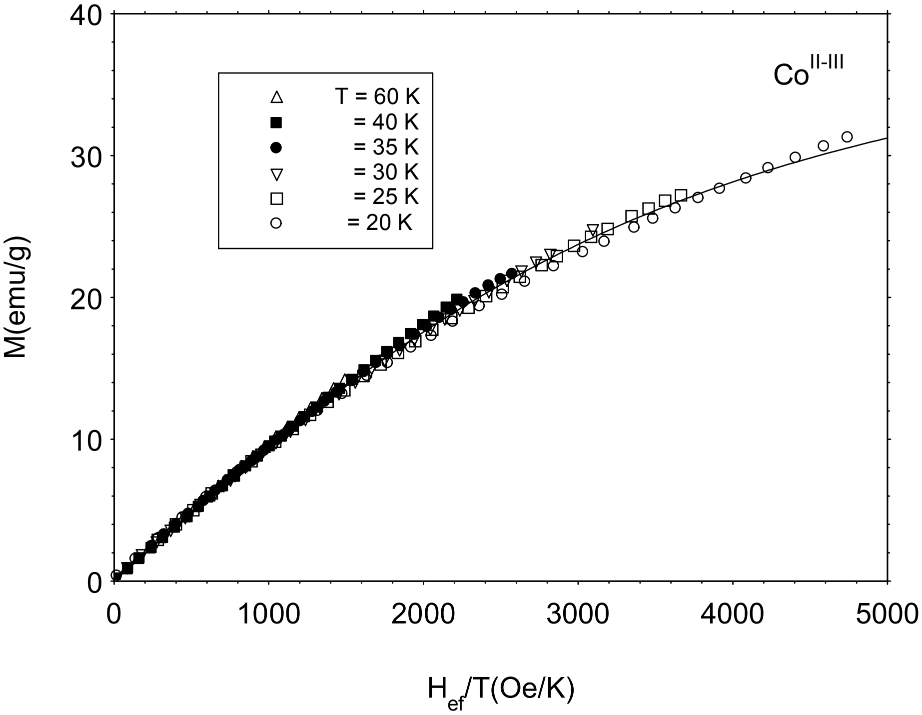

(c)

FIG. 7. Curves of M *versus* H_{ef} /T for $T \geq 20K$, where the solid line is the Langevin fit for the samples of the Co-ions coordinated polymers (a) Co^{II}, (b) Co^{III} and (c) Co^{II-III}.

Conclusions

From the above discussion, it can be concluded that Co^{II} coordinated polymer has a higher exchange interaction than the other two; namely Co^{III} and $Co^{II\text{-}III}$. It has been also found that the exchange interaction constant of the mixed valence polymer $Co^{II\text{-}III}$ is nearly the difference between the values of the exchange interaction constants of Co^{II} and Co^{III}. Meanwhile, the molecular field of the mixed valence polymer is the sum of the corresponding values of the other two samples. This reflects the antifferimagnetic coupling of Co^{II} and Co^{III} in the $Co^{II\text{-}III}$ sample. The mixed valence sample does not follow the simple additive rule.

References

[1] Lartigue, L., Innocenti, C., Kalaivani, T., Awwad, A., del Mar, M., Duque, S., Guari, Y., Larionova, J., Guérin, C., Montero, J.L.G., Montero, V.B., Arosio, P., Lascialfari, A., Gatteschi, D. and Sangregorio, C., J. Am. Chem. Soc., 133(27) (2011) 10459-10472.

[2] Pejaković, D.A., Manson, J.L., Miller, J.S. and Epstein, A.J., Phys. Rev. Lett., 85(9) (2000) 1994.

[3] Gasper, A.B., Ksenofontov, V., Seredyuk, M., Gutlich, P., Coord, Chem. Rev., 249 (2005) 2661-2676.

[4] Lu, A.H., Salabas, E.L. and Schüth, F., Angew. Chem. Int. Ed., 46 (2007) 1222–1244.

[5] Zhai, Y., Wu, W., Zhang, Y. and Ren, W., Composites Sci. Tech., 72(6) (2012) 696.

[6] Hu, L., de Montferrand, C., Lalatonne, Y., Motte, L. and Brioude, A., J. Phys. Chem. C, 116(7) (2012) 4349-4355.

[7] Lagarkov, A.N. and Rozanov, K.N., J. Magnet. Magnet. Mater., 321(14) (2009) 2082-2092.

[8] Maaz, K., Mumtaz, A., Hasanain, S.K. and Ceylan, A., J. Magnet. Magnet. Mater., 308(2) (2007) 289-295.

[9] Hamam, Y., El-Ghanem, H.M., Arafa, I.M., Said, M.R. and Abo-Aljarayesh, I., Polym. Int., 56 (2007) 376.

[10] Arafa, I., El-Ghanem, H. and Nemrat, S., In: A.V. Hopper (Ed.), Recent Developments in Polymer Research, (Nova Science Publishers Inc., New York, 2007), p 1.

[11] Elghanem, H.M., Abdul Jawad, S., Aljundi, J., Afaneh, F. and Arafa, I., Polym. Int., 52 (2003) 1125.

[12] Pawar, S.G., Patil, S.L., Chougule, M.A., Achary, S.N. and Patil, V.B., International Journal of Polymeric Materials, 60 (2011) 244.

[13] Utkan, G. *et al.*, Journal of Colloid and Interface Science, 353 (2010) 372.

[14] Boott, J.G., In: E. P. Wolhlfath and K.J. Buschow (Eds.), Ferromagnetic Materials, Vol. 4, (North-Holland, New-York, 1988), p. 211.

[15] Said, M.R., Hamam, Y.A., Mahmmood, S.H. and Abu-Aljarayesh, I., Mu′tah Lil-Buhooth WaAlderasat, 15(1) (2000) 93.

[16] Cullity, B.D., "Introduction to Magnetic Materials", (Addison-Wesley, New-York, 1972).

[17] Brun, T.O., Kouvel, J.S. and Lander, G.H., Phys. Rev. B, 13 (1976) 5007.

[18] Kouvel, J.S. and Brun, T.O., Phys. Rev. B, 22 (1980) 2428.

Volume 7, Number 1, 2014. pp. 35-42

Jordan Journal of Physics

ARTICLE

Effects of Ultrasound in Etching and Detecting Parameters of CR-39 Detector

Saeed H. Saeed Al-Nia'emi

Department of Physics, College of Education for Pure Sciences, University of Mosul, Iraq.

Received on: 3/4/2012 Accepted on: 18/3/2014

Abstract: Effect of 40 kHz ultrasound (US) in chemical etching of alpha-particle tracks in CR-39 solid state nuclear track detector were investigated. Alpha-particle irradiations (using 1 μCi ^{241}Am source) were made with different energies under normal incidence. All track etch rates V_D, V_B, V_T and V increased, but the critical angle of the detector θ_C decreased. The maximum increase in the bulk etch rate V_B, the track's diameter growing rate V_D, the etch rate ratio V, the etching efficiency η and sensitivity S were about 12% , 20%, 25%, 12.5% and 27.2%, respectively, while the decrease in the critical angle was about 15.2%. These results were in agreement with those found by [1, 2]. A minimum detection threshold energy of alpha-particle ~0.2 MeV was recorded.

Keywords: CR-39; Ultrasound; Track Etch; Alpha Particle.

Introduction

The environmental factors play an important role in estimating the real effects of charged particles in solid state nuclear track detectors (SSNTDs). SSNTDs, especially plastic ones, can be subjected to one or more factors which may produce physical or chemical changes in the registration and detection properties of the detector [3,4,5]. The environmental conditions improve the etching and detecting parameters of the detectors, such as the bulk etch rate V_B, the track etch rate V_T , the etching rate ratio (the sensitivity) V, as well as the angular and energy responses. The produced enhancement increases the ability of the detectors to detect particles having low energies [6].

Ultrasound (US) is considered one of the factors which affect the properties of the solid state nuclear detectors [1]. The vibration produced by the ultrasound source may excite the molecules of the detector material and the free radicals formed in the damaged regions through particle irradiations. The excitation induced by ultrasound increases the latent energy of the damaged regions produced by the incident particles which get more degradation through etching than the damaged regions etched without ultrasound. Therefore, any increase in degradation of the damaged regions leads to increase the track etch rate which subsequently leads to increase the track's diameter and size.

The effects of different factors on the parameters of solid state nuclear track detectors have been investigated. The effects of high doses of electromagnetic radiations such as: Gamma rays , X-rays , Laser and UV lights [4, 7-12], Ultrasonic waves [1,2,13], electric field [6] and annealing temperature [14] have been studied. Other conditions were also taken into consideration; the concentration and temperature of the etching solution [15], the

Corresponding Author: Saeed H. Saeed Al-Nia'emi **Email**: saeed_alnaeme@yahoo.com

chemical additives to the etching solution [16], effects of stirring [17, 18] as well as the presence of oxygen and the humidity during particle irradiation of the detector [19].

All these factors showed significant effects on the characteristics of solid state nuclear track detectors such as: the track's diameter and size, the track depth, the energy response, the bulk etch rate V_B, the track etch rate V_T and the etch rate ratio or detector sensitivity V, in CR-39, LR-115, cellulose nitrate and PM-355 detectors.

In the present work, the possible effects of ultrasound energy in the chemical etching of particle tracks in plastic solid state nuclear track detectors CR-39 were investigated.

Methodology

CR-39 detectors of 550 µm thickness were used from Page Mouldings (Worcestershire, England). Two sets of alpha-particle irradiated detectors were prepared: (1) only chemically etched (2) chemically etched under ultrasound impact for different etching durations.

Alpha-particle irradiations (using 1 µCi ^{241}Am source, main emitted alpha energy = 5.495 MeV) were made with energies of 0.2, 0.5, 1, 1.5, 2.5, 3.5, 4.5, 5.49 MeV under normal incidence. The alpha-particle energies were varied by changing the source to detector distance in air under atmospheric pressure. Ultrasound–induced chemical etching of alpha-particle irradiated detectors was performed using an ultrasonic bath (ULTRASONIC CLEANER MODEL FXP 20, Australia) at 40 kHz. Both sets of detectors were etched in a 6.25N aqueous solution of KOH at 70±1^{O}C. The gravitational method [3, 4, 20] was used to measure the bulk etch rate V_B. The track openings diameters were measured under an optical microscope with a magnification of 40× attached to digital camera [MDCE-5A] connected to a computer.

The following equations [3] have been used to estimate the etch rate ratio V, also called sensitivity of the etchable track detector due to normal incidence of charged particles. The track etch rate V_B is measured by the change in the weight of the detector using the relation:

$$V_B = \frac{1}{2\rho A}\frac{\Delta m}{\Delta t} \tag{1}$$

where $A (cm^2)$ and ρ (gm/cm^3) are the area of the detector surface and the density of the detector material respectively, while the quantity $(\frac{\Delta m}{\Delta t})$ is the amount of the bulk material removed from the surface of the detector sheet during etching. The weight of the detectors was measured before and after etching for 2 hours in both ultrasound-induced chemical etching (CE+US) and conventional chemical etching (CCE) detectors.

The surface diameter of the track D is given by:

$$D = 2V_B t\sqrt{\frac{V_T - V_B}{V_T + V_B}} \tag{2}$$

$$\frac{D}{t} = \mathrm{V_D} \tag{3}$$

where V_D is the rate of diameter growing of the track. From (2) and (3), one can get that the track etch rate V_T is:

$$V_T = V_B\frac{4V_B^{\ 2} + V_D^{\ 2}}{4V_B^{\ 2} - V_D^{\ 2}} \tag{4}$$

The etch rate ratio or detector sensitivity V, can easily be estimated by using the relation:

$$V = \frac{V_T}{V_B} \tag{5}$$

Further parameters related to the etch rate ratio V such as the critical angle (angular response) θ_C, etching efficiency η and etching sensitivity S can be estimated from the following equations [21]:

$$\theta_\mathrm{C} = \sin^{-1}(\frac{1}{V}) \tag{6}$$

$$\eta = 1 - \frac{1}{V} \tag{7}$$

$$S = V - 1 \tag{8}$$

Results and Discussion

The relation between the track's opening diameter and alpha energies is shown in Figs. 1 and 2 for both sets of detectors of ultrasound-induced chemical etching (CE+US) and conventional chemical etching (CCE) of particle tracks, respectively. One can see in Fig. 1 that the revealing of ultrasound-induced chemical etching tracks was faster than that of conventional chemical etching ones. The diameters were found to increase for ultrasound-induced chemical etching tracks over conventional chemical etching. However, the change in the track's diameter was maximum and ranged between (10-100%) when the energy of alpha particle was about 1.5 MeV. Fig. 3 shows the difference between the tracks' diameters of used alpha-particle energies etched for 2 h in CE+US and CCE methods.

The minimum energy E_{min} of alpha particle that could show etched tracks in CR-39 was ~0.2 MeV in both (CE+US) and CCE methods of etching. This value is called the threshold energy of the detector and the particles having energies less than the threshold energy cannot reveal etched tracks [3, 6].

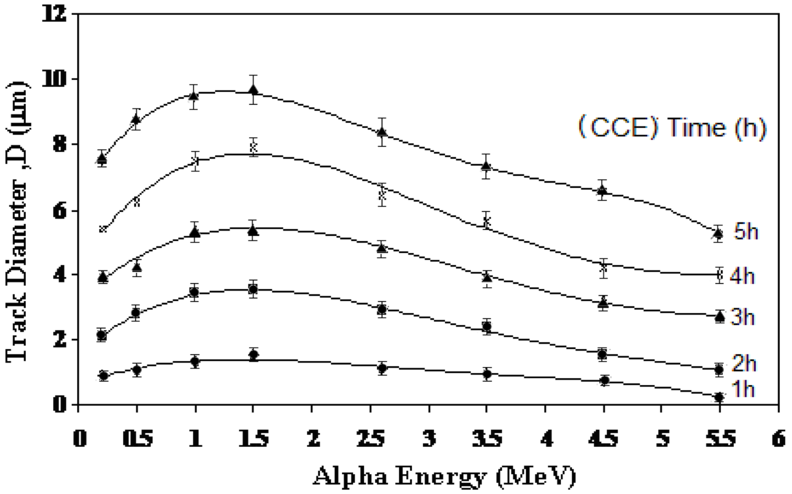

FIG. 1. Track diameter *versus* alpha-particle energy in conventional chemical etching (CCE).

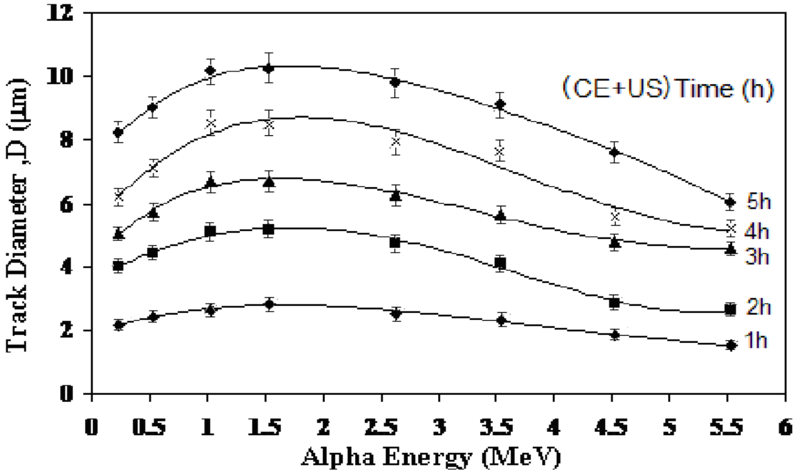

FIG. 2. Track diameter *versus* alpha-particle energy in ultrasound-induced chemical etching (CE+US).

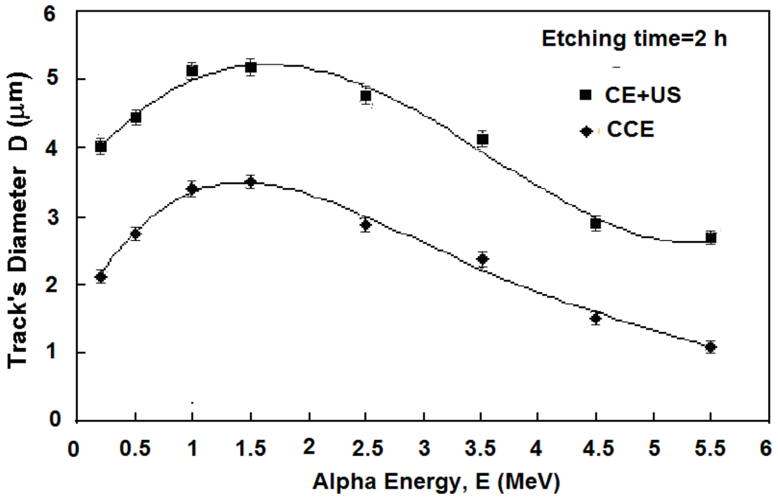

FIG. 3. Track diameter *versus* alpha-particle energy for an etching time of 2h in both (CE+US) and CCE methods.

The increase in tracks' diameters observed in ultrasound-induced etching (CE+US) method is due to the increase in the etching rates of the detector. The vibration energy of the ultrasound increases the reaction energy between etching solution and detector molecules which in turn increases the ability of interacted molecules to overcome the barrier energy separating the interacted and the resultant materials. The exposure of the etching solution to the ultrasound energy accelerated the degradation of the detector molecules which resulted in an enhancement of the tracks growing rate V_D , the bulk etch rate V_B, the track etch rate V_T and the detector sensitivity V at a given etching time. Afifi *et al.* [2] also indicated an increase in diameter and size of the tracks in CR-39 detectors chemically etched under ultrasound of 2 MHz.

On irradiating the etching medium by ultrasound, its temperature is controlled by using a thermocouple to keep the solution temperature constant at (70±1) ^{o}C and to minimize any effects on tracks due to raising the temperature of the etching solution.

The variation of the track growing rate V_D and track etch rate V_T with alpha–particle energy is shown in Figs. 4 and 5. It was found that V_D and V_T increase with alpha-particle energies with a maximum value at ~1.5 MeV.

The exposing of the chemical etching solution to US increased both V_D and V_T up to 20% and 25%, respectively as compared with those of CCE detectors.

The relation between etching rate ratio or sensitivity V and the incident alpha-particle energy for both ultrasound-induced chemical etching (CE+US) and conventional chemical (CCE) etching methods is shown in Fig. 6. One can see that the behavior of V against alpha energy is similar to the behavior of V_T and V_D. The detector sensitivity $V(=V_T/V_B)$ was studied by measuring the bulk etch rate V_B for both ultrasound-induced chemical etching and conventional chemical etching detectors. The bulk etch rate V_B was found equal to 1.74 μm.h^{-1} for ultrasound-induced chemical etching (CE+US) and 1.56 μm.h^{-1} for conventional chemical etching (CCE) detectors. V_B is considered constant up to 7 μm of etched depth in the detector, and any variation in V_T was accompanied by a variation in V according to the relation above.

The (CE+US) etching method showed an enhancement in the detector sensitivity V up to 16% over the CCE etching method for alpha energy of 1.5 MeV. Su [22] found that ultrasound-induced chemical etching of Lexan and LR-115 detectors increased the sensitivity about (20-50)% .

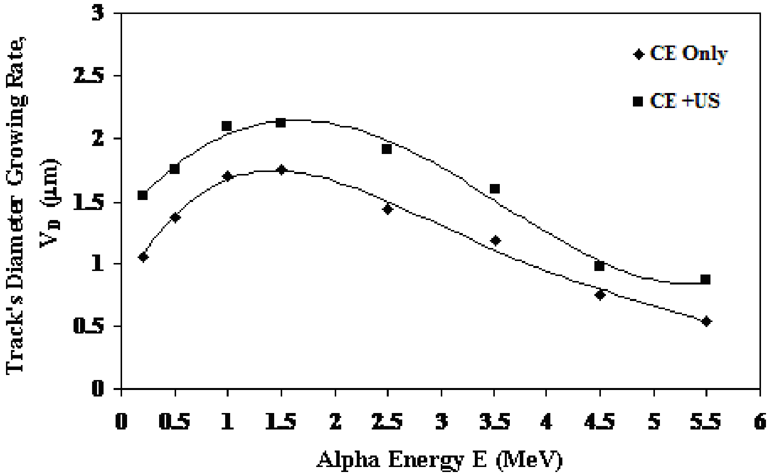

FIG. 4. Track's diameter growing rate *versus* alpha-particle energy for an etching time of 2 h in both (CE+US) and CCE methods.

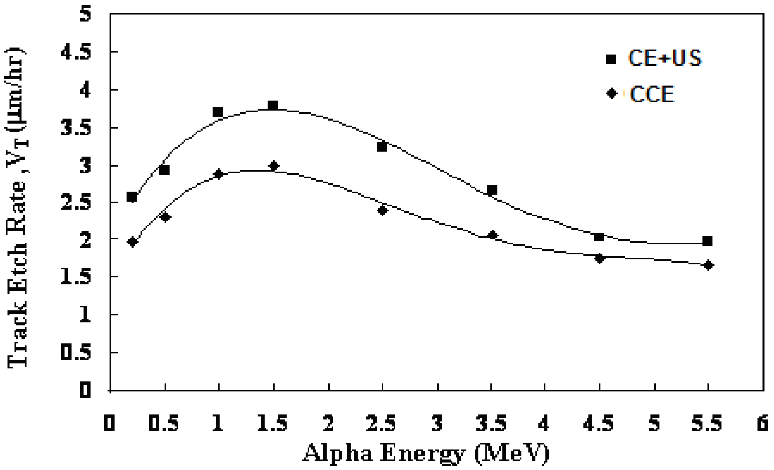

FIG. 5. Track etch rate *versus* alpha-particle energy.

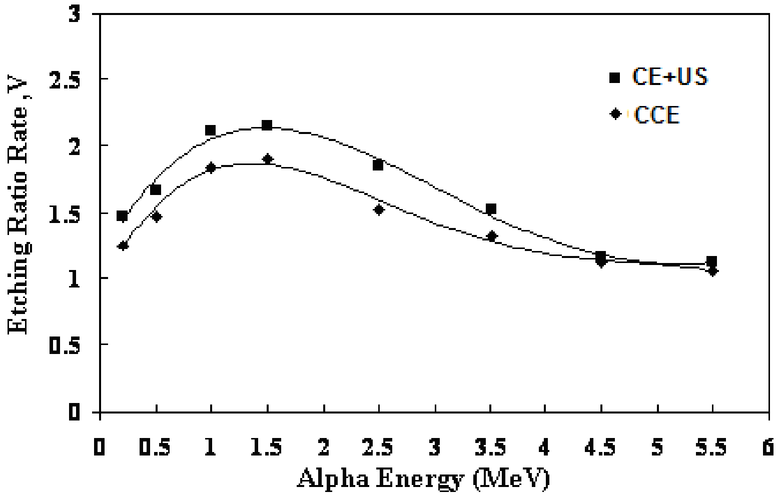

FIG. 6. Etch rate ratio or detector sensitivity *versus* alpha-particle energy.

Etching sensitivity *S* and etching efficiency η as functions of alpha-particle energy are shown in Figs.7 and 8, respectively. The chemical etching under ultrasound impact (CE+US) produced an enhancement in η and *S of* about 12.5% and 27.19%, respectively for alpha-particle irradiation energy of 1.5 MeV as compared to conventional chemical etching (CCE). Pandey *et al.* [1] and Afifi *et al.* [2] also found an enhancement in S, η and θ_c in etching CN-85 and Lexan detectors under ultrasound effect.

The critical angle θ_C, is defined as the minimum incident angle of the particle below which the etched tracks cannot be revealed. The variation of the critical angle as a function of alpha-particle energy is shown in Fig. 9.

CR-39 detectors showed a maximum decrease in the critical angle for alpha-particle at an energy of 1.5 MeV, which means an increase in the angular response of the detector to the incident particles. It is shown from Fig. 9 that the angular response of CR-39 to alpha particle is increased on ultrasound-induced chemical etching over the conventional chemical etching and having a maximum value at alpha energy of 1.5 MeV.

The effect of the ultrasound on the angular response of CR-39 to alpha-particles is obviously seen at an energy of 1.5 MeV through dropping of the critical angle from 31.39^o in conventional chemical etching (CCE) to 27.25^o degree in ultrasound-induced chemical etching (CE+US).

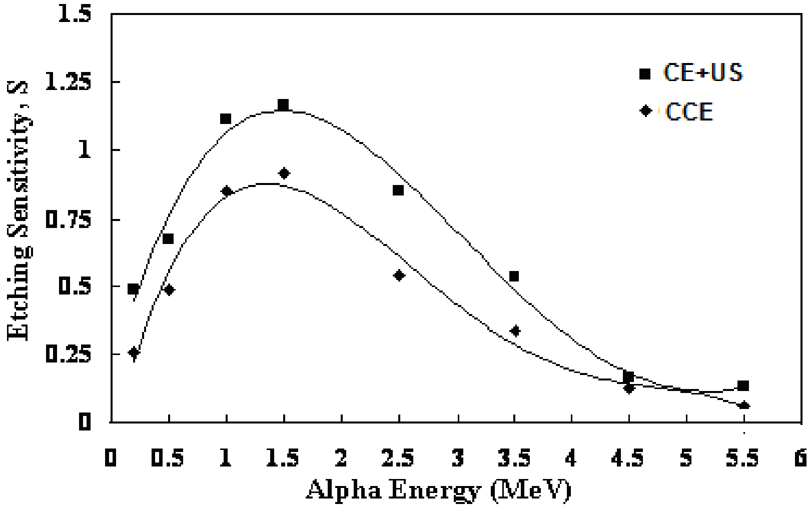

FIG. 7. Etching sensitivity *versus* alpha-particle energy.

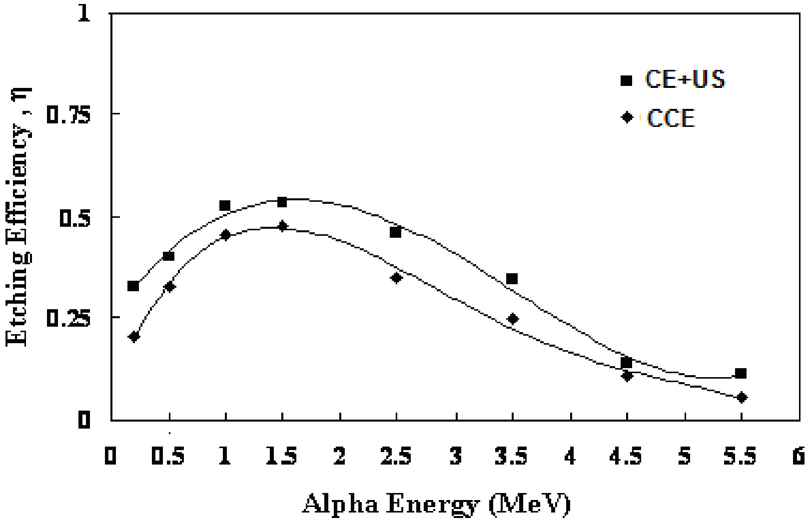

FIG. 8. Etching efficiency *versus* alpha-particle energy.

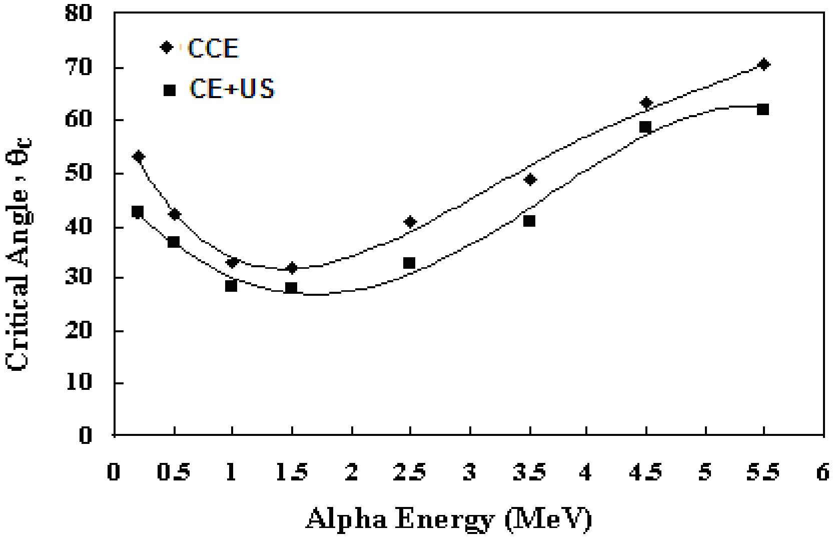

FIG. 9. Critical angle *versus* alpha-particle energy.

Conclusion

The results showed significant changes in revealing the track properties of particle tracks in CR-39 detector in ultrasound-induced etching as compared to conventional chemical etching method. The significant advantages of ultrasound-induced chemical etching over conventional chemical etching of particle tracks are: reduction in etching time, larger track-etch rates V_B, V_T and V, larger etching sensitivity η and efficiency *S*, and lower critical angle θ_C of the detector, leading to an overall improvement in the track revealing process. The decrease in the critical angle in ultrasound-induced etching means an improvement in the angular response of the detector which leads to increase the ability of CR-39 detector to detect particles with lower incident angles as compared to conventional chemical etching detectors.

References

[1] Pandey, A.K., Kalsi, P.C. and Iyer, R.H., Nucl. Instrum. and Meth. in Physics Research B, 134 (1998) 393.

[2] Afifi, H., El-Sersy, A. and Khaled, N., Radiation Effects and Defects in Solids, 159 (2004) 37.

[3] Durrani, S.A. and Bull, R.K., "Solid State Nuclear Track Detection", (Pregamon Press, Oxford, 1987).

[4] Al-Nia'emi, S.H.S., Ph.D. Thesis, College of Science, University of Mousl, Iraq, (1998).

[5] Al-Nia'emi, S.H. and Kasim, Y.Y., Jordan Journal of Physics, 6(1) (2013) 17.

[6] Omer, N.S.Kh., MSc. Thesis, College of Education, University of Mosul, Iraq, (2002).

[7] Khayrat, A.H. and Durrani, S.A., Radiat. Meas., 25 (1995) 163.

[8] Shahid, Sh., Rafique, Sh., Khaleeq-ur-Rahman, M., Ghauri, I.M. and Faizan-ul-Haq., 31st EPS Conference on Plasma Phys. London, 28 June-2 July 2004 ECA , 28G, (2004) p.5.

[9] Jaleh, B., Parvin, P., Mirabaszadeh, K. and Katouzi, M., Radiat. Meas., 38 (2004) 173.

[10] Tse, K.C.C., Ng, F.M.F. and Yu, K.N., Poly. Degradation Stability, 91 (2006) 2380.

[11] Ng, F.M.F. and Yu, K.N., Materials Chemistry and Physics, 100 (2006) 38.

[12] Tse, K.C.C., Nikezic, D. and Yu, K.N., Radiation Measurement, 43 (2008) S98.

[13] Dawood, Y.Z., Al-Hamdani, A.H. and Zayer, M.Q., ARPN Journal of Engineering and Applied Sciences, 8(2) (2013) 1819.

[14] Al-O'bedy, A.A.I., MSc. Thesis, College of Education, University of Mosul, Iraq (2000).

[15] Khalil, M.A., A'bdel, N.S. and Fathi, F.M.A., Rafidain Journal of Science, 16(1) (2005) 69.

[16] Chan, K.F., Ng, F.M.F., Nikezic, D. and Yu, K.N., Nuclear Instruments and Methods in Physics Research Section B: Beam Interactions with Materials and Atoms, 263(1) (2007) 284.

[17] Ho, J.P.Y., Yip, C.W.Y., Nikezic, D. and Yu, K.N., Radiat. Meas., 36 (2003) 141.

[18] Yip, C.W.Y., Ho, J.P.Y., Koo, V.S.Y., Nikezic, D. and Yu, K.N., Radiation Measurement, 37 (2003) 197.

[19] Khan, H.A., Nucl. Instrum. and Meth., 173 (1980) 55.

[20] Mahmood, I.T.H., Ph.D Thesis, Department of Physics, College of Education, University of Mosul, Iraq, (2011).

[21] Fleisher, R.L., Price, P.B. and Walker, R.M.. "Nuclear Track in Solids: Principle and Application", (University of California Press, 1975).

[22] Su, C.S., Radiation Protection Dosimetry, Oxford University Press, 34 (1990) 51.

الاستنتاجات

1. تم الحصول على توافق كبير بين قيم المعدلات الشهرية لِ (ET_O) المحسوبة بواسطة نموذج (PM-1998) ونموذج حوض التبخر (PAN).
2. أظهرت علاقات الارتباط بين القيم الشهرية لِ (ET_O) المحسوبة بواسطة النموذجين وجود ارتباط عالياً جداً في جميع المحطات، حيث تراوح معامل التحديد لهذه العلاقات بين (0.996-0.961).
3. تم الحصول على علاقة ارتباط لعموم العراق بين قيم (ET_O) المحسوبة بواسطة النموذجين أعطت معامل تحديد عالياً بلغ (0.931)، والعلاقة هي:

$$\mathbf{ET_O(PM) = 1.051 * ET_O(PAN) - 0.298}$$

4. نظراً لكون معامل التحديد عالٍ جدا بين نموذجي الفاو بنمان مونتيث وحوض التبخر ولكون نموذج حوض التبخر يعتمد على بيانات ومعلومات سهلة ومتاحة فيمكن أن يكون كبديل امثل لنموذج (PM-1998) في حالة عدم توفر بيانات مناخية كاملة يتطلبها نموذج بنمان مونتيث.

المراجع

[1] Allen, R.G., Smith, M., Perrier, A. and Pereira, L.S., ICID Bulletion, 43(2) (1994) 1.

[2] Allen, R.G., Hill, R.W. and Vemulapali, S., Summer Meeting of ASAE, 942132 (1994).

[3] Howell, T.A., Schneider, J.L. and Avett, S.R., Trans. ASAE, 38(3) (1995) 745.

[4] Jacobs, J.M., “Evaluation of Reference Evapotranspiration Methodologies and AFSIRE Water Use Simulation Model”. (University of Florida, Gainesville, Florida, 2001).

[5] Xu, C.Y. and Singh, V.P., Water Resources Management, 16 (2002) 197.

[6] Othoman, A., Clariza, F., Kenji, J. and Atsush, T., Fukuoka Japan, Memoira of the Faculty of Engineering, University of Kyushu, 66(1) (2006).

[7] Grisme, M.E., Orange, M., Snyder, R. and Matyac, R., Journal of Irrigation and Drainage Engineering, 128(3) (2002) 1803.

[8] Meyer, W.S., Smith, D.J. and Shell, G., “Estimating Reference and Crop Evapotranspiration from Weather Data and Crop Coefficients”, CSIRD Land and Water, Technical Repport 34/98, OCT, (1999).

[9] Lage, M., Bamouh, A., Karrou, M. and El-Mourid, M., Agronomie, 23 (2005) 625, INRA.

[10] Richard, L., Morteza, O., Scott, M. and Mark, E., Journal of Irrigation and Drainage Engineering, 131(3) (2005) 249.

[11] يعقوب، آلاء عبد الله ، مجلة هندسة الرافدين – جامعة الموصل، (2013) 21(1).

الجدول (2): علاقات الارتباط بين المعدلات الشهرية للقيم اليومية للتبخر نتح المرجعي (ET_o) المحسوبة بطريقة (PM- 1998) وطريقة حوض التبخر (PAN) في المحطات كافة.

Corr Station	*ET$_O$*(PM) & *ET$_O$*(PAN)	R^2	M.A.E %	R.M.S.E %
Zakho	*ETo* (PM) = 0.805 * ETo(PAN) + 0.153	0.993	6.0	4.4
Mosul	*ETo* (PM) = 0.810 * *ETo*(PAN) + 0.127	0.996	5.4	3.7
Sinjar	*ETo* (PM) = 1.005 * *ETo*(PAN) - 0.499	0.983	5.4	3.7
Erbil	*ETo* (PM) = 0.971 * *ETo*(PAN) - 0.0634	0.996	3.9	3.4
Sul.	*ETo* (PM) = 0.993 * *ETo*(PAN) - 0.161	0.994	5.3	3.8
Kirkuk	*ETo* (PM) =0.851 * *ETo*(PAN) - 0.151	0.984	13.6	11.4
Baiji	*ETo* (PM) = 1.018 * *ETo*(PAN) - 0.416	0.982	12.7	9.6
Ana	*ETo* (PM) = 1.245 * *ETo*(PAN) - 0.668	0.985	12.9	9.5
Khalis	*ETo* (PM) = 1.107 * *ETo*(PAN) - 0.280	0.989	7.6	5.3
Bagdad	*ETo* (PM) = 1.083 * *ETo*(PAN) - 0.279	0.995	4.8	3.6
Hilla	*ETo* (PM) = 1.045 * *ETo*(PAN) - 0.178	0.991	5.4	4.6
Hadetha	*ETo* (PM) = 1.162 * *ETo*(PAN) - 0.150	0.983	8.6	6.6
Rutba	*ETo* (PM) = 0.923 * *ETo*(PAN) - 0.218	0.994	3.5	3.1
Kut	*ETo* (PM) = 1.068 * *ETo*(PAN) - 0.350	0.961	15.8	13.1
Nukhaib	*ETo* (PM) = 1.304 * *ETo*(PAN) - 0.807	0.983	9.4	8.1
Karbala	*ETo* (PM) = 1.080 * *ETo*(PAN) - 0.557	0.984	10.1	8.0
Najaf	*ETo* (PM) = 0.824 * *ETo*(PAN) - 0.641	0.986	7.2	5.6
Amara	*ETo* (PM) = 1.265 * *ETo*(PAN) - 0.526	0.988	9.7	7.4
Samawa	*ETo* (PM) = 1.187 * *ETo*(PAN) - 0.708	0.991	5.5	4.5
Nasiriya	*ETo* (PM) = 1.147 * *ETo*(PAN) - 0.571	0.991	6.1	4.6
Salman	*ETo* (PM) = 1.456 * *ETo*(PAN) – 1.574	0.977	24.1	20.4
Basrah	*ETo* (PM) = 1.215 * *ETo*(PAN) + 0.367	0.991	17.1	15.2

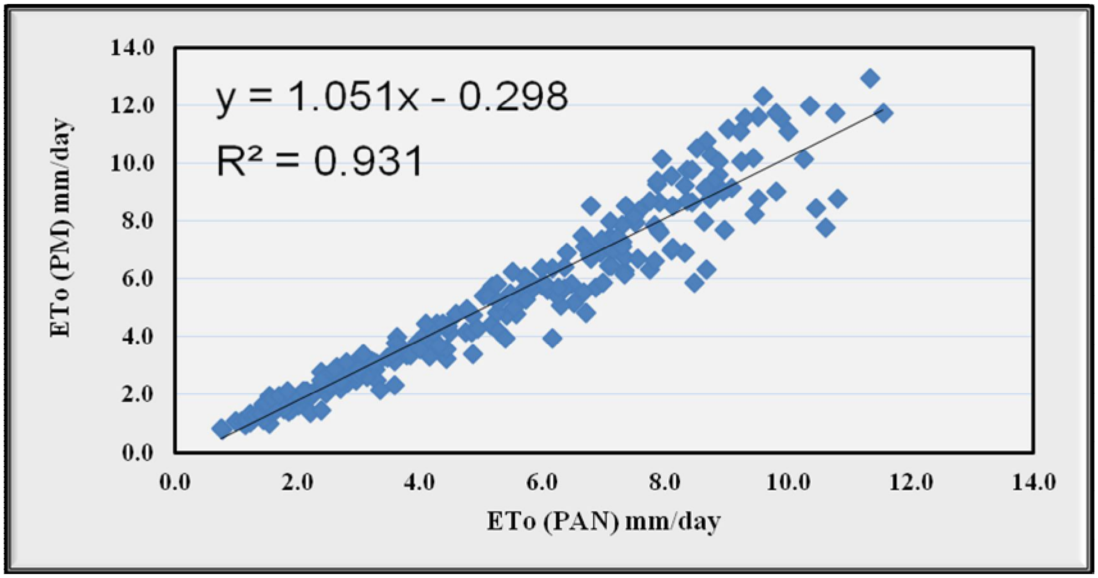

الشكل (4): علاقة الارتباط بين قيم ET_O المحسوبة بواسطة نموذجي (PM) و(PAN) بوحدات ملم/يوم لعموم العراق من خلال قيم جميع المحطات.

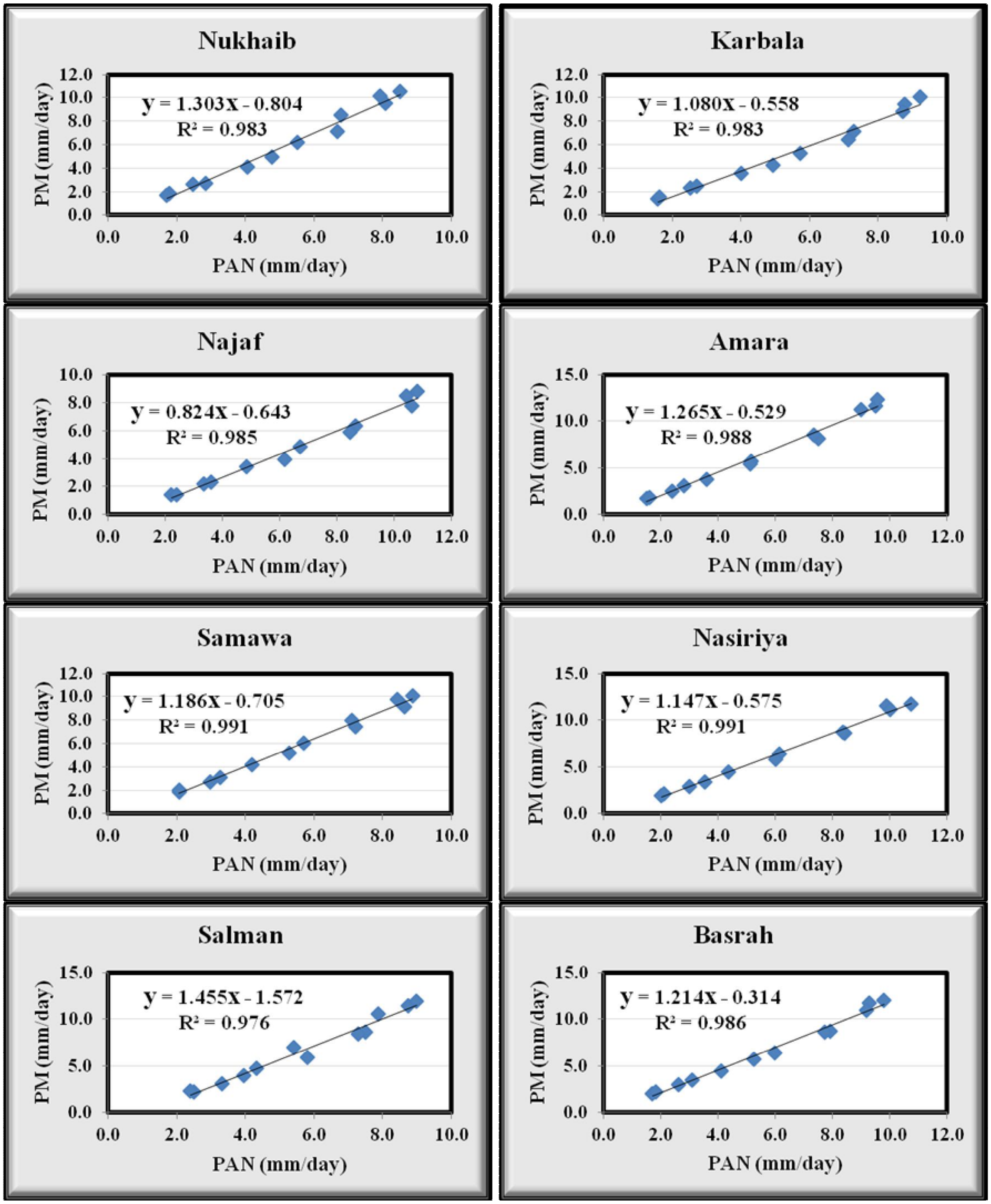

الشكل (3): علاقات الارتباط بين المعدلات الشهرية للقيم اليومية للتبخر – نتح المرجعي المحسوبة بطريقة (PM-1998) وطريقة حوض التبخر (PAN) في المحطات كافة

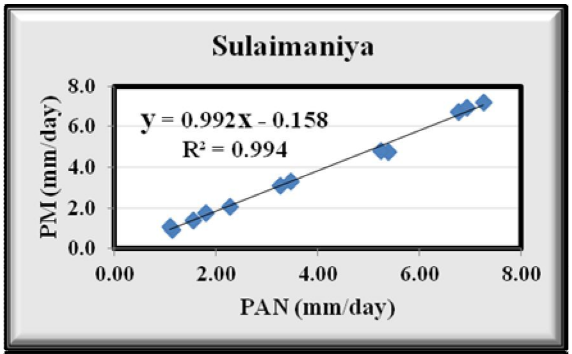
Sulaimaniya

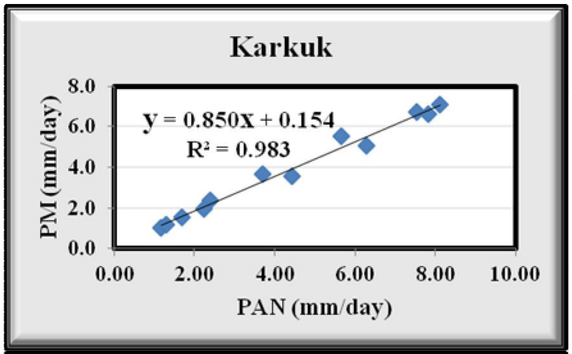
Karkuk

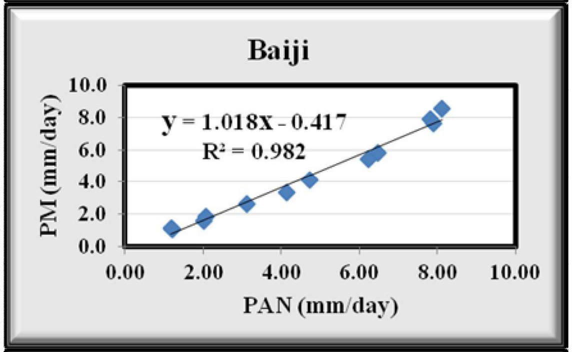
Baiji

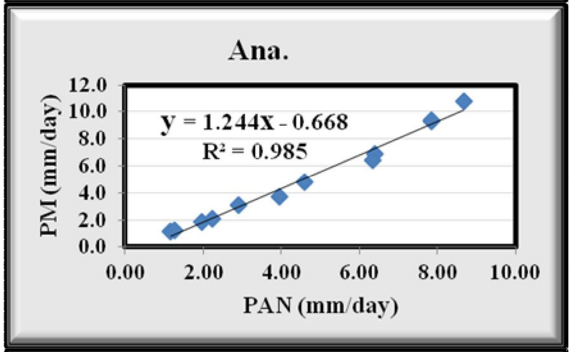
Ana.

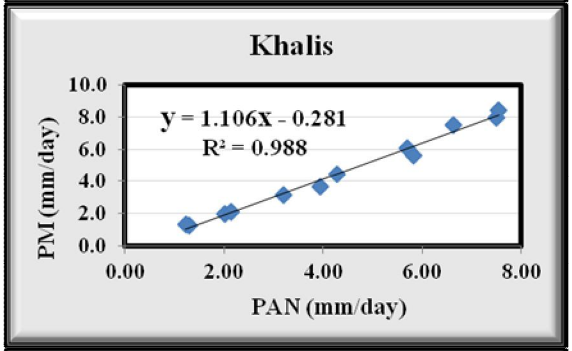
Khalis

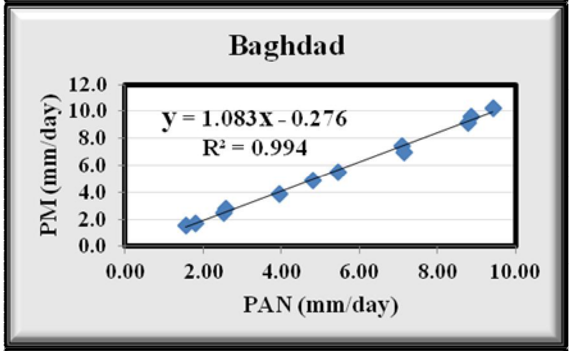
Baghdad

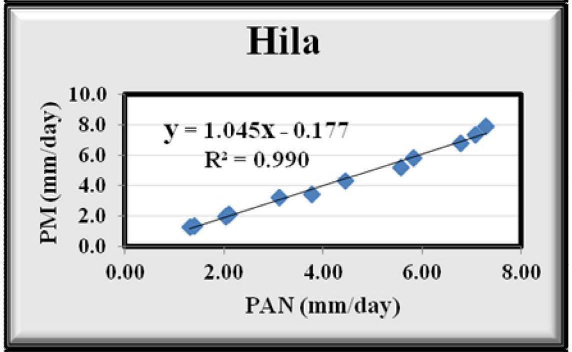
Hila

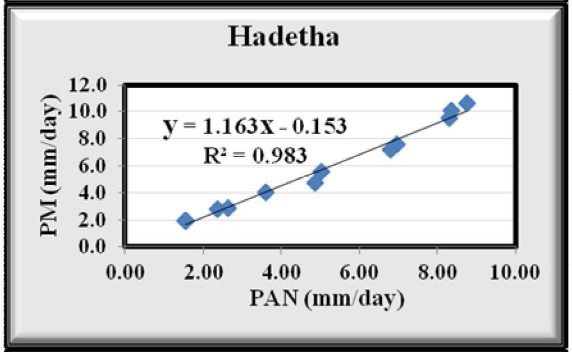
Hadetha

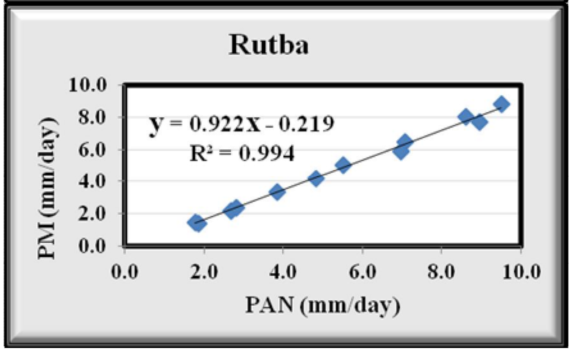
Rutba

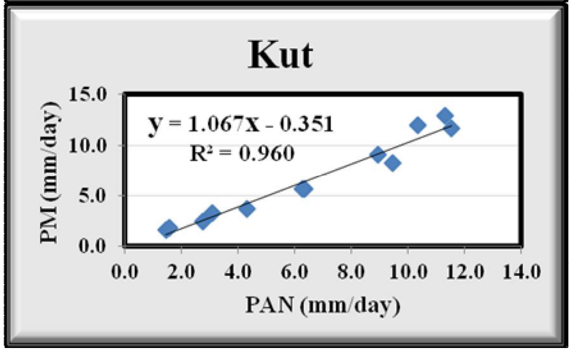
Kut

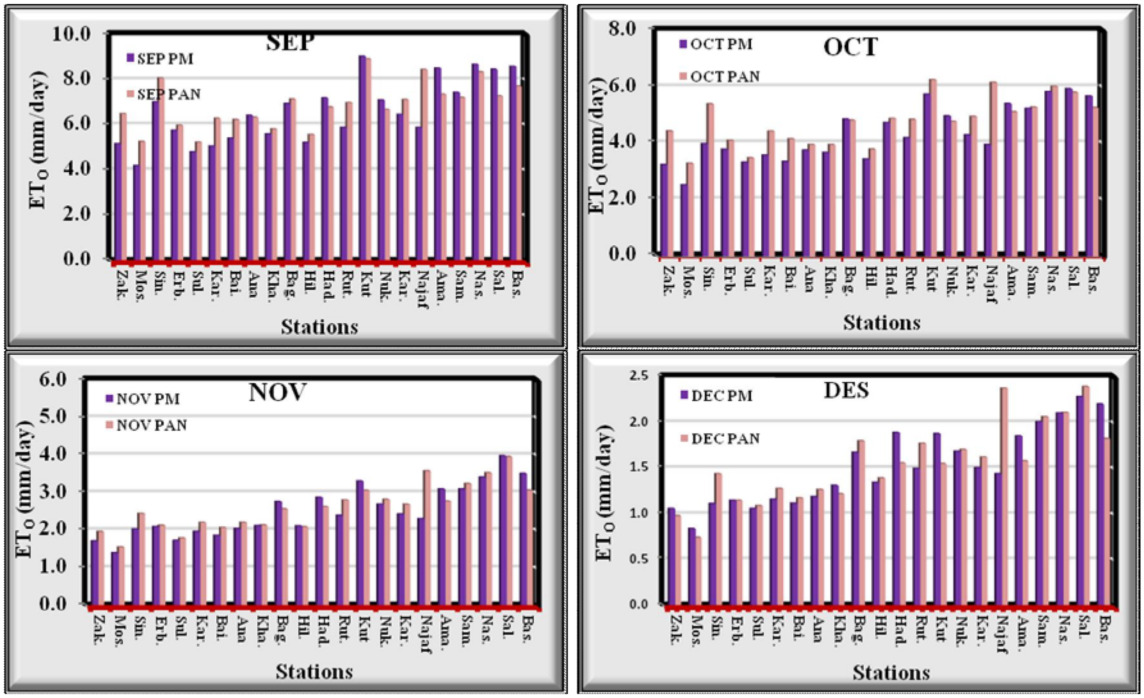

الشكل (2): المعدلات الشهرية للتبخر – نتح المرجعي ET_O بموجب نموذجي (PM,PAN) للمحطات كافة خلال أشهر السنة.

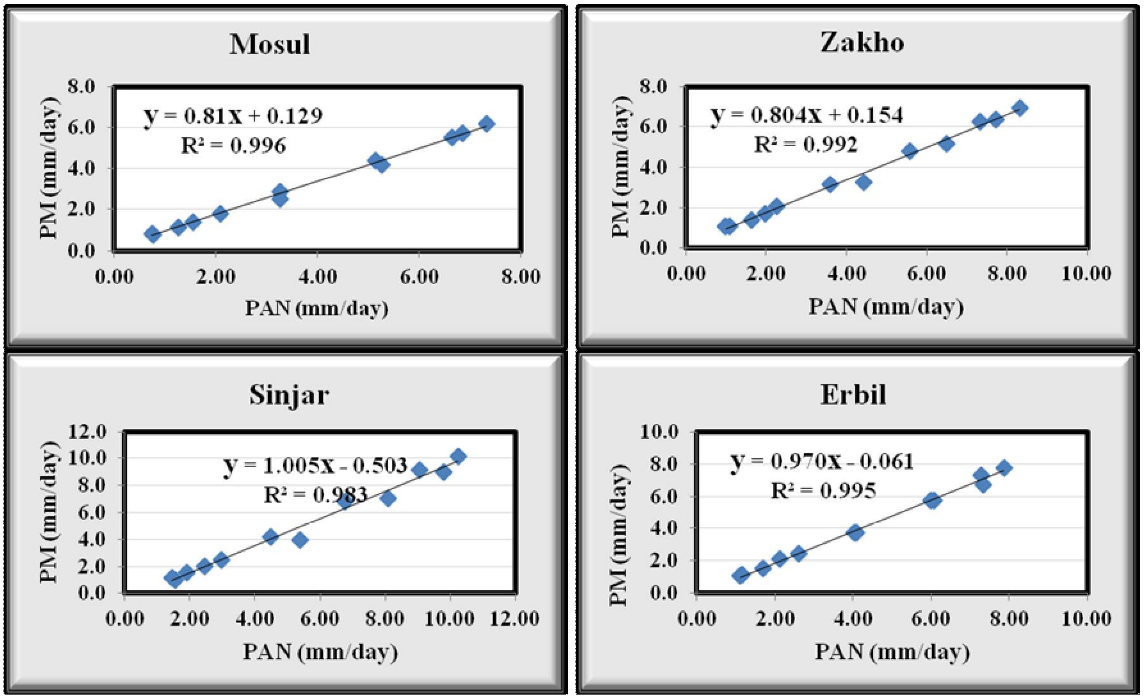

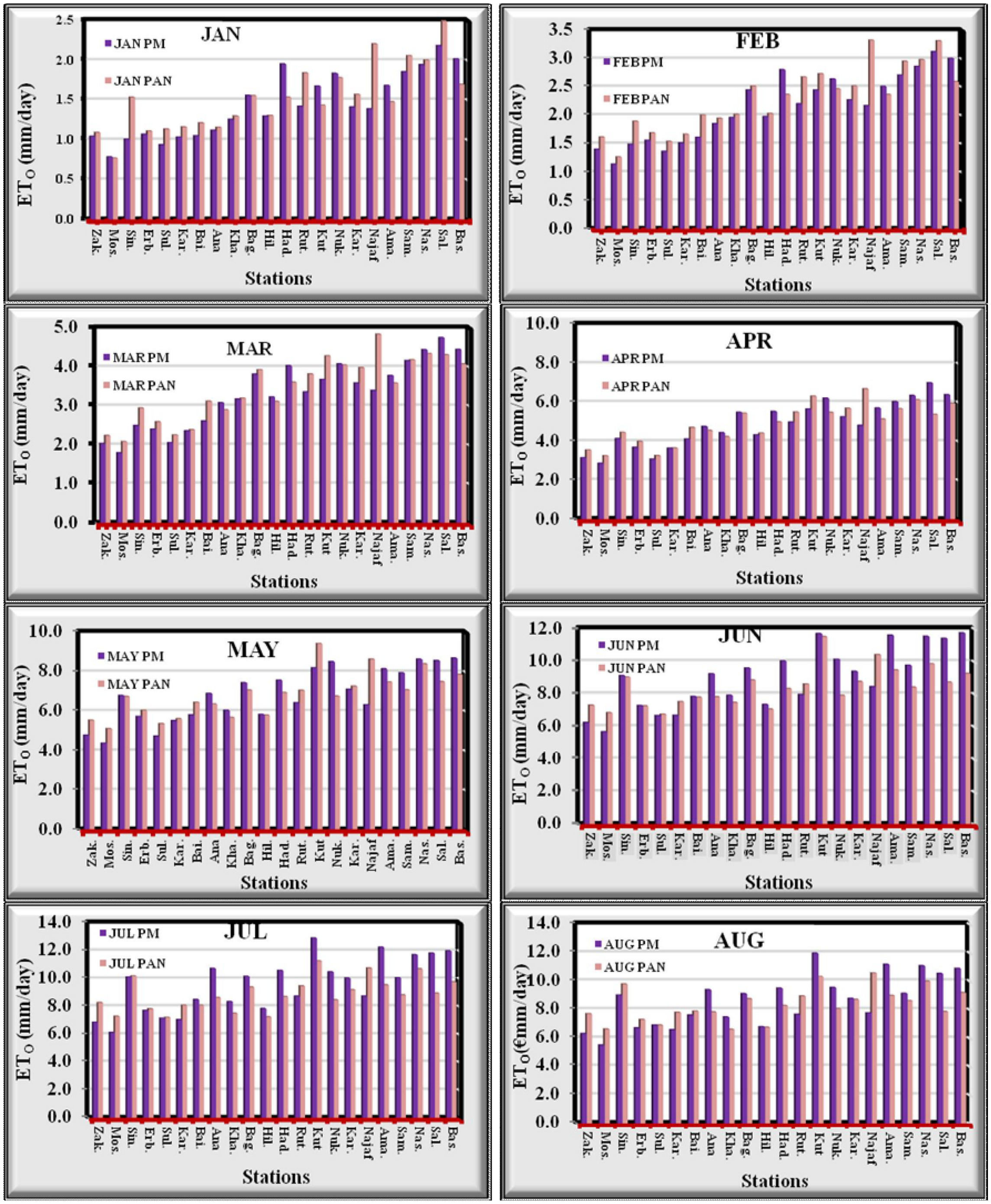
JAN
JAN PM
JAN PAN
FEB
FEB PM
FEB PAN
MAR
MAR PM
MAR PAN
APR
APR PM
APR PAN
MAY
MAY PM
MAY PAN
JUN
JUN PM
JUN PAN
JUL
JUL PM
JUL PAN
AUG
AUG PM
AUG PAN
ET$_O$ (mm/day)
Stations
Zak.
Mos.
Sin.
Erb.
Sul.
Kar.
Bai.
Ana
Kha.
Bag.
Hil.
Had.
Rut.
Kut
Nuk.
Kar.
Najaf
Ama.
Sam.
Nas.
Sal.
Bas.
0.0
0.5
1.0
1.5
2.0
2.5
3.0
3.5
4.0
5.0
6.0
8.0
10.0
12.0
14.0

النتائج والمناقشة

1. دراسة المعدلات الشهرية للقيم اليومية للتبخر – نتح المرجعي بموجب نموذجي (PAN, PM) للمحطات كافة

الشكل (2) يوضح مقارنة بين قيم ET_O المحسوبة بواسطة نموذجي (PAN , PM) للمحطات كافة خلال أشهر السنة بوحدات ملم/يوم. يلاحظ من المخططات أن هناك تقارباً كبيراً في الغالبية العظمى من المحطات بين قيم ET_O المحسوبة بواسطة النموذجين خلال أشهر السنة.

قيم ET_O المحسوبة بواسطة النموذجين خلال أشهر الشتاء كانت متدنية بسبب انخفاض كمية الإشعاع الشمسي قصير الموجة الواصل إلى سطح الأرض وتلبد السماء بالغيوم وانخفاض درجات الحرارة ومن ثم انخفاض التبخر من سطح الأرض والأسطح المائية. خلال أشهر الربيع، يلاحظ الارتفاع التدريجي في قيم ET_O نتيجة ارتفاع درجات الحرارة وقلة الغيمية وزيادة شدة الإشعاع الشمسي. خلال أشهر الصيف، يلاحظ الارتفاع الكبير في قيم ET_O في محطات الدراسة كافة، وذلك بسبب زيادة زاوية سمت الشمس التي تؤدي إلى زيادة كميات الإشعاع الشمسي الواصل إلى سطح الأرض، وهذا بدوره يعمل على رفع درجات الحرارة وزيادة التبخر من سطح الأرض والأسطح المائية، كما أن قلة الغيوم وارتفاع عدد ساعات السطوع الشمسي خلال أشهر الصيف أثرت أيضاً على زيادة قيم ET_O. أما خلال أشهر الخريف، فيلاحظ الانخفاض التدريجي في قيم ET_O في المحطات كافة.

2 . دراسة علاقات الارتباط بين قيم المعدلات الشهرية للقيم اليومية للتبخر – نتح المرجعي (ET_O) المحسوب بنموذج (PM-1998) ونموذج حوض التبخر (PAN) في المحطات كافة

الشكل (3) يوضح علاقات الارتباط بين المعدلات الشهرية للقيم اليومية للتبخر – نتح المرجعي (ET_O) المحسوب بنموذج (PM-1998) ونموذج حوض التبخر (PAN) في المحطات كافة.

العلاقات التي تم الحصول عليها أظهرت وجود ارتباط عالٍ جدًا بين قيم ET_O المحسوبة بواسطة النموذجين في المحطات كافة، حيث تراوح معامل التحديد (R^2) لهذه العلاقات بين (0.961-0.996). الجدول (2) يوضح المدلولات الإحصائية لهذه العلاقات، حيث يلاحظ أن قيم (RMSE , MAE) كانت منخفضة بشكل كبير في الغالبية العظمى من المحطات مما يوضح الارتباط العالي لهذين المتغيرين.

كما تم إيجاد علاقة ارتباط لعموم العراق بين قيم المعدلات الشهرية لِـ (ET_O) المحسوبة بواسطة النموذجين كما هو موضح في الشكل (4). العلاقة التي تم الحصول عليها هي:

$$\mathbf{ET_O (PM) = 1.051 * ET_O (PAN) - 0.298}$$

معامل التحديد (R^2) لهذه العلاقة بلغ (0.931).

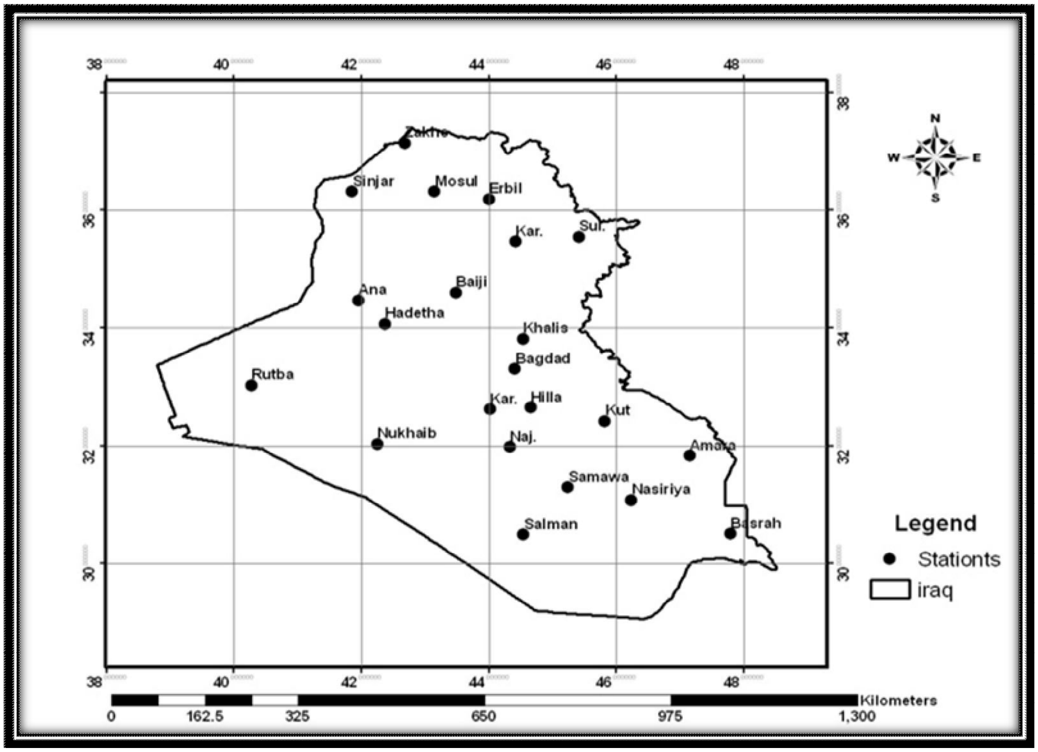

الشكل (1): مواقع المحطات كافة على خارطة العراق.

تم حساب التبخر – نتح المرجعي بطريقة PM-1998 حسب العلاقة التالية:

$$ET_0 = \frac{0.408\Delta\left(R_n - G\right) + \gamma \dfrac{900}{T+273} u_2 \left(e_s - e_a\right)}{\Delta + \gamma\left(1 + 0.34 u_2\right)}$$

حيث:

R_n: صافي الاشعاع الشمسي (ميجاجول/م^2.يوم)،

T: معدل درجة الحرارة $(T_{\max} + T_{\min})/2$ (°م)،

u_2: سرعة الرياح على ارتفاع مترين (م/ث)،

e_s: ضغط بخار التشبع (كيلو باسكال)،

e_a: ضغط البخار الفعلي (كيلو باسكال)،

$e_s - e_a$: عجز ضغط بخار التشبع (كيلو باسكال)،

$\Delta\ e_s - e_a$: ميل منحني ضغط بخار التشبع (كيلو باسكال / °م)،

γ: الثابت السايكرومتري (كيلو باسكال / °م).

تفاصيل مفردات هذه العلاقة موضحة في تقرير (FAO-56-1998).

كما تم حساب التبخر – نتح المرجعي بطريقة E_{pan} باستخدام العلاقة الاتية:

$$ET_o = K_p .\ E_{pan}$$

ET_o: التبخر – النتح (ملم/يوم)،

K_p: معامل الحوض،

E_{Pan} : تبخر الحوض (ملم/يوم).

وتم الحصول على قيم (K_p) وفقاً للعلاقة الاتية:

$$K_p = 0.108 - 0.0286\ u_2 + 0.0422\ \mathrm{Ln}\ (\mathrm{FET}) + 0.1434\ \mathrm{Ln}(RH_{mean}) - 0.000631\ [\mathrm{Ln}\ (\mathrm{FET})]^2\ \mathrm{Ln}\ (RH_{mean})$$

u_2. سرعة الرياح على ارتفاع مترين (م/ ث)،

RH_{mean}: معدل الرطوبة النسبية (%)،

FET: بعد الحوض عن الحشيش الأخضر (10 م).

وان قيم (K_p) تتغير ما بين (0.5 – 1.0)، وتعتمد القيمة الفعلية على نوع (Pan) وموقع القياس والفصل المناخي. تمت دراسة المعدلات الشهرية للقيم اليومية للتبخر–نتح المرجعي بوحدات ملم/يوم المحسوبة بموجب نموذجي (PAN, PM) للمحطات كافة.

كما تم إيجاد علاقات الارتباط بين قيم ET_O المحسوبة من النموذجين للمحطات كافة ولعموم العراق.

المقدمة

يعرف التبخر – نتح المرجعي بأنه أقصى كمية من البخار التي يمكن أن تنطلق من مساحة معينة من الأرض إلى الجو تحت تأثير العوامل الجوية الخاصة بتلك المنطقة. كما عرفت منظمة الأغذية والزراعة FAO-24 التبخر – نتح المرجعي بأنه معدل التبخر – نتح من سطح عشبي أخضر ممتد بارتفاع يبلغ (8-15) سم مزدهر النمو ويغطي الأرض كلياً ولا يعاني من شحُ المياه [1]. يعتبر التبخر – نتح المرجعي أحد الأركان الأساسية في الدراسات البيئية والهيدرولوجية لأنه يحدد درجة الاحتياج المائي للمحاصيل وما يلزمها من ري تكميلي، كما يحتل مكانة مهمة في التصانيف المناخية الحديثة لاستخدامه في علاقات قرائن الرطوبة [2، 3]. وقد اهتم العلماء بهذا المفهوم ووضعوا عدداً من العلاقات التجريبية لحسابه.

يعد نموذج فاو – بنمان – مونتيث (FAO-Penman-Montieth-1998) أهم نموذج قياسي لحساب التبخر – نتح المرجعي تحت الظروف المختلفة. هذا النموذج هو تمثيل بسيط للعوامل الفيزيائية والفسيولوجية التي تتحكم بعملية التبخر – نتح ويعتمد على بيانات مناخية حسب الحاجة والدقة المطلوبة [4، 5، 6]. كما يمكن حساب التبخر - نتح المرجعي بطريقة حوض التبخر ($FAO-E_{pan}$) بديلاً لطريقة بنمان – مونتيث في حالة عدم توفر بيانات مناخية كاملة يتطلبها نموذج بنمان – مونتيث، كما يتصف نموذج (E-pan) بأنه سهل الاستخدام ويعتمد بشكل رئيسي على عنصر التبخر وهو متوفر في الغالبية العظمى من محطات الأنواء الجوية [7]. هنالك العديد من الدراسات والبحوث التي أوجدت علاقات ارتباط بين قيم ET_O المحسوبة بواسطة النموذجين.

وجد Wayne وآخرون [8] (1999) علاقة ارتباط خطية طردية قوية بين ET_O والتبخر الحاصل من حوض التبخر من صنف A، وكان معامل التحديد لهذه العلاقة في حالة مروره بنقطة الأصل ($R^2=0.98$).

ووجد Lage وآخرون [9] (2005) علاقة ارتباط خطية طردية بين قيم ET_O المحسوبة بنموذج PM-1998 وتلك المحسوبة بنموذج E-pan، تراوح معامل التحديد لهذه العلاقة بين (0.83-0.79).

Richard وآخرون [10] 2005 قاموا بتخمين التبخر – نتح المرجعي (ET_O) من بيانات حوض التبخر E-pan في مناطق مختلفة من كاليفورنيا ذات المناخ الجاف وحصلوا على معامل تحديد عالٍ بلغ (0.92).

أما آلاء يعقوب [11] سنة (2012) فقد قامت بإيجاد علاقة ارتباط خطية قوية بين قيم ET_O المحسوبة بواسطة النموذجين في منطقة الموصل، وكان معامل التحديد لهذه العلاقة ($R^2=0.97$). يهدف هذا البحث إلى إيجاد علاقات ارتباط بين المعدلات الشهرية للقيم اليومية للتبخر – نتح المرجعي المحسوبة بواسطة النموذجين، وذلك في 22 محطة موزعة في عموم العراق للفترة (1980-2010).

المواد وطرائق البحث

بالاستعانة بالهيئة العامة للأنواء الجوية والرصد الزلزالي، أخذت بيانات العناصر الجوية التي يتطلبها كل من نموذجي PM-1998 وPAN-1998 وذلك للفترة (1980-2010) ل 22 محطة موزعة في عموم العراق.

الجدول (1) يوضح خطوط الطول والعرض والارتفاع لهذه المحطات. والشكل (1) يوضح مواقع المحطات كافة على خارطة العراق.

الجدول (1): خطوط الطول والعرض والارتفاع لكل المحطات.

Station	Latitude	Longitude	Altitude(m)	Station	Latitude	Longitude	Altitude(m)
Zakho	37º 08′	42º 41′	433	Hadetha	34º 04′	42 º 22′	634
Mosul	36º 19′	43º 09′	223	Rutba	33º 02′	40º 17′	630
Sinjar	36º 19′	40º 51′	465	Kut	32º 25′	45º 49′	23
Erbil	36º 11′	44º 00′	420	Nukhaib	32º 02′	42º 15′	305
Sulaimaniya	35º 33′	45º 25′	883	Karbala	32º 37′	44º 01′	29
Kirkuk	35º 28′	44º 25′	331	Najaf	31º 59	44º 20′	33
Baiji	34º 36′	43º 29′	115	Amara	31º 50′	47º 09′	9
Ana	34º 28′	41º 57′	139	Samawa	31º 18′	45º 17′	6
Khalis	33º 49′	44º 32′	42	Nasiriya	31º 05′	46º 14′	5
Bagdad	33º 18′	44º 24′	32	Salman	30º 30′	44º 32′	220
Hilla	32º 39′	44 39	27	Basrah	30º 31′	47º 47′	2

المجلد 7، العدد 1، 2014. ص ص. 52-43

المجلة الأردنية للفيزياء

ARTICLE

مقارنة بين نموذجي بنمان- مونتيث وحوض التبخر في تخمين التبخر - نتح المرجعي في مناطق مختلفة من العراق

وليد اسمير جاسم وهاني محمد حمدون

قسم الفيزياء، كلية التربية، جامعة الموصل، الموصل، العراق.

Received on: 15/12/2013; Accepted on: 25/3/2014

الملخص: يهدف البحث إلى إيجاد المعدلات الشهرية للتبخر – نتح المرجعي (ET_O) في (22) محطة موزعة في عموم العراق، وذلك من خلال نموذج (PM-1998) المستخدم بشكل واسع عالمياً ونموذج حوض التبخر (PAN- Class-A) للفترة (2010-1980). أظهرت النتائج وجود تقارب كبير بين قيم المعدلات الشهرية للتبخر – نتح المرجعي المحسوبة بواسطة النموذجين في كل المحطات. كما أظهرت النتائج وجود ارتباط عالٍ جداً بين قيم (ET_O) المحسوبة بواسطة النموذجين في المحطات كافة، حيث تراوح معامل التحديد (R^2) بين (0.996-0.961) ، كما كانت (RMSE , MAE) منخفضة بشكل كبير في الغالبية العظمى من المحطات مما يوضح الدقة العالية لهذه العلاقات. كما تم إيجاد علاقة ارتباط لعموم العراق بين قيم المعدلات الشهرية لِ (ET_O) المحسوبة بواسطة النموذجين التي أعطت معامل تحديد (R^2) عاليًا بلغ (0.931).

الكلمات المفتاحية: التبخر – نتح المرجعي؛ (PM-1998)؛ E- pan؛ FAO-56؛ ET_o.

Comparison between Penman-Montieth Model and Pan Evaporation Model in the Estimation of Reference Evapotranspiration in Different Regions in IRAQ

Waleed Jasem and Hani Hamdoon

Physics Department, College of Education, Mosul University, Mosul, Iraq.

Abstract: The objective of this research is to find the mean monthly values of reference evapotranspiration (ET_O) in 22 stations distributed all over Iraq using (PM-1998) model which is widely used worldwide and E_{pan} (class A) model during the period (1980-2010). The results showed high convergence between the mean monthly values of reference evapotranspiration calculated by the two models in all stations. The results showed also very high correlation between (ET_O) calculated by the two models in all stations, where (R^2) ranged between (0.961-0.996), in addition to that (MAE, RMSE) values were found very low in most of the stations. This demonstrates the accuracy of these correlations. Also, correlation was found all over Iraq between the mean monthly values of (ET_O) calculated by the two models, with a high value of (R^2) which was equal to (0.931).

Keywords: FAO-56; PM-1998; E-pan; ET_o.

Corresponding Author: Waleed Jasem **Email**: dr.waleedis@yahoo.com

Authors Index

Subject Index

طرائق البحث (التجريبية / النظرية): يجب أن تكون هذه الطرائق موضحة بتفصيل كاف لإتاحة إعادة إجرائها بكفاءة، ولكن باختصار مناسب، حتى لا تكون تكرارا للطرائق المنشورة سابقا.

النتائج: يستحسن عرض النتائج على صورة جداول وأشكال حيثما أمكن، مع شرح قليل في النص ومن دون مناقشة تفصيلية.

المناقشة: يجب أن تكون موجزة وتركز على تفسير النتائج.

الاستنتاج: يجب أن يكون وصفا موجزا لأهم ما توصلت إليه الدراسة ولا يزيد عن صفحة مطبوعة واحدة.

الشكر والعرفان: الشكر والإشارة إلى مصدر المنح والدعم المالي يكتبان في فقرة واحدة تسبق المراجع مباشرة.

المراجع: يجب طباعة المراجع بأسطر مزدوجة ومرقمة حسب تسلسلها في النص. وتكتب المراجع في النص بين قوسين مربعين. ويتم اعتماد اختصارات الدوريات حسب نظام Wordlist of Scientific Reviewers.

الجداول: تعطى الجداول أرقاما متسلسلة يشار إليها في النص. ويجب طباعة كل جدول على صفحة منفصلة مع عنوان فوق الجدول. أما الحواشي التفسيرية، التي يشار إليها بحرف فوقي، فتكتب أسفل الجدول.

الرسوم التوضيحية: يتم ترقيم الأشكال والرسومات والرسومات البيانية (المخططات) والصور، بصورة متسلسلة كما وردت في النص.

تقبل الرسوم التوضيحية المستخرجة من الحاسوب والصور الرقمية ذات النوعية الجيدة بالأبيض والأسود، على ان تكون أصيلة وليست نسخة عنها، وكل منها على ورقة منفصلة ومعرفة برقمها بالمقابل. ويجب تزويد المجلة بالرسومات بحجمها الأصلي بحيث لا تحتاج إلى معالجة لاحقة، وألا تقل الحروف عن الحجم 8 من نوع Times New Roman، وألا تقل سماكة الخطوط عن 0.5 وبكثافة متجانسة. ويجب إزالة جميع الألوان من الرسومات ما عدا تلك التي ستنشر ملونة. وفي حالة إرسال الرسومات بصورة رقمية، يجب أن تتوافق مع متطلبات الحد الأدنى من التمايز (1200 dpi Resolution) لرسومات الأبيض والأسود الخطية، و 600 dpi للرسومات باللون الرمادي، و300 dpi للرسومات الملونة. ويجب تخزين جميع ملفات الرسومات على شكل (jpg)، وأن ترسل الرسوم التوضيحية بالحجم الفعلي الذي سيظهر في المجلة. وسواء أرسل المخطوط بالبريد أو عن طريق الشبكة (Online)، يجب أرسال نسخة ورقية أصلية ذات نوعية جيدة للرسومات التوضيحية.

مواد إضافية: تشجع المجلة الباحثين على إرفاق جميع المواد الإضافية التي يمكن أن تسهل عملية التحكيم. وتشمل المواد الإضافية أي اشتقاقات رياضية مفصلة لا تظهر في المخطوط.

المخطوط المنقح (المعدَل) والأقراص المدمجة: بعد قبول البحث للنشر وإجراء جميع التعديلات المطلوبة، فعلى الباحثين تقديم نسخة أصلية ونسخة أخرى مطابقة للأصلية مطبوعة بأسطر مزدوجة، وكذلك تقديم نسخة إلكترونية تحتوي على المخطوط كاملا مكتوبا على Microsoft Word for Windows 2000 أو ما هو استجد منه. ويجب إرفاق الأشكال الأصلية مع المخطوط النهائي المعدل حتى لو تم تقديم الأشكال إلكترونيا. وتخزن جميع ملفات الرسومات على شكل (jpg)، وتقدم جميع الرسومات التوضيحية بالحجم الحقيقي الذي ستظهر به في المجلة. ويجب إرفاق قائمة ببرامج الحاسوب التي استعملت في كتابة النص، وأسماء الملفات على قرص مدمج، حيث يعلَم القرص بالاسم الأخير للباحث، وبالرقم المرجعي للمخطوط للمراسلة، وعنوان المقالة، والتاريخ. ويحفظ في مغلف واقٍ.

الفهرسة: تقوم المجلة الأردنية للفيزياء بالإجراءات اللازمة لفهرستها وتلخيصها في جميع الخدمات الدولية المعنية.

حقوق الطبع

يُشكِّل تقديم مخطوط البحث للمجلة اعترافاً صريحاً من الباحثين بأنَ مخطوط البحث لم يُنْشَر ولم يُقَدَّم للنشر لدى أي جهَة أخرى كانت وبأي صيغة ورقية أو إلكترونية أو غيرها. ويُشترط على الباحثين ملء أنموذج يَنُصُّ على نقْل حقوق الطبع لتُصبح ملكاً لجامعة اليرموك قبل الموافقة على نشر المخطوط. ويقوم رئيس التحرير بتزويد الباحثين بإنموذج نقل حقوق الطبع مع النسخة المُرْسَلَة للتنقيح. كما ويُمنع إعادة إنتاج أيِّ جزء من الأعمال المنشورة في المجلّة من دون إذن خَطِّيٍّ مُسْبَق من رئيس التحرير.

إخلاء المسؤولية

إن ما ورد في هذه المجلة يعبر عن آراء المؤلفين، ولا يعكس بالضرورة آراء هيئة التحرير أو الجامعة أو سياسة اللجنة العليا للبحث العلمي أو وزارة التعليم العالي والبحث العلمي. ولا يتحمل ناشر المجلة أي تبعات مادية أو معنوية أو مسؤوليات عن استعمال المعلومات المنشورة في المجلة أو سوء استعمالها.

معلومات عامة

المجلة الأردنية للفيزياء هي مجلة بحوث علميّة عالمية متخصصة مُحكمة تصدر بدعم من صندوق دعم البحث العلمي، وزارة التعليم العالي والبحث العلمي، عمان، الأردن. وتقوم بنشر المجلة عمادة البحث العلمي والدراسات العليا في جامعة اليرموك، إربد، الأردن. وتنشر البحوث العلمية الأصيلة، إضافة إلى المراسلات القصيرة Short Communications، والملاحظات الفنية Technical Notes، والمقالات الخاصّة Feature Articles، ومقالات المراجعة Review Articles، في مجالات الفيزياء النظرية والتجريبية، باللغتين العربية والإنجليزية.

تقديم مخطوط البحث

تُرسَل نسخة أصلية وثلاث نسخٍ من المخطوط، مُرْفَقَةً برسالة تغطية من جانب الباحث المسؤول عن المراسلات، إلى رئيس التحرير:

أ.د. نهاد عبدالرؤف يوسف،
رئيس التحرير، المجلة الأردنية للفيزياء،
عمادة البحث العلمي والدراسات العليا،
جامعة اليرموك، إربد، الأردن.
هاتف : 111 11 72 2 962 00 / فرعي: 2075
فاكس : 121 11 72 2 962 00
بريد إلكتروني : jjp@yu.edu.jo

تقديم المخطوطات إلكترونيًا: اتبع التعليمات في موقع المجلة على الشبكة العنكبوتية.

ويجري تحكيمُ البحوثِ الأصيلة والمراسلات القصيرة والملاحظات الفنية من جانب مُحكِّمين اثنين في الأقل من ذوي الاختصاص والخبرة. وتُشَجِّع المجلة الباحثين على اقتراح أسماء المحكمين. أما نشر المقالات الخاصّة في المجالات الفيزيائية النَشِطَة، فيتم بدعوة من هيئة التحرير، ويُشار إليها كذلك عند النشر. ويُطْلَب من كاتب المقال الخاص تقديم تقرير واضح يتّسم بالدقة والإيجاز عن مجال البحث تمهيداً للمقال. وتنشر المجلةُ أيضاً مقالات المراجعة في الحقول الفيزيائية النشطة سريعة التغيُّر، وتُشَجَّع كاتبي مقالات المراجعة أو مُستَكتبيها على إرسال مقترحٍ من صفحتين إلى رئيس التحرير. ويُرْفَق مع البحث المكتوب باللغة العربية ملخص (Abstract) وكلمات دالة (Keywords) باللغة الإنجليزية.

ترتيب مخطوط البحث

يجب أن تتم طباعة مخطوط البحث ببنط 12 نوعه Times New Roman، وبسطر مزدوج، على وجه واحد من ورق A4 (21.6 × 27.9 سم) مع حواشي 3.71 سم ، باستخدام معالج كلمات ميكروسوفت وورد 2000 أو ما استَجَد منه. ويجري تنظيم أجزاء المخطوط وفق الترتيب التالي: صفحة العنوان، الملخص، رموز التصنيف (PACS)، المقدّمة، طرق البحث، النتائج، المناقشة، الخلاصة، الشكر والعرفان، المراجع، الجداول، قائمة بدليل الأشكال والصور والإيضاحات، ثَمَّ الأشكال والصور والإيضاحات. وتُكْتَب العناوين الرئيسة بخطٍ **غامق**، بينما تُكْتَب العناوين الفرعية بخطٍ *مائل*.

صفحة العنوان: وتشمل عنوان المقالة، أسماء الباحثين الكاملة وعناوين العمل كاملة. ويكتب الباحث المسؤول عن المراسلات اسمه مشارا إليه بنجمة، والبريد الإلكتروني الخاص به. ويجب أن يكون عنوان المقالة موجزا وواضحا ومعبرا عن فحوى (محتوى) المخطوط، وذلك لأهمية هذا العنوان لأغراض استرجاع المعلومات.

الملخص: المطلوب كتابة فقرة واحدة لا تزيد على مائتي كلمة، موضحة هدف البحث، والمنهج المتبع فيه والنتائج وأهم ما توصل إليه الباحثون.

الكلمات الدالة: يجب أن يلي الملخص قائمة من 4-6 كلمات دالة تعبر عن المحتوى الدقيق للمخطوط لأغراض الفهرسة.

PACS: يجب إرفاق الرموز التصنيفية، وهي متوافرة في الموقع http://www.aip.org/pacs/pacs06/pacs06-toc.html.

المقدمة: يجب أن توضّح الهدف من الدراسة وعلاقتها بالأعمال السابقة في المجال، لا أن تكون مراجعة مكثفة لما نشر (لا تزيد المقدمة عن صفحة ونصف الصفحة مطبوعة).

Subscription Form

Jordan Journal of

PHYSICS

An International Peer-Reviewed Research Journal issued by the Support of the Scientific Research Support Fund

Published by the Deanship of Research & Graduate Studies, Yarmouk University, Irbid, Jordan

Name: .... :الأسم
Specialty:...:التخصص
Address: ....:العنوان
P.O. Box:.. : صندوق البريد
City & Postal Code: ....:المدينة/الرمز البريدي
Country: ....:الدولة
Phone: ....:رقم الهاتف
Fax No:.. :رقم الفاكس
E-mail:.. :البريد الإلكتروني
No. of Subscription: .... :عدد الإشتراكات
Method of Payment:.. :طريقة الدفع
Amount Enclosed:... :المبلغ المرفق
Signature: ....:التوقيع

Cheques should be paid to Deanship of Research and Graduate Studies - Yarmouk University.

I would like to subscribe to the Journal
For

☐ One Year
☐ Two Years
☐ Three Years

One Year Subscription Rates

	Inside Jordan	Outside Jordan
Individuals	JD 8	€ 40
Students	JD 4	€ 20
Institutions	JD 12	€ 60

Correspondence

Subscriptions and Sales:

Prof. Ibrahim O. Abu-AlJarayesh
Deanship of Research and Graduate Studies
Yarmouk University
Irbid – Jordan
Telephone: 00 962 2 711111 Ext. 2075
Fax No.: 00 962 2 7211121

المملكة الأردنية الهاشمية جامعة اليرموك

المجلة الأردنية
للفيزياء

مجلة بحوث علمية عالمية متخصصة محكّمة
تصدر بدعم من صندوق دعم البحث العلمي

المجلد (7)، العدد (1)، 2014م / 1435هـ

المجلة الأردنية

للفيزياء

مجلة بحوث علمية عالمية محكّمة

المجلد (7)، العدد (1)، 2014م / 1435هـ

المجلة الأردنية للفيزياء: مجلة علمية عالمية متخصصة محكّمة تصدر بدعم من صندوق دعم البحث العلمي، وزارة التعليم العالي والبحث العلمي، الأردن، وتصدر عن عمادة البحث العلمي والدراسات العليا، جامعة اليرموك، إربد، الأردن.

ترسل البحوث إلى العنوان التالي:

الأستاذ الدكتور نهاد عبد الرؤوف يوسف
رئيس تحرير المجلة الأردنية للفيزياء
عمادة البحث العلمي والدراسات العليا، جامعة اليرموك
إربد ، الأردن
هاتف 7211111 2 962 00 **فرعي** 2075
E-mail: *jjp@yu.edu.jo*
Website: *http://Journals.yu.edu.jo/jjp*